Chemical Science

RSC Publishing

EDGE ARTICLE

Lanthanide hexafluoroacetylacetonates *vs*. nitrates for the controlled loading of luminescent polynuclear single-stranded oligomers†

Cite this: *Chem. Sci.*, 2013, **4**, 1125

Amir Zaïm,[a] Natalia Dalla Favera,[a] Laure Guénée,[b] Homayoun Nozary,[a] Thi Nhu Y. Hoang,[a] Svetlana V. Eliseeva,[cd] Stéphane Petoud[c] and Claude Piguet*[a]

Received 14th November 2012
Accepted 10th December 2012

DOI: 10.1039/c2sc21982d

www.rsc.org/chemicalscience

This work demonstrates how minor structural and electronic changes between $Ln(NO_3)_3$ and $Ln(hfac)_3$ lanthanide carriers (Ln = trivalent lanthanide, hfac = hexafluoroacetylacetonate) lead to opposite thermodynamic protocols for the metal loading of luminescent polynuclear single-stranded oligomers. Whereas metal clustering is relevant for $Ln(hfac)_3$, the successive fixation of $Ln(NO_3)_3$ provides stable microspecies with an alternated occupancy of the binding sites. Partial anion dissociation and anion/ligand bi-exchange processes occur in polar aprotic solvents, which contribute to delay the unambiguous choice of a well-behaved neutral lanthanide carrier for the selective complexation of different trivalent lanthanides along a single ligand strand. Clues for further improvement along this stepwise strategy are discussed.

Introduction

Lanthanide-centred Yb/Er or Tm/Er upconverting pairs doped into ionic solids,[1] nanoparticles,[2] metal–organic frameworks,[3] nanotubes[4] and nanocrystals[5] are currently the subject of intense investigations for potential applications as spectral concentrators for solar cells[6] and as imaging agents for biological systems.[7] Independently of the level of theoretical modelling,[8] the indirect sensitization of the activator *via* energy-transfer upconversion (ETU) mechanisms appears to be the most efficient way for inducing metal-centred upconversion. Its rational and tuneable implementation requires the precise spatial location of different trivalent lanthanide cations, Ln^{III}, displaying controlled intermetallic communications, a challenge which is difficult to address by using statistically doped materials.[9] As a first step toward this goal, the recent programming of linear Cr–Ln–Cr sequences[10] indeed demonstrated unprecedented Cr-sensitized Er-centred upconversion,[11] and this strategy might offer an attractive alternative to doped solids considering that Wolf type II metallopolymers can be selectively fed with different lanthanides (Fig. 1a).

The thermodynamic Ising model limited to near–neighbour interactions (Fig. 1a) predicts that organized sequences of

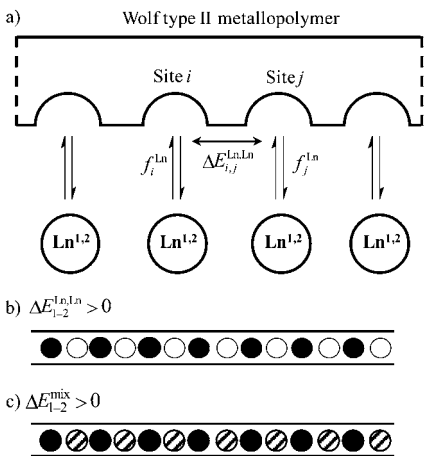

Fig. 1 (a) Thermodynamic model adapted for the successive intermolecular connections of different lanthanide cations (Ln^1 or Ln^2) to multi-site Wolf type II metallopolymer (f_i^{Ln} is the microscopic affinity of site *i* for Ln and $\Delta E_{i,j}^{Ln,Ln}$ is the intermetallic interaction between cations occupying sites *i* and *j*), and pictorial representation of associated microstates for (b) homometallic loading process for half-saturation and (c) heterobimetallic competition for saturation occurring upon negative cooperativity.

[a]*Department of Inorganic and Analytical Chemistry, University of Geneva, 30 quai E. Ansermet, CH-1211 Geneva 4, Switzerland. E-mail: Claude.Piguet@unige.ch*

[b]*Laboratory of X-ray Crystallography, University of Geneva, 24 quai E. Ansermet, CH-1211 Geneva 4, Switzerland*

[c]*Centre de Biophysique Moléculaire, CNRS UPR 4301, Rue Charles-Sadron, 45071 Orléans Cedex 2, France*

[d]*Le Studium® Institute for Advanced Studies, Orléans & Tours, France*

† Electronic supplementary information (ESI) available: Geometrical analyses (Appendices 1 and 2), correction of electronic absorption spectra (Appendix 3) and calculation of binding isotherms (Appendix 4). Tables of ^1H and ^{19}F NMR shifts, elemental analyses, crystal data, geometric parameters and bond valences, photophysical data, thermodynamic stability constants and associated microscopic describers. Figures showing molecular structures with numbering schemes, molecular superimpositions, crystal packing, symmetry numbers, ^1H, ^{13}C and ^{19}F NMR spectra, electronic absorption and emission spectra. CCDC 909092–909096. For ESI and crystallographic data in CIF or other electronic format see DOI: 10.1039/c2sc21982d

occupied and unoccupied sites can be obtained upon half-saturation with a single type of metal ion undergoing repulsive vicinal intermetallic interactions ($\Delta E_{1,2}^{Ln,Ln} > 0$ in Fig. 1b).[12] This prediction can be extended to the design of a strict alternation of two different lanthanides Ln^1 and Ln^2 if the mixing rule $\Delta E_{1,2}^{mix} = \Delta E_{1,2}^{Ln1,Ln1} + \Delta E_{1,2}^{Ln2,Ln2} - 2\Delta E_{1,2}^{Ln1,Ln2} > 0$ is obeyed in saturated metallopolymers (Fig. 1c),[13] a situation ideally suited for some future optimization of metal-centred upconversion.[11] The current lack of accessible linear single-stranded oligomeric or polymeric receptors containing regularly spaced binding sites for encapsulating Ln(III) prevented the experimental validation of this strategy. Nevertheless, we note that the related competitive complexation of two different lanthanides into four adjacent binding sites in self-assembled linear triple-stranded helicates indeed displayed weak, but perceptible anti-cooperative behaviour for the La–Lu pair ($\Delta E_{1,2}^{mix}$ = +2 kJ mol^{-1}).[14] Having gained some experience in the coordination of trivalent lanthanides with tridentate polyaromatic ligands,[15] we foresee to exploit the segmental linear polymeric single-stranded receptor **1**, in which well-known rigid tridentate N_3 and N_2O binding sites are separated by Z-spacers for its selective loading with neutral LnX_3 metallic carriers, X being a didentate monoanion (Scheme 1a). Whereas carboxylates ($X = RCOO^-$)[16] and nitrates ($X = NO_3^-$)[17] anions failed to support a simple thermodynamic rationalization because of the formation of polynuclear dimers with **L1**, hexafluoracetylacetonates ($X = F_3C–CO–CH–CO–CF_3^- = hfac^-$) showed more encouraging results with the formation of saturated nine-coordinated mononuclear complexes with **L1** (Scheme 1b).[18]

We therefore explore in this contribution the structural and thermodynamic consequences of the metal loading of segmental oligomeric ligands of increasing size (**L1–L4**) with $Ln(hfac)_3$ and $Ln(NO_3)_3$. The short methylene spacer ($Z = CH_2$) has been selected because it is sufficiently rigid to prevent intramolecular chelation events, which are not compatible with a straightforward analysis within the frame of the Ising model.[19]

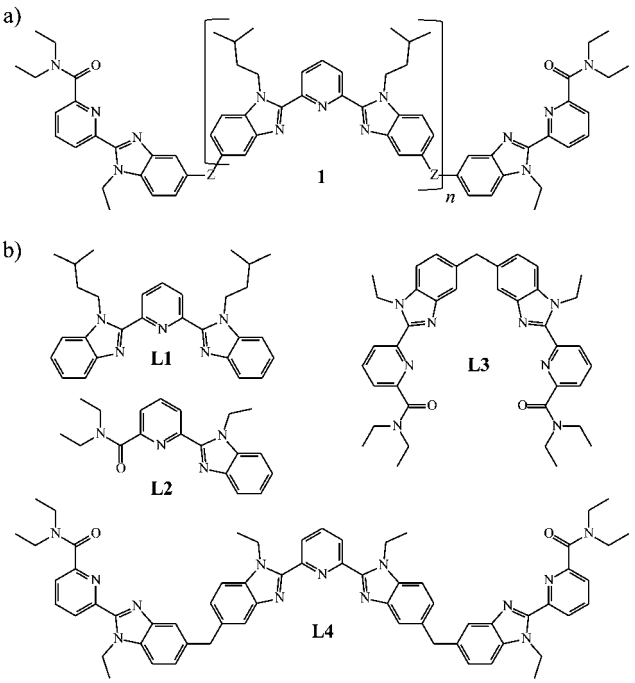

Scheme 1 Chemical structures for (a) the target single-stranded polymer with Z-spacers and (b) the segmental oligomeric ligands **L1–L4** used in this work.

Results and discussion

Synthesis, structural characterization and photophysical properties of the complexes $[Ln_m(Lk)(hfac)_{3m}]$ (Ln = La, Eu, Gd, Lu; L*k* = L2–L4; *m* = 1–3)

Reactions of stoichiometric amounts of **L2** (1 eq.),[20] or **L3** (0.5 eq.),[21] or **L4** (0.33 eq.)[22] with $[Ln(hfac)_3(diglyme)]$ (1.0 eq., Ln = Eu, Gd, Lu)[23] in dichloromethane/acetonitrile yielded 70–80% of microcrystalline powders whose elemental analyses were compatible with the formation of the single-stranded complexes $[Ln(\mathbf{L2})(hfac)_3]$, $[Ln_2(\mathbf{L3})(hfac)_6]\cdot xH_2O$ and $[Ln_3(\mathbf{L4})(hfac)_9]\cdot xH_2O$ (Table S1, ESI†). Slow evaporation of concentrated acetonitrile solutions gave X-ray quality prisms for $[Eu(\mathbf{L2})(hfac)_3]$ (**2**), $[Eu_2(\mathbf{L3})(hfac)_6]$ (**3**), $[Eu_3(\mathbf{L4})(hfac)_9]\cdot 5.5CH_3CN$ (**4**), $[Lu(\mathbf{L2})(hfac)_3]$ (**5**) and $[Lu_2(\mathbf{L3})(hfac)_6]$ (**6**)[24] (Table S2 and Fig. S1–S3, ESI†). Careful inspection of the crystal packing revealed no remarkable intermolecular interaction for **2**, whereas all other complexes exhibited one type of weak offset π-stacking interaction between pairs of parallel aromatic benzimidazole rings belonging to neighbouring complexes related by inversion centres (Fig. S4–S6, ESI†).[25] The molecular structures for the pertinent pairs of analogous Eu and Lu complexes (**2–5** in Fig. S7, **3–6** in Fig. S8†) are almost superimposable, and the discussion is therefore limited to the series of europium complexes **2–4** (Fig. 2). Each europium cation is nine-coordinated by the three donor atoms of a meridionally bound tridentate ligand (N_3 or N_2O donor sets) and by the six oxygen atoms of three didentate hexafluoroacetylacetonate anions, one lying close to the coordination plane defined by the Eu atom and the three donor atoms of the tridentate binding unit (= equatorial hfac), whilst the two remaining $hfac^-$ ions are arranged on both sides of this plane (= axial hfac, Fig. 2 and 3).

The EuN_2O_7 coordination spheres found in $[Eu(\mathbf{L2})(hfac)_3]$, $[Eu_2(\mathbf{L3})(hfac)_6]$ and $[Eu_3(\mathbf{L4})(hfac)_9]$ are almost superimposable (Fig. S9 and S10†), as are the EuN_3O_6 coordination spheres in $[Eu_3(\mathbf{L4})(hfac)_9]$ and $[Eu(\mathbf{L1})(hfac)_3]$[18] (Fig. S10†). However, both types of coordination spheres differ by the combined rotation (α) and nutation (β) of the equatorial $hfac^-$ ion (Fig. 3, Table S3†).

When a symmetrical N_3 binding unit is connected to the metal ion in $[Eu(\mathbf{L1})(hfac)_3]$ and $[Eu_3(\mathbf{L4})(hfac)_9]$, the equatorial $hfac^-$ ion lies opposite to the bound tridentate aromatic unit (β = 176–180°, Fig. 2c and 3a-right). The replacement of a terminal benzimidazole ring by a tertiary amide in the N_2O site in $[Eu(\mathbf{L2})(hfac)_3]$, $[Eu_2(\mathbf{L3})(hfac)_6]$ and $[Eu_3(\mathbf{L4})(hfac)_9]$ shifts this anion toward the bound amide oxygen atom (β = 132–135°, Fig. 2a, b and 3b-right, Table S3†). This distortion is accompanied by a rotation of the plane of the equatorial $hfac^-$ ion around the R = (Eu–O1) + (Eu–O2) direction, which amounts to α = 40–45° for the tridentate N_3 unit and α = 83–88° for the unsymmetrical N_2O ligand (Fig. 3-left, Table S3†). In view of the minor intermolecular packing forces present in the

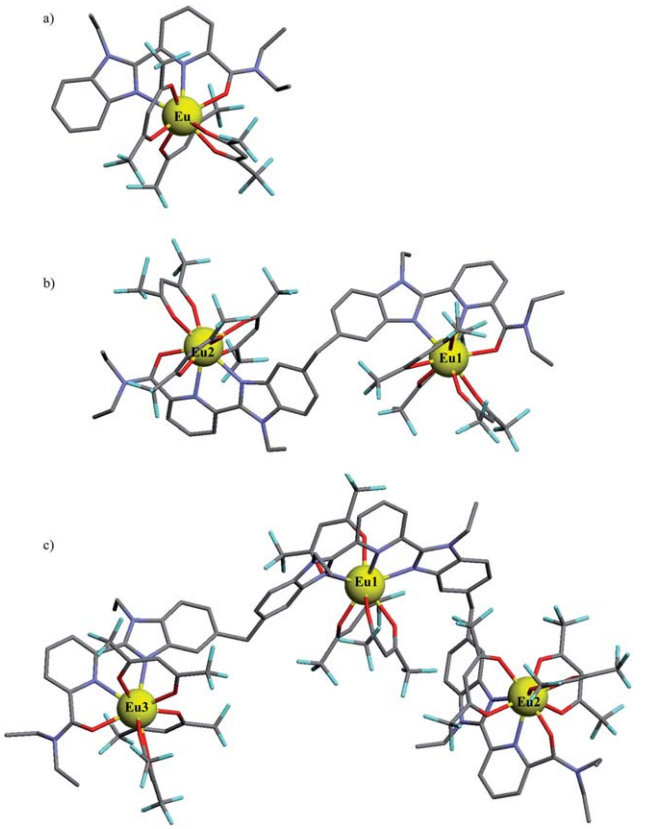

Fig. 2 Perspective views of the molecular structures of the complexes (a) [Eu(**L2**)(hfac)$_3$], (b) [Eu$_2$(**L3**)(hfac)$_6$] and (c) [Eu$_3$(**L4**)(hfac)$_9$] in the solid state. Colors: grey = C-atoms, dark blue = N-atoms, red = O-atoms, pale blue = F-atoms, yellow = Eu-atoms. H atoms are omitted for clarity. Numbering schemes and thermal ellipsoids can be found in Fig. S1–S3.†

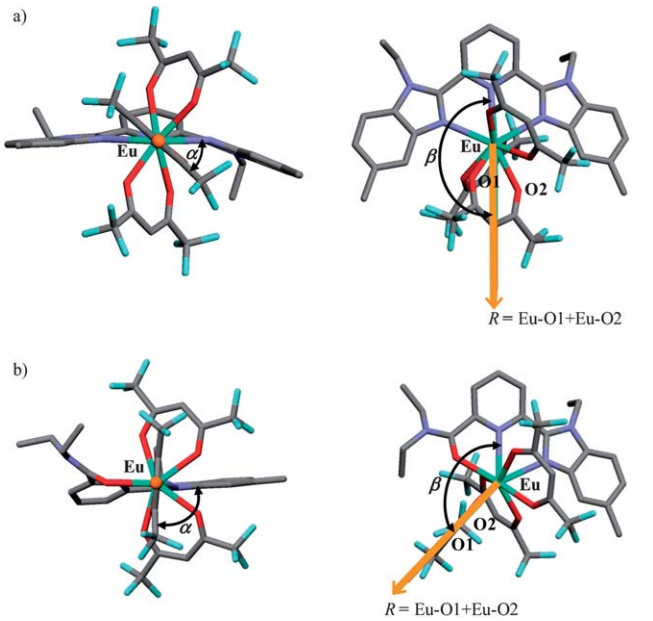

Fig. 3 Perspective views along (left) and perpendicular (right) to the aromatic tridentate ligand in the molecular structures of (a) the central [Eu(N$_3$)(hfac)$_3$] unit and (b) the distal [Eu(N$_2$O)(hfac)$_3$] unit in the trinuclear [Eu$_3$(**L4**)(hfac)$_9$] complex showing the rotation (α) and nutation (β) angles adopted by the equatorial didentate hfac anion (noted here as O1, O2).

crystals, this structural change can be safely assigned to specific stereoelectronic effects induced by the change of donor atoms of the bound tridentate aromatic ligand. We however do not detect any significant intramolecular interligand interactions in [Eu(**L1**)(hfac)$_3$], [Eu(**L2**)(hfac)$_3$], [Eu$_2$(**L3**)(hfac)$_6$] and [Eu$_3$(**L4**)(hfac)$_9$], and this contrasts with a recent structural report focussed on closely related tris(β-diketonate)lanthanide adducts with chiral tridentate bis(oxazolinyl)pyridine ligands.[26] Eu^{III} coordination spheres in **2–4** can be best described as slightly distorted monocapped square antiprisms with the pyridine nitrogen atom occupying the capping position (see Appendix I, Fig. S11 and Tables S4 and S5 in the ESI†). Since the Ln–N and Ln–O bond lengths are standard (Tables S6–S15, ESI†),[18,26,27] calculated ionic radii fit the expected values for nine-coordinate Eu^{III} ($R_{Eu}^{CN=9}$ = 1.12 Å) and Lu^{III} ($R_{Lu}^{CN=9}$ = 1.032 Å),[28] and the associated bond valences display the usual affinity trend $\nu_{Ln,O\text{-amide}} \geq \nu_{Ln,O\text{-hfac}} > \nu_{Ln,N\text{-bzim}} > \nu_{Ln,N\text{-py}}$ (Table S3, S16–S20, ESI†).[29] Compared with the analogous ten-coordinate nitrate complexes [Eu(**L2**)(NO$_3$)$_3$(CH$_3$CN)] and [Eu$_2$(**L3**)(NO$_3$)$_6$(H$_2$O)$_2$],[19] the much stronger interactions between Eu^{III} and the oxygen atoms of the didentate hfac anions ($\nu_{Ln,O\text{-hfac}} \gg \nu_{Ln,O\text{-nitrate}}$) restraints the coordination number to CN = 9 in **2–4**. Finally, the variable intramolecular intermetallic contact distances and helicity indexes H of the diphenylmethane spacers[30] computed for [Eu$_2$(**L3**)(NO$_3$)$_6$(H$_2$O)$_2$] (Eu···Eu = 8.564(1) Å, H = 0.76),[19] [Eu$_2$(**L3**)(hfac)$_6$] (Eu···Eu = 12.594(1) Å, H = 0.52) and [Eu$_3$(**L4**)(hfac)$_9$] (Eu$_1$···Eu$_2$ = 9.593(1) Å, H = 0.71 and Eu$_1$···Eu$_3$ = 12.806(1) Å, H = 0.83) highlight the relative looseness of the helical conformation in these single-stranded helicates (Tables S21 and Appendix 2, ESI†).

Since larger lanthanides (Ln = La–Pr) tend to adopt higher coordination numbers, the reactions of stoichiometric amounts of **L2** (1 eq.), or **L3** (0.5 eq.), or **L4** (0.33 eq.) with [La(hfac)$_3$(diglyme)] (1.0 eq.) in dichloromethane/acetonitrile are expected to give intricate mixtures resulting from the bi-exchange process previously evidenced for **L1** (eqn (1)).[18]

$$2[La(\mathbf{L1})(hfac)_3] \rightleftharpoons [La(\mathbf{L1})_2(hfac)_2]^+ + [La(hfac)_4]^- \quad (1)$$

Accordingly, we were unable to obtain microcrystalline materials with satisfactory elemental analyses for this cation, but maturation in acetonitrile yielded X-ray quality prisms of the double-stranded complex [La(**L2**)$_2$(hfac)$_2$]$_2$[La$_2$(hfac)$_4$(O$_2$CCF$_3$)$_4$]·2CH$_3$CN (**7**). In this complex, the presence of double-stranded cations [La(**L2**)$_2$(hfac)$_2$]$^+$ confirms the operation of equilibrium (1) (Fig. 4a, Table S22 and Fig. S13†), while the formation of the dinuclear [La$_2$(hfac)$_4$(O$_2$CCF$_3$)$_4$]$^{2-}$ anion benefits from the slow retro-Claisen condensation of hfac$^-$ in presence of traces of water, which produces trifluoroacetate anions.[31] Noticeable intra- and intermolecular offset π-stacking interactions involving benzimidazole rings observed in the crystal structure of **7** probably contribute to the driving force shifting equilibrium (1) to the right (Fig. S14†).

The unusual quadruply bridged complex dianion [La$_2$(hfac)$_4$(O$_2$CCF$_3$)$_4$]$^{2-}$ is located on an inversion centre, each

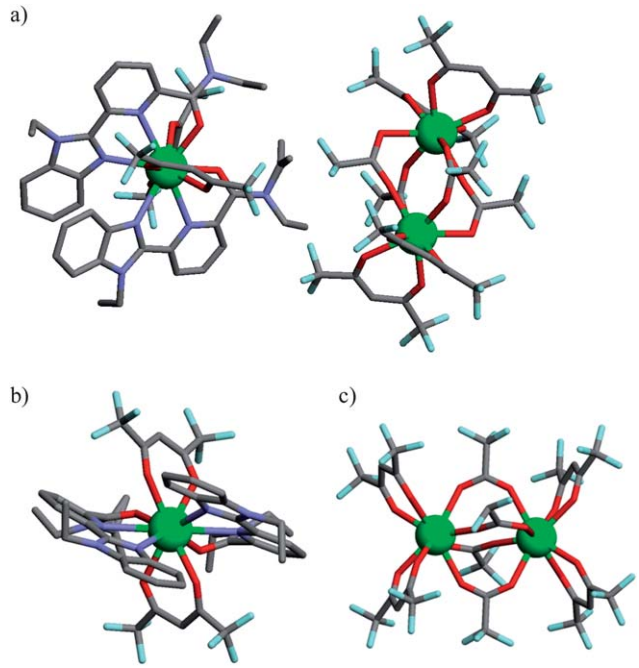

Fig. 4 (a) Perspective view of the molecular structure of the complex salt $[La(\mathbf{L2})_2(hfac)_2]_2[La_2(hfac)_4(O_2CCF_3)_4]$ in the unit cell of **7**. (b) View of the double-stranded $[La(\mathbf{L2})_2(hfac)_2]^+$ cation along its pseudo-twofold axis. (c) View of the dinuclear $[La_2(hfac)_4(O_2CCF_3)_4]^{2-}$ anion perpendicular to its pseudo-twofold axis. Colors: grey = C-atoms, dark blue = N-atoms, red = O-atoms, pale blue = F-atoms, green = La-atoms. H atoms and solvent molecules are omitted for clarity. Numbering scheme and thermal ellipsoids can be found in Fig. S13.†

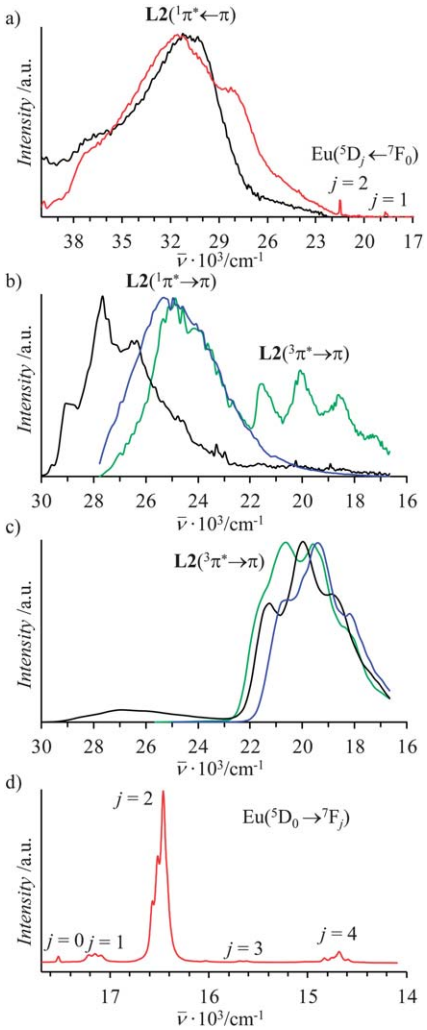

Fig. 5 Solid-state (a) reflectance absorption spectra (293 K), (b) emission spectra ($\bar{\nu}_{exc}$ = 30 300–29 500 cm^{-1}, 77 K), (c) phosphorescence spectra ($\bar{\nu}_{exc}$ = 30 300–29 500 cm^{-1}, delay time after excitation flash 5 ms, 77 K) and (d) luminescence spectra ($\bar{\nu}_{exc}$ = 28 170 cm^{-1} at 293 K) recorded for **L2** (black traces), [Lu(**L2**)(hfac)$_3$] (blue traces), [Gd(**L2**)(hfac)$_3$] (green traces) and [Eu(**L2**)(hfac)$_3$] (red traces).

La atom being eight-coordinated in an approximate square-antiprism arrangement (Fig. S15a†), and separated from its neighbour by a distance of 4.5230(3) Å (Fig. 4c). In the $[La(\mathbf{L2})_2(hfac)_2]^+$ cation, La^{III} is ten-coordinated in a pseudo-bicapped square-antiprismatic geometry (Fig. S15b†), where the two nitrogen atoms of the pyridine rings occupy the opposite capping positions (Fig. 4b, Tables S23–S25†). We conclude (i) that each tridentate N_3 unit in **L1** or in **L4**, or N_2O unit in **L2–L4** are able to coordinate one neutral $Ln(NO_3)_3$ or $Ln(hfac)_3$ moiety, and (ii) that the stronger interaction of the β-diketonate anions excludes additional complexation with solvent molecules. Moreover, the use of the largest cation Ln = La favours the anion/ligand bi-exchange process shown in equilibrium (1), which makes the situation more complicated.

In agreement with the abundant literature dealing with indirect lanthanide sensitization *via* ligand excitation,[32] the absorption spectra of the polyaromatic ligands **L2–L4** are dominated by broad and intense $^1\pi^* \leftarrow {}^1\pi$ transitions in the UV (Fig. 5a, S16a–S17a†). Direct photo-excitation in this energy domain produces dual short-lived fluorescence ($^1\pi^* \rightarrow {}^1\pi$ around 28 000 cm^{-1} with characteristic lifetimes in the sub-nanosecond range, Fig. 5b, S16b–S17b†)[33] and long-lived phosphorescence ($^3\pi^* \rightarrow {}^1\pi$ around 20 500 cm^{-1} with characteristic lifetimes in the millisecond range, Fig. 5c, S16c–S17c and Table S26†). Upon complexation to the $Ln(hfac)_3$ metallic core in $[Gd_m(\mathbf{Lk})(hfac)_{3m}]$ and $[Lu_m(\mathbf{Lk})(hfac)_{3m}]$ (**Lk** = **L2–L4**, m = 1–3), the electronic reorganization shifts both $^1\pi^* \leftarrow {}^1\pi$ absorption[34] and $^1\pi^* \rightarrow {}^1\pi$ fluorescence[35] by *ca.* 2000–4000 cm^{-1} towards lower energies (Fig. 5a and b and S16a, b–S17a, b, and Table S26†), whilst the energy of the $^3\pi^* \rightarrow {}^1\pi$ phosphorescence is not significantly affected (Fig. 5c, S16c–S17c†). Because of the additional paramagnetic coupling produced by Gd(III), both $^1\pi^* \rightarrow {}^3\pi^*$ intersystem crossing and $^3\pi^* \rightarrow {}^1\pi$ emission are boosted, thus leading to stronger $^3\pi^* \rightarrow {}^1\pi$ phosphorescence and shorter $\tau(^3\pi^*)$ lifetimes (Table S26†).[36] Finally, irradiation into the spin-allowed ligand-centred $^1\pi^* \leftarrow {}^1\pi$ transition in $[Eu_m(\mathbf{Lk})(hfac)_{3m}]$ at $\bar{\nu}_{exc}$ = 28 170 cm^{-1} produces intense long-lived red emission signals, arising from quantitative **Lk** → Eu(III) energy transfers followed by $Eu(^5D_1)$ and $Eu(^5D_0)$-centred luminescence (Fig. 5d, S16d–S17d–S18†). The latter emission spectra are dominated by the hypersensitive forced electric dipolar $Eu(^5D_0 \rightarrow {}^7F_2)$ transition centred at 16 340 cm^{-1} leading to absolute quantum yields Φ_{Eu}^{L} in the 24–35% range (Table 1 column 5, solid state, 293 K). Using Einstein's result for the spontaneous radiative emission rate,[37] the radiative lifetime

τ_{rad}^{Eu} of the Eu($^5D_0$) emitting level is deduced from the I_{tot}/I_{MD} ratio (Table 1 column 3), where I_{tot} is the integrated emission for the Eu($^5D_0$) level ($^5D_0 \rightarrow {}^7F_J$, $J = 0$–4) and I_{MD} is the integrated intensity of the magnetic dipolar Eu($^5D_0 \rightarrow {}^7F$) transition (Table S27†). Combined with the characteristic Eu($^5D_0$) lifetime τ_{obs}^{Eu} (Table 1, column 2), we calculate $\Phi_{Eu}^{Eu} = \tau_{obs}^{Eu}/\tau_{rad}^{Eu} = 51$–$60\%$ for the intrinsic Eu-centered quantum yield in these complexes (Table 1, column 4), whereas the sensitization process amounts to $\eta_{sens} = \eta_{ISC}\eta_{en.tr.}^{L\rightarrow Eu} = \Phi_{Eu}^{L}/\Phi_{Eu}^{Eu} = 48$–$59\%$ (Table 1, column 6, *i.e.* η_{ISC} is the efficiency of intersystem crossing and $\eta_{en.tr.}^{L\rightarrow Eu}$ is that of ligand → Eu(III) energy transfer).[35] These photophysical characteristics are comparable with those reported for the analogous tridentate N_3 binding unit bound to Eu(hfac)$_3$ in [Eu(**L1**)(hfac)$_3$] ($\Phi_{Eu}^{Eu} = 86\%$ and $\eta_{sens} = 35\%$ leading to $\Phi_{Eu}^{L} = 30(2)\%$).[18] We conclude that all [Eu$_m$(**L*k***)(hfac)$_{3m}$] complexes (**L*k*** = **L1–L4**, m = 1–3) are fairly emissive and could be exploited as luminescent tags for metal binding in extended polymers involving these binding units.

Speciation of the diamagnetic complexes [Ln$_m$(L*k*)(hfac)$_{3m}$] (Ln = La, Y, Lu, L*k* = L2–L4, *m* = 1–3) in solution

NMR monitoring of the titration of **L2** with [Ln(hfac)$_3$(diglyme)] in CD_3CN shows that (i) equilibrium (2) holds in this solvent for Ln = La, Y, Lu (Fig. 6b, c and e), (ii) the bi-exchange process depicted in equilibrium (1) for Ln = La is severely shifted to the left in CD_3CN so that [La(**L2**)(hfac)$_3$] exists as a single (>95%) complex in solution, but (iii) an additional C_s-symmetrical complex can be detected in excess of metal for the heavier lanthanides Ln = Y, Lu according to equilibrium (3) (Fig. 6d–f and Table S28†).

$$\mathbf{L2} + [\mathrm{Ln(hfac)_3(diglyme)}] \underset{\beta_{1,1}^{\mathrm{Ln(hfac)_3},\mathbf{L2}}}{\rightleftharpoons} [\mathrm{Ln}(\mathbf{L2})(\mathrm{hfac})_3] + \mathrm{diglyme}; \quad (2)$$

$$[\mathrm{Ln}(\mathbf{L2})(\mathrm{hfac})_3] + [\mathrm{Ln(hfac)_3(diglyme)}] \rightleftharpoons [\mathrm{Ln}(\mathbf{L2})(\mathrm{hfac})_2]^+ + [\mathrm{Ln(hfac)_4}]^- + \mathrm{diglyme} \quad (3)$$

Support for equilibrium (3) comes primarily from (i) ^{19}F NMR spectra showing the stepwise replacement of the signal of [Ln(**L2**)(hfac)$_3$] with those of [Ln(**L2**)(hfac)$_2$]$^+$ and [Ln(hfac)$_4$]$^-$ (Fig. S19 and Table S29†) and (ii) the detection of an identical ^{1}H NMR spectroscopic signature corresponding to the dissociated species [Ln(**L2**)(hfac)$_2$]$^+$ (Ln = Y, Lu) whatever its origin is (equilibrium (4), LA is a Lewis Acid such as Ln^{3+},[38] Li^+ or H^+, Fig. S20†).

$$[\mathrm{Ln}(\mathbf{L2})(\mathrm{hfac})_3] + \mathrm{LA}^{z+} \rightleftharpoons [\mathrm{Ln}(\mathbf{L2})(\mathrm{hfac})_2]^+ + [\mathrm{LA(hfac)}]^{(z-1)+} \quad (4)$$

Table 1 Experimental global (Φ_{Eu}^{L}) and intrinsic (Φ_{Eu}^{Eu}) quantum yields, luminescence lifetimes (τ_{obs}^{Eu}) and calculated radiative lifetimes (τ_{rad}^{Eu}), sensitization efficiency (η_{sens}) for [Eu$_m$(**L*k***)(hfac)$_{3m}$] (**L*k*** = **L2–L4**, m = 1–3) in the solid state at 293 K

Compound	τ_{obs}^{Eu}/ms	τ_{rad}^{Eu} [a]/ms	Φ_{Eu}^{Eu} [a] (%)	Φ_{Eu}^{L} (%)	η_{sens} [a] (%)
[Eu(**L2**)(hfac)$_3$]	0.79(1)	1.3(1)	60(7)	28(3)	48(9)
[Eu$_2$(**L3**)(hfac)$_6$]	0.80(1)	1.4(1)	59(7)	35(3)	59(10)
[Eu$_3$(**L3**)(hfac)$_9$]	0.74(2)	1.5(2)	51(6)	24(2)	48(9)

[a] Calculated using standard equations, n taken equal to 1.5.[37]

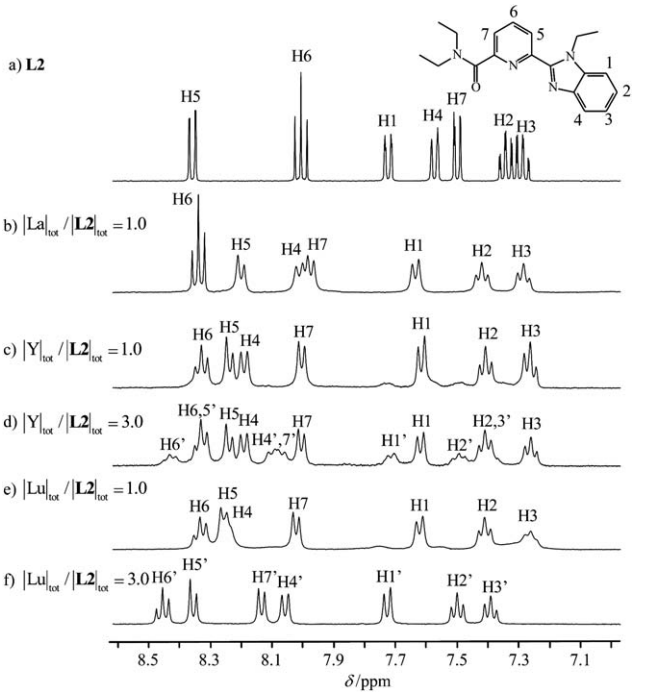

Fig. 6 Aromatic parts of selected ^{1}H NMR spectra recorded upon the titration of **L2** with [Ln(hfac)$_3$(diglyme)] in CD_3CN at 293 K. (a) **L2**, (b) La : **L2** = 1 : 1, (c) Y : **L2** = 1 : 1, (d) Y : **L2** = 3 : 1, (e) Lu : **L2** = 1 : 1 and (f) Lu : **L2** = 3 : 1. Protons with standard numbering correspond to those of [Ln(**L2**)(hfac)$_3$], whereas those with the marks are assigned to the dissociated complex [Ln(**L2**)(hfac)$_2$]$^+$ (see text).

Interestingly, ^{1}H NMR Diffusion-Ordered Spectroscopy (*i.e.* NMR-DOSY) experiments performed on the lutetium complexes in CD_3CN give translational self-diffusion coefficients with a decrease of 6% going from [Lu(**L2**)(hfac)$_3$] ($D_x = 1.25(2) \times 10^{-9}$ m^2 s^{-1}) to [Lu(**L2**)(hfac)$_2$]$^+$ ($D_x = 1.18(1) \times 10^{-9}$ m^2 s^{-1}) despite the smaller molecular weight of the cation. Application of the Stokes–Einstein equation (eqn (5)),[39] corrected for the microfrictional theory (where r_{solv} is the hydrodynamic radius of the solvent, $T = 293$ K is the temperature and $\eta = 3.65 \times 10^{-4}$ kg m^{-1} s^{-1} is the viscosity of acetonitrile at 293 K),[40] provides the pseudo-spherical hydrodynamic radii r_H^x ([Lu(**L2**)(hfac)$_3$]) = 4.91(9) Å and r_H^x ([Lu(**L2**)(hfac)$_2$]$^+$) = 5.21(4) Å, from which pseudo-spherical hydrodynamic volumes V_H^x ([Lu(**L2**)(hfac)$_3$]) = 492(39) Å^3 and V_H^x ([Lu(**L2**)(hfac)$_2$]$^+$) = 593(12) Å^3 and hydrodynamic molecular weight MM_H^x ([Lu(**L2**)(hfac)$_3$]) = 728(43) g mol^{-1} and MM_H^x ([Lu(**L2**)(hfac)$_2$]$^+$) = 878(19) g mol^{-1} are deduced with eqn (6) and (7) ($\rho_H^x = 2.46$ g cm^{-3} is the molecular density and N_{Av} is Avogadro number).[41]

$$D_x = \left(\frac{kT}{6\pi\,\eta r_H^x}\right)\left(1 + 0.695\left(r_{solv}/r_H^x\right)^{2.234}\right) \quad (5)$$

$$V_H^x = \frac{4}{3}\pi\left(r_H^x\right)^3 \quad (6)$$

$$MM_H^x = \rho_H^x V_H^x N_{Av} \quad (7)$$

The counter-intuitive increase of the hydrodynamic molecular weight by 135(47) g mol^{-1} upon release of one hfac$^-$ ion on

going from [Lu(**L2**)(hfac)$_3$] to [Lu(**L2**)(hfac)$_2$]$^+$ (eqn (3)) suggests the partial formation of [Lu(**L2**)(hfac)$_2$]$^+$[Lu(hfac)$_4$]$^-$ ion pairs in solution, a phenomenon often reported when measuring the apparent diffusion coefficients of charged organometallic complexes in organic solvent.[42] Finally, the discrepancy between pseudo-C_s symmetry observed for [Ln(**L2**)(hfac)$_3$] in the solid state (Fig. 2a) and the detection of three equivalent bound hfac anions in solution can be solved for [Y(**L2**)(hfac)$_3$] by using variable-temperature ^{1}H NMR. The slow rate observed for the exchange between axial and equatorial didentate hfac$^-$ anion at 238 K on the NMR time scale is indeed compatible with a C_s point group, while the coalescence of the signals occurring around 275 K in CD_3CN eventually results in a single average NMR peak for the coordinated hfac anions at room temperature (Fig. S21a†). A kinetic Eyring treatment of the data (Fig. S21b†)[43] gives $\Delta H^{\neq}_{exch}$ = 48.3(1.9) kJ mol^{-1} and $\Delta S^{\neq}_{exch}$ = −23.5(0.9) J mol^{-1} K^{-1}, in agreement with a concerted exchange between axial and equatorial hfac anions within the coordination sphere of [Y(**L2**)(hfac)$_3$].[44]

The ^{1}H NMR titrations of the bis-tridentate ligand **L3** with [Ln(hfac)$_3$(diglyme)] (Ln = La, Y, Lu) in acetonitrile mirrors the behaviour depicted for **L2**, with the fixation of a maximum of two Ln(hfac)$_3$ units per ligand (equilibrium (8) with **L*k*** = **L3** and m = 1, 2) and the operation of partial anion dissociation in excess of metal for Y^{III} and Lu^{III} (equilibrium (9) with **L*k*** = **L3** and m = 2, Fig. S22†).

$$\mathbf{L}k + m[\mathrm{Ln(hfac)_3(diglyme)}] \underset{\beta^{\mathrm{Ln(hfac)_3},\mathbf{L}k}_{m,1}}{\rightleftharpoons} [\mathrm{Ln}_m(\mathbf{L}k)(\mathrm{hfac})_{3m}] + m\ \mathrm{diglyme}; \quad (8)$$

$$[\mathrm{Ln}_m(\mathbf{L}k)(\mathrm{hfac})_{3m}] + [\mathrm{Ln(hfac)_3(diglyme)}] \rightleftharpoons [\mathrm{Ln}_m(\mathbf{L}k)(\mathrm{hfac})_{3m-1}]^+ + [\mathrm{Ln(hfac)_4}]^- + \mathrm{diglyme} \quad (9)$$

With the tris-tridentate ligand **L4**, the loading of the three binding sites leads to the formation of the trinuclear [Ln$_3$(**L4**)(hfac)$_9$] complexes for Ln = La, Y, Lu (equilibrium (8) with **L*k*** = **L4** and m = 1–3), but the central N$_3$ coordinating unit is subject to an efficient bi-exchange process with the largest lanthanum cation, which complicates the interpretation of NMR data (Fig. S23†). For the small Ln = Y, Lu cations, the partial dissociation of a terminal hfac anion in excess of metal gives non-negligible amounts of the cationic species [Ln$_3$(**L4**)(hfac)$_8$]$^+$ (equilibrium (9) with **L*k*** = **L4** and m = 3; Fig. S24–S25†).

To sum up, the deleterious trend to dimerization evidenced by single-stranded ligands bound to Ln(NO$_3$)$_3$[16,17] disappears for Ln(hfac)$_3$, and each N$_3$ tridentate binding site found in **L1** or in **L4** (central site) accepts a single Ln(hfac)$_3$ unit for Ln = La, Y, Lu. However, we note that the bi-exchange process depicted in eqn (1) produces variable quantities of the double-stranded complexes with the largest La^{III} cation. This embarrassing competitive reaction is removed by using the unsymmetrical N$_2$O tridentate binding units in **L2**, **L3** and **L4** (distal sites), but the increased electron density on the amide oxygen atom induces partial dissociation of one didentate hfac anion in presence of excesses of Lewis acids, a phenomenon previously noticed for nitrate anions in Ln(NO$_3$)$_3$, but erroneously assigned then to hemilability.[18]

Thermodynamic behaviours and intermetallic interactions in [Ln$_m$(L*k*)(hfac)$_{3m}$] and in [Ln$_m$(L*k*)(NO$_3$)$_{3m}$] (Ln = La, Eu, Y, Lu, L*k* = L1–L4, *m* = 1–3) in solution

The *trans–trans* toward *cis–cis* conformational change of each tridentate binding unit in **L1–L4** accompanying its complexation to Ln(hfac)$_3$ alters the envelope of the ligand-centred n → π* and π → π* transitions, which allows the quantitative evaluation of the coordination process by using spectrophotometric titrations in acetonitrile (Fig. 7).[18] In agreement with speciations established by NMR in this solvent for Ln = La, Eu and Y, factor analyses[45a] confirms the successive fixation of one Ln(hfac)$_3$ unit to each binding site leading to pronounced end points for Ln : **L2** = 1.0 (Fig. 7a), Ln : **L3** = 2.0 (Fig. 7b) and Ln : **L4** = 3.0 (Fig. 7c). Global spectrophotometric data can then be fitted with non-linear least-squares techniques to seven macroscopic equilibria: (10) with k = 1, 2, (11) with m = 1, 2 and (12) with m = 1–3 (Fig. 8a and Table S30†).[45b,c]

$$[\mathrm{Ln(hfac)_3(diglyme)}] + \mathbf{L}k \underset{\beta^{\mathrm{Ln(hfac)_3},\mathbf{L}k}_{1,1}}{\rightleftharpoons} [\mathrm{Ln}(\mathbf{L}k)(\mathrm{hfac})_3] + \mathrm{diglyme}; \quad (10)$$

$$m[\mathrm{Ln(hfac)_3(diglyme)}] + \mathbf{L3} \underset{\beta^{\mathrm{Ln(hfac)_3},\mathbf{L3}}_{1,1}}{\rightleftharpoons} [\mathrm{Ln}_m(\mathbf{L3})(\mathrm{hfac})_{3m}] + m\ \mathrm{diglyme}; \quad (11)$$

$$m[\mathrm{Ln(hfac)_3(diglyme)}] + \mathbf{L4} \underset{\beta^{\mathrm{Ln(hfac)_3},\mathbf{L4}}_{1,1}}{\rightleftharpoons} [\mathrm{Ln}_m(\mathbf{L4})(\mathrm{hfac})_{3m}] + m\ \mathrm{diglyme}; \quad (12)$$

For the smallest Lu^{3+} cation, spectrophotometric titrations confirm the operation of equilibria (10)–(12), followed by further evolution of the absorption spectra in the presence of an excess of metal leading to final smooth end points for Lu : **L2** = 2.0, Lu : **L3** = 3.0 and Lu : **L4** = 3.0–4.0 (Fig. S26†). This specific trend can be assigned to the partial dissociation of one hfac anion from a LuN$_2$O$_7$ coordination site to give [Lu(**L2**)(hfac)$_2$]$^+$, [Lu$_2$(**L3**)(hfac)$_5$]$^+$ and [Lu$_3$(**L4**)(hfac)$_8$]$^+$ according to equilibrium (3). Evolving factor analysis[46] satisfyingly rebuild the spectrophotometric data with the resort of only two absorbing species for **L2** (0.0 < Lu : **L2** < 1.0), respectively three species for **L3** (0.0 < Lu : **L3** < 2), and non-linear least-squares fits restricted within these stoichiometric ranges satisfyingly converge by using eqn (10) and (11) (Fig. 8a). However, major difficulties were encountered for modeling and fitting the titration of **L4** with Lu^{3+} according to eqn (12) because of the early formation of the dissociated species [Lu$_3$(**L4**)(hfac)$_8$]$^+$. The computed stability constants $\log\left(\beta^{\mathrm{Ln(hfac)_3},\mathbf{L4}}_{m,1}\right)$ are only mere estimates (Table S30†), and are therefore not considered for further thermodynamic analysis (Fig. 8).

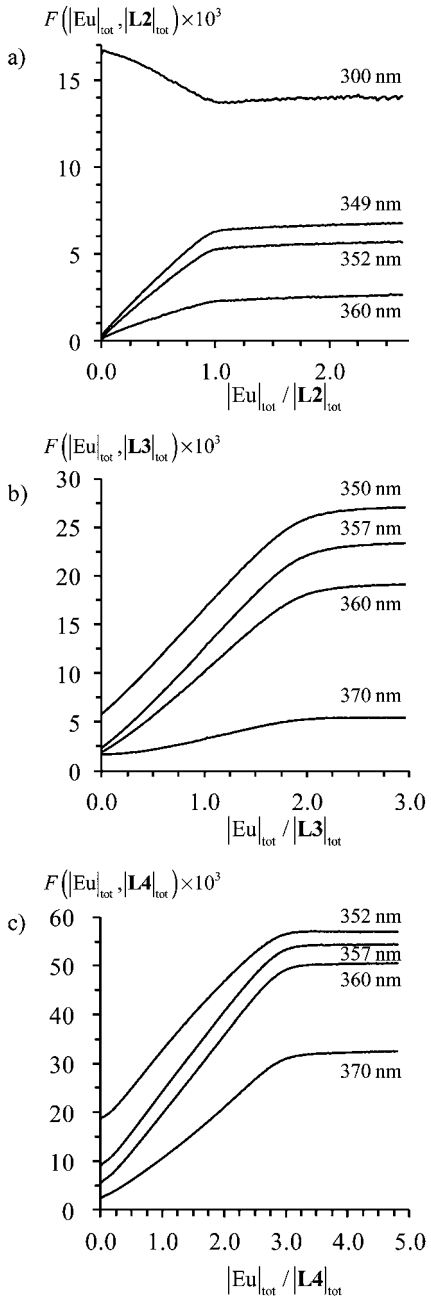

Fig. 7 Variation of corrected molar extinction F (see Appendix 3†) monitored at four different wavelengths observed during the spectrophotometric titrations of (a) **L2**, (b) **L3** and (c) **L4** with [Eu(hfac)$_3$(diglyme)] (298 K, CH_3CN, total ligand concentration: 10^{-4} mol dm^{-3}).

The same procedure was used for collecting a complete set of stability constants with the alternative nitrate salts $Ln(NO_3)_3(H_2O)_3$ (eqn (13)–(15), Table S31 and Fig. 8b).[19]

$$Ln(NO_3)_3(H_2O)_3 + \mathbf{L2} \rightleftharpoons [Ln(\mathbf{L2})(NO_3)_3] + 3H_2O; \quad \beta_{1,1}^{Ln(NO_3)_3,\mathbf{L2}} \tag{13}$$

$$m\,Ln(NO_3)_3(H_2O)_3 + \mathbf{L3} \rightleftharpoons [Ln_m(\mathbf{L3})(NO_3)_{3m}] + 3mH_2O; \quad \beta_{1,1}^{Ln(NO_3)_3,\mathbf{L3}} \tag{14}$$

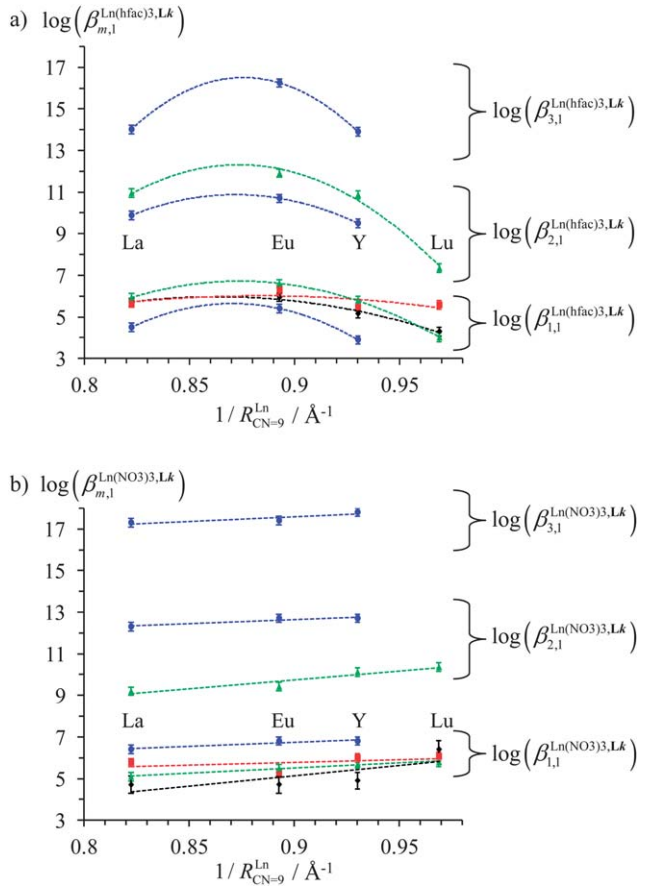

Fig. 8 Variations of (a) $\log\left(\beta_{m,1}^{Ln(hfac)_3,\mathbf{Lk}}\right)$ and (b) $\log\left(\beta_{m,1}^{Ln(NO_3)_3,\mathbf{Lk}}\right)$[19,47] for **L1** (black diamond), **L2** (red squares), **L3** (green triangles) and **L4** (blue disks) as a function of the inverse of nine-coordinate ionic radii along the lanthanide series (CH_3CN, 298 K).[28a] The lines are only guides for the eyes.

$$m\,Ln(NO_3)_3(H_2O)_3 + \mathbf{L4} \rightleftharpoons [Ln_m(\mathbf{L4})(NO_3)_{3m}] + 3mH_2O; \quad \beta_{1,1}^{Ln(NO_3)_3,\mathbf{L4}} \tag{15}$$

As previously noted for the mononuclear complexes [Ln(**L1**)(hfac)$_3$][18] and [Ln(**L1**)(NO$_3$)$_3$],[47] the stability constants obtained with the two different counter-anions (*i.e.* hfac$^-$ *vs.* NO$_3^-$) are comparable when diglyme in [Ln(hfac)$_3$(diglyme)] is replaced by water in Ln(NO$_3$)$_3$(H$_2$O)$_3$. Standard electrostatic trends resulting of the use of nitrate salts (Fig. 8b, *i.e.* $\log\left(\beta_{m,1}^{Ln(NO_3)_3,\mathbf{Lk}}\right)$ linearly increase with the inverse of the lanthanide ionic radii)[48] is replaced with concave bowl-shaped curves upon the use of hexafluoroacetylacetonate anions (Fig. 8a). Based on the trends observed for the bond valences in the molecular structures ($\nu_{Ln,O\text{-}hfac} \gg \nu_{Ln,O\text{-}NO_3}$ and $\nu_{Eu,O\text{-}hfac} > \nu_{Lu,O\text{-}hfac}$, Table S3†), the concave bowl-shaped trend can be tentatively ascribed to the larger bulk produced by hfac$^-$ around small lanthanides. A deeper insight into the thermodynamic complexation processes benefits from the application of the site-binding model (eqn (16)), which expresses the stability constants of eqn (10)–(12) in terms of the two microscopic parameters f_i^{Ln} (= intermolecular affinity of site i for Ln^{III} including desolvation and co-ligand displacement) and $\Delta E_{i,j}^{Ln,Ln}$ (= intermetallic interactions between cations

occupying sites i and j usually written as the Boltzman factor $u_{ij}^{\mathrm{Ln,Ln}} = \mathrm{e}^{-\Delta E_{ij}^{\mathrm{Ln,Ln}}/RT}$) illustrated in Fig. 1a.[48]

$$\beta_{m,1}^{\mathrm{Ln},\mathbf{Lk}} = \mathrm{e}^{-\left(\Delta G_{m,1}^{\mathrm{Ln},\mathbf{Lk}}/RT\right)} = \omega_{m,1}^{\mathrm{chiral}}\omega_{m,1}^{\mathrm{Ln},\mathbf{Lk}}\prod_{i=1}^{m} f_i^{\mathrm{Ln}}\prod_{i<j}\mathrm{e}^{-\Delta E_{ij}^{\mathrm{Ln,Ln}}/RT} \quad (16)$$

Once the statistical factor $\omega_{m,1}^{\mathrm{chiral}}\cdot\omega_{m,1}^{\mathrm{Ln},\mathbf{Lk}}$ quantifying the changes in rotational entropy occurring when the reactants are transformed into products are at hand for each equilibrium (Fig. S27†),[49] a set of seven equations (eqn (17)–(22)) containing six microscopic parameters satisfyingly models the stability constants (Fig. S28†).[19]

$$\beta_{1,1}^{\mathrm{Ln},\mathbf{L1}} = 3f_{\mathrm{N_3(L1)}}^{\mathrm{Ln}} \quad (17)$$

$$\beta_{1,1}^{\mathrm{Ln},\mathbf{L2}} = 3f_{\mathrm{N_2O(L2)}}^{\mathrm{Ln}} \quad (18)$$

$$\beta_{1,1}^{\mathrm{Ln},\mathbf{L3}} = 6f_{\mathrm{N_2O}}^{\mathrm{Ln}} \quad (19)$$

$$\beta_{2,1}^{\mathrm{Ln},\mathbf{L3}} = 9\left(f_{\mathrm{N_2O}}^{\mathrm{Ln}}\right)^2 u_{1-2}^{\mathrm{Ln,Ln}} \quad (20)$$

$$\beta_{1,1}^{\mathrm{Ln},\mathbf{L4}} = 3f_{\mathrm{N_3}}^{\mathrm{Ln}} + 6f_{\mathrm{N_2O}}^{\mathrm{Ln}} \quad (21)$$

$$\beta_{2,1}^{\mathrm{Ln},\mathbf{L4}} = 9\left(f_{\mathrm{N_2O}}^{\mathrm{Ln}}\right)^2 u_{1-3}^{\mathrm{Ln,Ln}} + 18f_{\mathrm{N_3}}^{\mathrm{Ln}} f_{\mathrm{N_2O}}^{\mathrm{Ln}} u_{1-2}^{\mathrm{Ln,Ln}} \quad (22)$$

$$\beta_{3,1}^{\mathrm{Ln},\mathbf{L4}} = 27f_{\mathrm{N_3}}^{\mathrm{Ln}}\left(f_{\mathrm{N_2O}}^{\mathrm{Ln}}\right)^2\left(u_{1-2}^{\mathrm{Ln,Ln}}\right)^2 u_{1-3}^{\mathrm{Ln,Ln}} \quad (23)$$

Non-linear least-square fits of eqn (17)–(23) for X = $hfac^-$ (Table S30†) and X = NO_3^- (Table S31†) provide microscopic free energies for the intermolecular connection of LnX_3 to the tridentate N_3 binding site in **L1** ($\Delta G_{\mathrm{inter}}^{\mathrm{Ln,N_3},\mathbf{L1}} = -RT\ln\left(f_{\mathrm{N_3(L1)}}^{\mathrm{Ln}}\right)$, Fig. 9a) and in **L3–L4** ($\Delta G_{\mathrm{inter}}^{\mathrm{Ln,N_3}} = -RT\ln\left(f_{\mathrm{N_3}}^{\mathrm{Ln}}\right)$, Fig. 9b), and to the tridentate N_2O binding site in **L2** ($\Delta G_{\mathrm{inter}}^{\mathrm{Ln,N_2O},\mathbf{L2}} = -RT\ln\left(f_{\mathrm{N_2O(L2)}}^{\mathrm{Ln}}\right)$, Fig. 9a) and in **L3–L4** ($\Delta G_{\mathrm{inter}}^{\mathrm{Ln,N_2O}} = -RT\ln\left(f_{\mathrm{N_2O}}^{\mathrm{Ln}}\right)$, Fig. 9b),[50] together with vicinal ($\Delta E_{1-2}^{\mathrm{Ln,Ln}} = -RT\ln(u_{1-2}^{\mathrm{Ln,Ln}})$) and distal ($\Delta E_{1-3}^{\mathrm{Ln,Ln}} = -RT\ln(u_{1-3}^{\mathrm{Ln,Ln}})$) intramolecular intermetallic interactions (Fig. 9c). We immediately notice that the comparable free energies of connection of the N_2O binding site found for **L2** with either $Ln(hfac)_3$ or $Ln(NO_3)_3$ (Fig. 9a left) are retained upon connection of the benzimidazole side arms with a single methylene spacers in the segmental ligands **L3** (N_2O–CH_2–N_2O) and **L4** (N_2O–CH_2–N_3–CH_2–N_2O, Fig. 9b left). However, disubstitution of the central N_3 unit in **L4** drastically affects $\Delta G_{\mathrm{inter}}^{\mathrm{Ln,N_3}}$ which is reduced by 40% for $Ln(hfac)_3$, but is increased by the same amount for $Ln(NO_3)_3$ with respect to its value found for the N_3 binding unit in **L1** (Fig. 9a and b right). Although counter-intuitive, the opposite contributions of vicinal $\Delta E_{1-2}^{\mathrm{Ln,Ln}}$ and distal $\Delta E_{1-3}^{\mathrm{Ln,Ln}}$ intermetallic interactions to the global stability of a given polynuclear complex (Fig. 9c) have recently found theoretical justifications for the metal loading of linear oligomers possessing regularly spaced binding sites.[51] Nevertheless the reversal of this trend on going from $[Ln_3(\mathbf{L4})(hfac)_9]$ to $[Ln_3(\mathbf{L4})(NO_3)_9]$ is more puzzling (Fig. 9c).

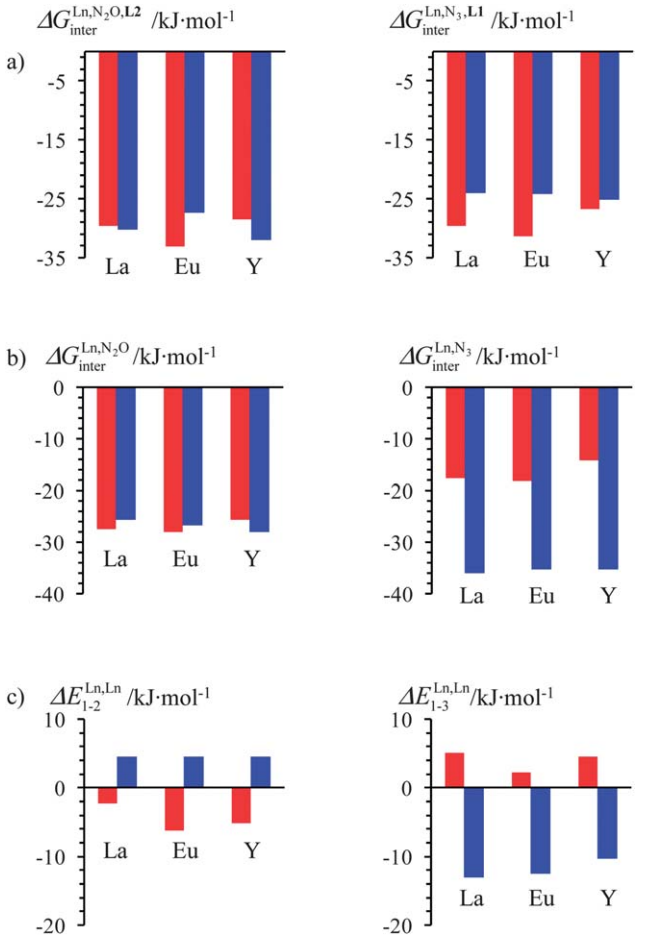

Fig. 9 Representation of the thermodynamic contributions in kJ mol^{-1} corresponding to (a) intermolecular Ln-tridentate site connections in **L1** and **L2**, (b) intermolecular Ln-tridentate site connections in **L3** and **L4** and (c) intermetallic interactions responsible for the global complexation process leading to $[Ln_m(\mathbf{Lk})(hfac)_{3m}]$ (red) and $[Ln_m(\mathbf{Lk})(NO_3)_{3m}]$ (blue) (Ln = La, Eu, Y; **Lk** = **L3–L4**, m = 1–3, CH_3CN, 298 K).

Let's take now the unsaturated macrospecies $[Ln_2(\mathbf{L4})(hfac)_6]$ and $[Ln_2(\mathbf{L4})(NO_3)_6]$ into account for the modelling of the first step of an incomplete metal loading along the strand as depicted in Fig. 1b. The contribution of each microspecies $\beta_{2,1}^{\mathrm{Ln},\mathbf{L4}}(\mathrm{vicinal}) = 18f_{\mathrm{N_3}}^{\mathrm{Ln}} f_{\mathrm{N_2O}}^{\mathrm{Ln}} u_{1-2}^{\mathrm{Ln,Ln}}$ (the two lanthanides occupy neighbouring positions) and $\beta_{2,1}^{\mathrm{Ln},\mathbf{L4}}(\mathrm{distal}) = 9\left(f_{\mathrm{N_2O}}^{\mathrm{Ln}}\right)^2 u_{1-3}^{\mathrm{Ln,Ln}}$ (the two lanthanides occupy the terminal positions) to the macroconstant (eqn (22)) can be calculated by using the pertinent microscopic thermodynamic describers (Table 2).

The systematic larger stabilities found with X = NO_3^- have two different origins. For the vicinal microspecies, the gain in binding energy produced by the complexation of the central N_3 site to $Ln(NO_3)_3$ (Fig. 9b) overcomes the unfavorable nearest neighbour intermetallic interaction (Fig. 9c left). In contrast, the occupancy of the two terminal N_2O sites in the distal microspecies provides comparable stabilization for $Ln(hfac)_3$ and $Ln(NO_3)_3$ (Fig. 9b left), but only the latter lanthanide carrier evidences attractive distal intermetallic interactions (Fig. 9c right). Interestingly, successive loadings of **L4** with $Ln(hfac)_3$ displays no preference between clustering and

Table 2 Thermodynamic macroscopic $\log(\beta_{2,1}^{Ln,L4})$ (eqn (22)) and microscopic $\log(\beta_{2,1}^{Ln,L4}(vicinal))$ and $\log(\beta_{2,1}^{Ln,L4}(distal))$ constants computed for $[Ln_2(\mathbf{L4})(hfac)_6]$ and $[Ln_2(\mathbf{L4})(NO_3)_6]$ (CH_3CN, 298 K)

	$La(hfac)_3$	$Eu(hfac)_3$	$Y(hfac)_3$	$La(NO_3)_3$	$Eu(NO_3)_3$	$Y(NO_3)_3$
$\log(\beta_{2,1}^{Ln,L4})$	9.91	10.71	9.46	12.30	12.58	12.60
$\log(\beta_{2,1}^{Ln,L4}(vicinal))$	9.56	10.46	9.16	11.26	11.36	11.56
$\log(\beta_{2,1}^{Ln,L4}(distal))$	9.65	10.35	9.15	12.25	12.55	12.55
$\beta_{2,1}^{Ln,L4}(distal)/\beta_{2,1}^{Ln,L4}(vicinal)$	1.26	0.79	1.00	9.98	15.81	9.98

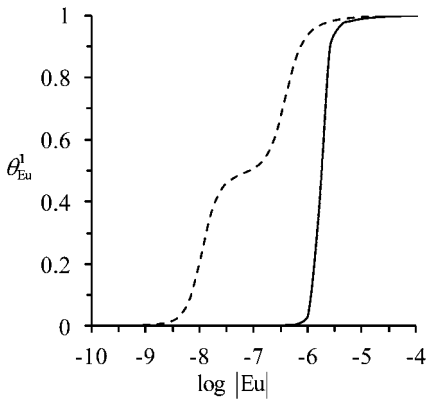

Fig. 10 Predicted binding isotherms for the complexation of $Eu(hfac)_3$ (full trace) and $Eu(NO_3)_3$ (dotted trace) to the multi-tridentate linear polymer **1**. The simulation used $\Delta G_{inter}^{Ln,N_3}$, $\Delta E_{1-2}^{Ln,Ln}$ and $\Delta E_{1-3}^{Ln,Ln}$ shown in Fig. 9 with a total number of $n = 8$ adjacent tridentate binding units (see Appendix 4†).

alternating processes in acetonitrile ($\beta_{2,1}^{Ln,L4}(distal)/\beta_{2,1}^{Ln,L4}(vicinal) \approx 1.0$). The use of $Ln(NO_3)_3$ unambiguously favours the alternated loading with $\beta_{2,1}^{Ln,L4}(distal)/\beta_{2,1}^{Ln,L4}(vicinal) \geq 10$ (Table 2 entry 4).

Conclusion

In a polar aprotic solvent such as acetonitrile, both [Ln(hfac)-(diglyme)] and $Ln(NO_3)_3(H_2O)_3$ are soluble enough to react with the ligands **L1–L4** ligands to give stable single-stranded ternary complexes $[Ln_m(\mathbf{Lk})(X)_{3m}]$ in solution and in the solid state (m = 1–3, **Lk** = **L1–L4**, X = $hfac^-$, NO_3^-). The obvious changes in the affinity of the oxygen donor atom for the central lanthanide cation occurring when poorly coordinating NO_3^- are replaced with $hfac^-$ result in the exclusive formation of pseudo-mono-capped square antiprismatic nine-coordinate [Ln(tridentate)$(hfac)_3$] cores, whilst [Ln(tridentate)$(NO_3)_3$] easily accept additional solvent molecules, both types of complexes being strongly photoluminescent with Ln = Eu^{III}. Upon replacement of the N_3 tridentate binding site with the analogous N_2O unit ($\nu_{Ln,O\text{-}amide} > \nu_{Ln,N\text{-}bzim}$), the equatorial didentate anion moved away from the basal plane without inducing other remarkable changes in the molecular structures. However, solvation processes specific to each type of binding site induces more important variations in solution with the operation of anion/ligand bi-exchange reactions and dimerization processes for N_3 binding sites, and partial anion dissociation for N_2O binding units. These different behaviours can be traced back to different thermodynamic microscopic describers, with a special emphasis on the intramolecular intermetallic interactions between vicinal ($\Delta E_{1-2}^{Ln,Ln}$) and distal ($\Delta E_{1-3}^{Ln,Ln}$) occupied sites, which display opposite trends when **L4** is loaded with $Ln(hfac)_3$ ($\Delta E_{1-2}^{Ln,Ln} < 0$ and $\Delta E_{1-3}^{Ln,Ln} > 0$) or with $Ln(NO_3)_3$ ($\Delta E_{1-2}^{Ln,Ln} > 0$ and $\Delta E_{1-3}^{Ln,Ln} < 0$). Whatever the physical origin of this trend is,[51] these parameters favour clustering upon reacting $Ln(hfac)_3$ with an extended polymer such as **1** (steep binding isotherm in Fig. 10, full trace), whilst reaction with $Ln(NO_3)_3$ lead to a double-humped binding isotherm (Fig. 10, doted trace), which is diagnostic for the formation of the stable alternated micro-species depicted in Fig. 1b (Appendix 4†).[12,13]

Altogether, we have evidenced that $Ln(NO_3)_3$ is better suited to be used as lanthanide carriers for the alternated loading of single-stranded multi-tridentate polymer such as **1** in acetonitrile, and efforts are currently made along this line. However, the relative complexity of the speciation observed in this solvent for the ternary complexes $[Ln_m(\mathbf{Lk})(X)_{3m}]$ (X = $hfac^-$, NO_3^-) may severely hinder a satisfying characterization by using the Ising model. In this context, we note that preliminary titrations of **L1** or **L2** with [Ln$(hfac)_3$(diglyme)] (Ln = La, Y, Lu) in non-polar chloroform shows the straightforward and concomitant step-wise replacement of the ^1H NMR signals of the free ligand (Fig. S29 and Table S32†) and of the ^{19}F NMR signals of the 'free' metal [Ln$(hfac)_3$(diglyme)] (Fig. S30 and Table S29†) with those of $[Ln(\mathbf{Lk})(hfac)_3]$ according to equilibrium 2. No major change occurs when an excess of metal is present (Fig. S30†), and chloroform is promising for the design of Wolf type II metallopolymers with $Ln(hfac)_3$ lanthanide carriers.

Experimental

Solvents and starting materials

These were purchased from Strem, Acros, Fluka AG and Aldrich and used without further purification unless otherwise stated. The ligands **L1**,[18] **L2**,[20] **L3**,[21] **L4** (ref. 22) were prepared according to literature procedures. The hexafluoroacetylacetonate salts [Ln$(hfac)_3$(diglyme)] were prepared from the corresponding oxide (Aldrich, 99.99%).[23] Acetonitrile and dichloromethane were distilled over calcium hydride. Silica-gel plates Merck 60 F254 were used for thin layer chromatography (TLC) and Fluka silica gel 60 (0.04–0.063 mm) or Acros neutral activated alumina (0.050–0.200 mm) was used for preparative column chromatography.

Preparation of the complexes $[Ln_m(Lk)(hfac)_{3m}]$ (Ln = La, Eu, Gd, Lu, Lk = L2–L4, m = 1–3)

Reactions of stoichiometric amounts of **L2** (1 eq.), or **L3** (0.5 eq.), or **L4** (0.33 eq.) with [Ln$(hfac)_3$(diglyme)] (1.0 eq.,

Ln = La, Eu, Gd, Lu) in dichloromethane–acetonitrile yield 70–80% of microcrystalline powders whose elemental analyses were compatible with the formation of the single-stranded complexes $[Ln(\mathbf{L2})(hfac)_3]$, $[Ln_2(\mathbf{L3})(hfac)_6]\cdot xH_2O$ and $[Ln_3(\mathbf{L4})(hfac)_9]\cdot xH_2O$ (Table S1, ESI†). Slow evaporation of concentrated acetonitrile solutions gave X-ray quality prisms for $[Eu(\mathbf{L2})(hfac)_3]$ (**2**), $[Eu_2(\mathbf{L3})(hfac)_6]$ (**3**), $[Eu_3(\mathbf{L4})(hfac)_9]\cdot 5.5CH_3CN$ (**4**), $[Lu(\mathbf{L2})(hfac)_3]$ (**5**), $[Lu_2(\mathbf{L3})(hfac)_6]$ (**6**) and $[La_2(\mathbf{L2})(hfac)_2]_2[La_2(hfac)_4(O_2CCF_3)_4]\cdot 2CH_3CN$ (**7**).

Spectroscopic measurements

^1H, ^{19}F and ^{13}C NMR spectra were recorded at 293 K on Bruker Avance 400 MHz and Bruker DRX-300 MHz spectrometers. Chemical shifts are given in ppm with respect to TMS (^1H) or C_6F_6 (^{19}F). DOSY-NMR data used the pulse sequence implemented in the Bruker program *ledbpgp2s*[52] which employed stimulated echo, bipolar gradients and longitudinal eddy current delay as the *z* filter. The four 2 ms gradient pulses had sine-bell shapes and amplitudes ranging linearly from 2.5 to 50 G cm^{-1} in 32 steps. The diffusion delay was in the range 60–140 ms depending on the analyte diffusion coefficient, and the no. of scans was 32. The processing was done using a line broadening of 5 Hz and the diffusion coefficients were calculated with the Bruker processing package. VT-^1H NMR measurements of samples were measured on a Bruker Avance 400 spectrometer equipped with a variable temperature unit. The integrated intensities of the relevant peaks were obtained by deconvoluting using Matlab or Excel (one Lorentz function per peak) after Fourier transform and phasing of the spectrum using mnova. Fitting of van't Hoff plots was done using Excel. Elemental analyses were performed by K. L. Buchwalder from the Microchemical Laboratory of the University of Geneva. Electronic absorption spectra in the UV-Vis were recorded at 293 K either from solutions in CH_2Cl_2 using quartz cells of 10 or 1 mm path length (transmittance) or from a solid-state sample diluted in MgO by using a Perkin-Elmer Lambda 900 spectrometer equipped with an integration sphere (reflectance). Spectrophotometric titrations were performed with a J&M diode array spectrometer (Tidas series) connected to an external computer. In a typical experiment, 50 cm^3 of ligand in acetonitrile (10^{-4} mol dm^{-3}) were titrated at 293 K with a solution of $[Ln(hfac)_3(diglyme)]$ (10^{-3} mol dm^{-3}) in acetonitrile under an inert atmosphere. After each addition of 0.20 mL, the absorbance was recorded using Hellma optrodes (optical path length 0.1 cm) immersed in the thermostated titration vessel and connected to the spectrometer. Mathematical treatment of the spectrophotometric titrations was performed with factor analysis and with the SPECFIT program.[45] Excitation and emission spectra as well as lifetimes of the triplet states were recorded on a Horiba Jobin Yvon Fluorolog-3 spectrofluorimeter equipped with a Hamamatsu R928P detector and accessories for low-temperature measurements. Spectra were corrected for both excitation and emission responses (excitation lamp, detector and both excitation and emission monochromator responses). Quartz tube sample holders were employed. Luminescence lifetimes of Eu^{III} were determined under excitation at 355 nm provided by a YG 980 QuantelNd:YAG laser while the signal was detected by a photon-counting unit DPM-HVH R928. The output signal from the detector was then fed to a Tektronix TDS 754C 500 MHz bandpass digital oscilloscope and then transferred to a PC for treatment with Origin 8®. Lifetimes are averages of at least three independent measurements. Quantum yield measurements of the solid-state samples were performed on quartz tubes with the help of an integration sphere developed by Frédéric Gumy and Jean-Claude G. Bünzli (Laboratory of Lanthanide Supramolecular Chemistry, École Polytechnique Féderale de Lausanne (EPFL), BCH 1402, CH-1015 Lausanne, Switzerland) and commercialized by GMP S.A. (Renens, Switzerland).

X-Ray crystallography

Summary of crystal data, intensity measurements and structure refinements for $[Eu(\mathbf{L2})(hfac)_3]$ (**2**), $[Eu_2(\mathbf{L3})(hfac)_6]$ (**3**), $[Eu_3(\mathbf{L4})(hfac)_9]\cdot 5.5CH_3CN$ (**4**), $[Lu(\mathbf{L2})(hfac)_3]$ (**5**), $[Lu_2(\mathbf{L3})(hfac)_6]$ (**6**) and $[La_2(\mathbf{L2})(hfac)_2]_2[La_2(hfac)_4(O_2CCF_3)_4]\cdot 2CH_3CN$ (**7**) were collected in Tables S2 and S22 (ESI†). All crystals were mounted on quartz fibers with protection oil. Cell dimensions and intensities were measured at 180–190 K on a Agilent Supernova diffractometer with mirror-monochromated or on a STOE IPDS diffractometer with graphite-monochromated using either Mo-Kα radiation ($\lambda = 0.71073$ Å) or Cu-Kα radiation ($\lambda = 1.54187$). Data were corrected for Lorentz and polarization effects and for absorption. The structures were solved by direct methods (SIR97),[53] all other calculations were performed with Shelx1[54] systems and ORTEP[55] programs. CCDC 905225[24] and 909092–909096 contain the supplementary crystallographic data.

Acknowledgements

Financial support from the Swiss National Science Foundation is gratefully acknowledged. S. P. acknowledges supports from la Ligue contre le Cancer and from Institut National de la Santé et de la Recherche Médicale (INSERM). The work in France was carried out within the COST Action CM1006.

References and notes

1 (*a*) F. Auzel, *Chem. Rev.*, 2004, **104**, 139; (*b*) B. M. van der Ende, L. Aarts and A. Meijerink, *Phys. Chem. Chem. Phys.*, 2009, **11**, 11081.
2 (*a*) F. Wang and X. Liu, *J. Am. Chem. Soc.*, 2008, **130**, 5642; (*b*) M. Haase and H. Schäfer, *Angew. Chem., Int. Ed.*, 2011, **50**, 5808.
3 D. Weng, X. Zheng, X. Chen, L. Li and L. Jin, *Eur. J. Inorg. Chem.*, 2007, 3410.
4 K. Zheng, D. Zhang, D. Zhao, N. Liu, F. Shi and W. Qin, *Phys. Chem. Chem. Phys.*, 2010, **12**, 7620.
5 F. Wang and X. Liu, *Chem. Soc. Rev.*, 2009, **38**, 976.
6 S. V. Eliseeva and J.-C. G. Bünzli, *New J. Chem.*, 2011, **35**, 1165.
7 V. J. Pansare, S. Hejazi, W. J. Faenza and R. K. Prud'homme, *Chem. Mater.*, 2012, **24**, 812.

8 E. M. Chan, D. J. Gargas, P. J. Schuck and D. J. Milliron, *J. Phys. Chem. B*, 2012, **116**, 10561.

9 F. Ferraro and C. Z. Hadad, *J. Phys. Chem. C*, 2012, **116**, 7134.

10 (*a*) M. Cantuel, F. Gumy, J.-C. G. Bünzli and C. Piguet, *Dalton Trans.*, 2006, 2647; (*b*) L. Aboshyan-Sorgho, M. Cantuel, S. Petoud, A. Hauser and C. Piguet, *Coord. Chem. Rev.*, 2012, **256**, 1644.

11 L. Aboshyan-Sorgho, C. Besnard, P. Pattison, K. R. Kittilstved, A. Aebischer, J.-C. G. Bünzli, A. Hauser and C. Piguet, *Angew. Chem., Int. Ed.*, 2011, **50**, 4108.

12 (*a*) G. Koper and M. Borkovec, *J. Phys. Chem. B*, 2001, **105**, 6666; (*b*) M. Borkovec, G. J. M. Koper and C. Piguet, *Curr. Opin. Colloid Interface Sci.*, 2006, **11**, 280; (*c*) G. J. M. Koper and M. Borkovec, *Polymer*, 2010, **51**, 5649.

13 M. Borkovec, J. Hamacek and C. Piguet, *Dalton Trans.*, 2004, 4096.

14 N. Dalla Favera, J. Hamacek, M. Borkovec, D. Jeannerat, G. Ercolani and C. Piguet, *Inorg. Chem.*, 2007, **46**, 9312.

15 For a comprehensive review, see C. Piguet and J.-C. G. Bünzli, *Handbook on the Physics and Chemistry of Rare Earths*, ed. K. A. Gschneidner Jr, J.-C. G. Bünzli and V. K. Pecharsky, Elsevier, Amsterdam, 2009, vol. 40, p. 301.

16 (*a*) H. Nozary, C. Piguet, J.-P. Rivera, P. Tissot, P.-Y. Morgantini, J. Weber, G. Bernardinelli, J.-C. G. Bünzli, R. Deschenaux, B. Donnio and D. Guillon, *Chem. Mater.*, 2002, **14**, 1075; (*b*) H. Nozary, S. Torelli, L. Guénée, E. Terazzi, G. Bernardinelli, B. Donnio, D. Guillon and C. Piguet, *Inorg. Chem.*, 2006, **45**, 2989.

17 (*a*) E. Terazzi, S. Torelli, G. Bernardinelli, J.-P. Rivera, J.-M. Bénech, C. Bourgogne, B. Donnio, D. Guillon, D. Imbert, J.-C. G. Bünzli, A. Pinto, D. Jeannerat and C. Piguet, *J. Am. Chem. Soc.*, 2005, **127**, 888; (*b*) T. B. Jensen, E. Terazzi, K. Buchwalder, L. Guénée, H. Nozary, K. Schenk, B. Heinrich, B. Donnio, D. Guillon and C. Piguet, *Inorg. Chem.*, 2010, **49**, 8601.

18 A. Zaïm, H. Nozary, L. Guénée, C. Besnard, J.-F. Lemonnier, S. Petoud and C. Piguet, *Chem.–Eur. J.*, 2012, **18**, 7155.

19 N. Dalla Favera, L. Guénée, G. Bernadinelli and C. Piguet, *Dalton Trans.*, 2009, 7625.

20 T. Le Borgne, P. Altmann, N. André, J.-C. G. Bünzli, G. Bernardinelli, P.-Y. Morgantini, J. Weber and C. Piguet, *Dalton Trans.*, 2004, 723.

21 K. Zeckert, J. Hamacek, J.-P. Rivera, S. Floquet, A. Pinto, M. Borkovec and C. Piguet, *J. Am. Chem. Soc.*, 2004, **126**, 11589.

22 S. Floquet, N. Ouali, B. Bocquet, G. Bernardinelli, D. Imbert, J.-C. G. Bünzli, G. Hopfgartner and C. Piguet, *Chem.–Eur. J.*, 2003, **9**, 1860.

23 (*a*) W. J. Evans, D. G. Giarikos, M. A. Johnston, M. A. Greci and J. W. Ziller, *J. Chem. Soc., Dalton Trans.*, 2002, 520; (*b*) G. Malandrino, R. Lo Nigro, I. L. Fragalà and C. Benelli, *Eur. J. Inorg. Chem.*, 2004, 500.

24 The crystal structure of **6** (CCDC 905225) has been submitted to *Chem.–Eur. J.*

25 (*a*) S. L. Cockroft, J. Perkins, C. Zonta, H. Adams, S. E. Spey, C. M. R. Low, J. G. Vinter, K. R. Lawson, C. J. Urch and C. A. Hunter, *Org. Biomol. Chem.*, 2007, **5**, 1062; (*b*) C. R. Martinez and B. L. Iverson, *Chem. Sci.*, 2012, **3**, 2191.

26 J. Yuasa, T. Ohno, K. Miyata, H. Tsumatori, Y. Hasegawa and T. Kawai, *J. Am. Chem. Soc.*, 2011, **133**, 9892.

27 A. G. Orpen, L. Brammer, F. H. Allen, O. Kennard, D. G. Watson and R. Taylor, *J. Chem. Soc., Dalton Trans.*, 1989, S1.

28 (*a*) R. D. Shannon, *Acta Crystallogr., Sect. A: Cryst. Phys., Diffr., Theor. Gen. Crystallogr.*, 1976, **32**, 751; (*b*) P. D'Angelo, A. Zitolo, V. Migliorati, G. Chillemi, M. Duvail, P. Vitorge, S. Abadie and R. Spezia, *Inorg. Chem.*, 2011, **50**, 4572; (*c*) P. D'Angelo and R. Spezia, *Chem.–Eur. J.*, 2012, **18**, 11162.

29 (*a*) I. D. Brown and D. Altermatt, *Acta Crystallogr., Sect. B: Struct. Sci.*, 1985, **41**, 244; (*b*) N. E. Breese and M. O'Keeffe, *Acta Crystallogr., Sect. B: Struct. Sci.*, 1991, **47**, 192; (*c*) I. D. Brown, *Acta Crystallogr., Sect. B: Struct. Sci.*, 1992, **48**, 553; (*d*) I. D. Brown, *The Chemical Bond in Inorganic Chemistry*, Oxford University Press, UK, 2002; (*e*) A. Trzesowska, R. Kruszynski and T. J. Bartczak, *Acta Crystallogr., Sect. B: Struct. Sci.*, 2004, **60**, 174; (*f*) A. Trzesowska, R. Kruszynski and T. J. Bartczak, *Acta Crystallogr., Sect. B: Struct. Sci.*, 2005, **61**, 429; (*g*) F. Zocchi, *THEOCHEM*, 2007, **805**, 73; (*h*) I. D. Brown, *Chem. Rev.*, 2009, **109**, 6858.

30 J. H. Brewster, *Top. Curr. Chem.*, 1974, **47**, 29.

31 S. R. Drake, A. Lyons, D. J. Otway and D. J. Williams, *Inorg. Chem.*, 1994, **33**, 1230.

32 For tutorial reviews, see: (*a*) N. Sabbatini, M. Guardigli and I. Manet, *Handbook on the Physics and Chemistry of Rare Earths*, ed. K. A. Gschneidner and L. Eyring, Elsevier, Amsterdam, 1996, vol. 23, p. 69; (*b*) E. G. Moore, A. P. S. Samuel and K. N. Raymond, *Acc. Chem. Res.*, 2009, **42**, 542; (*c*) S. Petoud, *Chimia*, 2009, **63**, 745.

33 J.-F. Lemonnier, L. Guénée, C. Beuchat, T. A. Wesolowski, P. Mukherjee, D. H. Waldeck, K. A. Gogik, S. Petoud and C. Piguet, *J. Am. Chem. Soc.*, 2011, **133**, 16219.

34 (*a*) K. Nakamoto, *J. Phys. Chem.*, 1960, **64**, 1420–1425; (*b*) C. Piguet, B. Bocquet, E. Müller and A. F. Williams, *Helv. Chim. Acta*, 1989, **72**, 323–337.

35 C. Piguet, J.-C. G. Bünzli, G. Bernardinelli, C. G. Bochet and P. Froidevaux, *J. Chem. Soc., Dalton Trans.*, 1995, 83.

36 (*a*) S. Tobita, M. Arakawa and I. Tanaka, *J. Phys. Chem.*, 1984, **88**, 2697; (*b*) S. Tobita, M. Arakawa and I. Tanaka, *J. Phys. Chem.*, 1985, **89**, 5649; (*c*) S. I. Klink, L. Grave, D. N. Reinhoudt, F. C. J. M. van Veggel, M. H. V. Werts, F. Geurts and J. W. Hofstraat, *J. Phys. Chem. A*, 2000, **104**, 5457.

37 $(\tau_{rad})^{-1} = A(\psi_J, \psi_{J'}) = A_{MD,0} n^3 (I_{tot}/I_{MD})$ with $A_{MD,0} = 14.65\ s^{-1}$ for the magnetic dipolar $Eu(^5D_0 \rightarrow {}^7F_1)$ transition and a refractive index $n = 1.5$; A. Aebischer, F. Gumy and J.-C. G. Bünzli, *Phys. Chem. Chem. Phys.*, 2009, **11**, 1346 and references therein.

38 Ln^{3+} is formally obtained from $[Ln(CF_3SO_3)_3(diglyme)]$; H. C. Aspinall, J. L. M. Dwyer, N. Greeves, E. G. McIver and J. C. Woolley, *Organometallics*, 1998, **17**, 1884.

39 (*a*) A. Einstein, *Ann. Phys.*, 1906, **324**, 289; (*b*) A. Einstein, *Ann. Phys.*, 1906, **324**, 371; (*c*) P. Stilbs, *Prog. Nucl. Magn. Reson. Spectrosc.*, 1987, **19**, 1; (*d*) A. R. Waldeck, P. W. Kuchel,

A. J. Lennon and B. E. Chapman, *Prog. Nucl. Magn. Reson. Spectrosc.*, 1997, **30**, 39; (*e*) M. Sharma and S. Yashonath, *J. Phys. Chem. B*, 2006, **110**, 17207; (*f*) A. Macchioni, G. Ciancaleoni, C. Zuccaccia and D. Zuccaccia, *Chem. Soc. Rev.*, 2008, **37**, 479.

40 (*a*) A. Gierer and K. Z. Wirtz, *Z. Naturforsch., A: Astrophys., Phys. Phys. Chem.*, 1953, **8**, 532; (*b*) H.-C. Chen and S.-H. Chen, *J. Phys. Chem.*, 1984, **88**, 5118.

41 The molecular density is estimated with $\rho_H^x = MM_{mol}/V_{mol}$, where the Connolly volume V_{mol} is obtained from the building of the Connolly surface around the molecular structures of [Lu(**L2**)(hfac)$_3$] observed in its crystal structure and by using a probe radius of 2.0 Å for modeling an acetonitrile solvent molecule (V_{CH_3CN} = 36.3 Å^3): (*a*) M. L. Connolly, *Science*, 1983, **221**, 709; (*b*) M. L. Connolly, *J. Appl. Crystallogr.*, 1983, **16**, 548.

42 (*a*) M. Valentini, H. Rüegger and P. S. Pregosin, *Helv. Chim. Acta*, 2001, **84**, 2833; (*b*) E. Martinez-Viviente, P. S. Pregosin, L. Vial, C. Herse and J. Lacour, *Chem.–Eur. J.*, 2004, **10**, 2912; (*c*) P. S. Pregosin, P. G. A. Kumar and I. Fernandez, *Chem. Rev.*, 2005, **105**, 2977; (*d*) M. D. Pluth, B. E. F. Tiedemann, H. van Halbeek, R. Nunlist and K. N. Raymond, *Inorg. Chem.*, 2008, **47**, 1411.

43 (*a*) A. D. Bain, *Prog. Nucl. Magn. Reson. Spectrosc.*, 2003, **43**, 63; (*b*) G. Lente, I. Fabian and A. J. Poe, *New J. Chem.*, 2005, **29**, 759.

44 C. Freund, W. Porzio, U. Giovanella, F. Vignali, M. Pasini, S. Destri, A. Mech, S. Di Pietro, L. Di Bari and P. Mineo, *Inorg. Chem.*, 2011, **50**, 5417.

45 (*a*) E. R. Malinowski and D. G. Howery, *Factor Analysis in Chemistry*, Wiley, New York, Chichester, 1980; (*b*) H. Gampp, M. Maeder, C. J. Meyer and A. D. Zuberbühler, *Talanta*, 1985, **32**, 1133; (*c*) H. Gampp, M. Maeder, C. J. Meyer and A. D. Zuberbühler, *Talanta*, 1986, **33**, 943.

46 B. R. Hall, L. E. Manck, I. S. Tidmarsh, A. Stephenson, B. F. Taylor, E. J. Blaikie, D. A. Vander Griend and M. D. Ward, *Dalton Trans.*, 2011, **40**, 12132.

47 A. Escande, L. Guénée, K.-L. Buchwalder and C. Piguet, *Inorg. Chem.*, 2009, **48**, 1132.

48 (*a*) J. Hamacek, M. Borkovec and C. Piguet, *Dalton Trans.*, 2006, 1473; (*b*) C. Piguet, *Chem. Commun.*, 2010, **46**, 6209.

49 (*a*) S. W. Benson, *J. Am. Chem. Soc.*, 1958, **80**, 5151; (*b*) W. F. Bailey and A. S. Monahan, *J. Chem. Educ.*, 1978, **55**, 489; (*c*) G. Ercolani, C. Piguet, M. Borkovec and J. Hamacek, *J. Phys. Chem. B*, 2007, **111**, 12195.

50 The absolute affinities of a given tridentate binding unit in the multi-tridentate ligand **L3–L4** ($f_{N_3}^{Ln}$, $f_{N_2O}^{Ln}$) differs from those found in the mono-tridentate ligands **L1** or **L2** ($f_{N_3(\mathbf{L1})}^{Ln}$, $f_{N_2O(\mathbf{L2})}^{Ln}$) because of the substitution of the benzimidazole rings with methylene spacers.[19]

51 (*a*) N. Dalla Favera, J. Hamacek, M. Borkovec, D. Jeannerat, F. Gumy, J.-C. G. Bünzli, G. Ercolani and C. Piguet, *Chem.–Eur. J.*, 2008, **14**, 2994; (*b*) T. Riis-Johannessen, N. Dalla Favera, T. K. Todorova, S. M. Huber, L. Gagliardi and C. Piguet, *Chem.–Eur. J.*, 2009, **15**, 12702.

52 D. Wu, A. Chen and C. S. Johnson Jr, *J. Magn. Reson., Ser. A*, 1995, **115**, 260.

53 A. Altomare, M. C. Burla, M. Camalli, G. Cascarano, C. Giacovazzo, A. Guagliardi, G. Moliterni, G. Polidori and R. Spagna, *J. Appl. Crystallogr.*, 1999, **32**, 115.

54 G. M. Sheldrick, *SHELXL97 Program for the Solution and Refinement of Crystal Structures*, University of Göttingen, Germany, 1997.

55 ORTEP3, L. J. Farrugia, *J. Appl. Crystallogr.*, 1997, **30**, 565.

Lanthanide hexafluoroacetylacetonates versus nitrates for the controlled loading of luminescent polynuclear single-stranded oligomers.

Amir Zaïm, Natalia Dalla Favera, Laure Guénée, Homayoun Nozary, Thi Nhu Y Hoang, Svetlana V. Eliseeva, Stéphane Petoud and Claude Piguet*

Supporting Information (71 pages)

Appendix 1: **Geometrical analysis of the Eu(III) coordination spheres in [Eu_3(L4)$(hfac)_9$]**

Each Eu^{III} cation in [Eu_3(**L4**)$(hfac)_9$] is nine-coordinated by the three donor atoms of the tridentate aromatic binding segment of **L4** and by six oxygen atoms of three didentate hexafluoroacetylacetonate anions. In each coordination sphere, the donor atoms occupy the vertices of a distorted polyhedron, which is usually analyzed as a distorted monocapped square antiprism for ternary complexes [Ln(**L**)$(hfac)_3$], where **L** is a tridentate neutral ligand.[S1] When different geometries are to be compared, the use of the famous *S* angle of the 'shape measure' parameter is pertinent,[S2] but it is of more limited interest for characterizing a single set of analogous structures, and we therefore resort to the vectorial shape analysis proposed by LeBorgne et al.[S3] Following this approach, each coordination sphere of Eu(III) can be described as a distorted monocapped square antiprism (MSA), in which O3, O4, O5, O6 and O1, O3, N2, N8 for the central EuN_3O_6 unit (Figure S11a), and O13, O15, O17, O18 and O2, O14, O16, N10 for the distal EuN_2O_7 unit (Figure S11b) define, respectively, the lower and the upper tetragonal faces of the approximate antiprism, the latter being capped by N1 (EuN_3O_6 unit) or by N12 (EuN_2O_7 unit). The computed resulting vector *R*1 (resp. *R*2) corresponds to the sum of the four Eu-donor atoms vectors forming the upper (resp. the lower) tetragonal face of the antiprism. The θ angles between each generating upper Eu-donor vector and *R*1 (resp between each lower Eu-donor vector and *R*2), measure the flatening of the antiprism along the pseudo-C_4 axis defined by the *R*1-*R*2 direction (EuN_3O_6 unit: $34.7 \leq \theta \leq 68.7°$, average 66(5)°for the upper face and 50(15)° for the lower face in Table S4; EuN_2O_7 unit: $51.0 \leq \theta \leq 70.2°$, average 65(4)°for the upper face and 54(3)° for the lower face in Table S5), whereas the ϕ angle (EuN_3O_6 unit: 175.4°; EuN_2O_7 unit: 177.8°) between *R1* and *R*2 indicates a minor bending of the two tetragonal faces ($\phi = 180°$ in an ideal MSA, Tables S2-S3). The rather broad distribution of θ_i suggests some significant distortions from the idealized Johnson capped square antiprism[S4] despite a rather regular distribution of the ω_i angles between the projected vectors of the tetrapodes along the pseudo-C_4 axis (EuN_3O_6 unit: average ω(intra-tetrapode) = 90(10)°, ideal: 90° and average ω(inter-tetrapode) = 45(7)° in Table S4; EuN_2O_7 unit: average

ω(intra-tetrapode) = 90(4)°, ideal: 90° and average ω(inter-tetrapode) = 45(3)° in Table S5) together with a minor deviation of the capping N(pyridine) atom from the pseudo-C_4 axis (EuN_3O_6 unit: α = 2.5°; EuN_2O_7 unit: α = 2.3°). According that all Eu-O and Eu-N bonds are comparable, vector normalization to unit length[S3] does not significantly affect the geometrical analysis (Tables S3-S4). A more rigorous analysis of the coordination sphere of nine-coordinate metal complexes based on the spherical relaxation of the five Johnson polyhedra possessing nine vertices[S4] shows that the distorted central EuN_3O_6 coordination sphere in [Eu_3(**L4**)(hfac)$_9$] can be alternatively described as a 2:5:2 hula hoop (HH), in which the basal plane is defined by N1, N2, N8, O5, O6 related by a five-fold pseudo-symmetry axis with two vertices (O1, O2) and (O3,O4), each related by a two-fold pseudo-symmetry axis, and located on each opposite side of the central pentagone (Fig. S11a).[S9] On the contrary, the less distorted distal EuN_2O_7 coordination spheres in [Eu_3(**L4**)(hfac)$_9$] do not fit this criteria (Fig. S11b).

References

[S1] Y. Kuramochi, T. Nakagawa, T. Yokoo, J. Yuasa, T. Kawai, Y. Hasegawa, *Dalton Trans.* **2012**, *41*, 6634-6640.

[S2] (a) B. E. Robertson, *Inorg. Chem.*, **1977**, *16*, 2735–2742. (b) M. C. Favas, D. L. Kepert, *Prog. Inorg. Chem.* **1981**, *28*, 309–367. (c) J. Xu, E. Radkov, M. Ziegler, K. N. Raymond, *Inorg. Chem.* **2000**, 39, 4156–4164. (d) S. V. Eliseeva, O. V. Kotova, F. Gumy, S. N. Semenov, V. G. Kessler, L. S. Lepnev, J.-C. G. Bünzli, N. P. Kuzmina, *J. Phys. Chem. A*, **2008**, *112*, 3614–3614. (e) T. Harada, Y. Nakano, M. Fujiki, M. Naito, T. Kawai, Y. Hasegawa, *Inorg. Chem.* **2009**, *48*, 11242–11250. (f) B. E. Robertson, *Inorg. Chem.*, **1977**, *16*, 2735–2742. (e) M. C. Favas, D. L. Kepert, *Prog. Inorg. Chem.* **1981**, *28*, 309–367.

[S3] T. Le Borgne, J.-M. Bénech, S. Floquet, G. Bernardinelli, C. Aliprandini, P. Bettens, C. Piguet, *Dalton Trans.* **2003**, 3856-3868.

[S4] A. Ruiz-Martinez, D. Casanova, S. Alvarez, *Chem. Eur. J.* **2008**, *14*, 1291-1303.

Appendix 2: **Geometrical analysis of the helicity in $[Eu_2(L3)(hfac)_6]$, $[Lu_2(L3)(hfac)_6]$ and $[Eu_3(L4)(hfac)_9]$**

We have resorted to the detailed analysis of crooked lines proposed by Brewster[30] for the quantitative determination of the helicity index *H* (eqn S1) associated with the specific organization of the five-carbon chain HC_{ar}-C_{ar}-CH_2-C_{ar}-$C_{ar}H$ in the spacer and numbered C15-C14-C20-C21-C27 in $[Eu_2(\mathbf{L3})(hfac)_6]$ (Figure S2a).

$$H = \frac{V}{V_{max}} = 6\sqrt{3}\pi\frac{L \cdot A}{D^3} \qquad \text{(S1)}$$

According to Brewster,[30] the five atoms are projected onto a plane perpendicular to the helical axis defined by the line passing through the two terminal atoms of the chain. This yields three possible geometrical figures: a line for non-helical organization, a quadrilateral for a regular helical crooked line and two triangles with a common summit for an amphiverse helix.[19] The helicity index computed with eqn (S1) corresponds to the ratio of the volume enclosed by the crooked line (*V*) with respect to the maximum volume (V_{max}) produced when the subtended figure is a circle (*L* is the end to end distance of the helix, *A* is the area of the subtended figure in the projection plane and *D* is the total length of the crooked line, Figure S12a).[30] For $[Eu_2(\mathbf{L3})(hfac)_6]$, $[Lu_2(\mathbf{L3})(hfac)_6]$ and $[Eu_3(\mathbf{L4})(hfac)_9]$, the subtended figures produced by the crooked line of the diphenylmethane spacers are diagnostic for the existence of regular helices (Figure S12b). The introduction of the geometrical data gathered in Table S21 into eqn (S1) gives helicity indexes of H = 0.52 ($[Eu_2(\mathbf{L3})(hfac)_6]$), H = 0.58 ($[Lu_2(\mathbf{L3})(hfac)_6]$) and H = 0.71, 0.83 ($[Eu_3(\mathbf{L4})(hfac)_9]$).

Appendix 3. **Correction of the rough spectrophotometric data for the residual absorption of [Ln(hfac)$_3$]**.

For a given stoichiometric ratio $x = \left|\mathrm{Ln}\right|_{\mathrm{tot}} / \left|\mathbf{L}\boldsymbol{k}\right|_{\mathrm{tot}}$, the absorbance A_x^{λ} recorded at the wavelength λ for a mixture produced by equilibrium (2) can be expressed with the Lambert-Beer relationship (eq S2, l is the pathlength of the incident light within the solution, ε_i^{λ} is the molar absorption coefficient of species i at the wavelength λ).

$$\frac{A_x^{\lambda}}{l} = \varepsilon_{\mathrm{Ln(hfac)_3}}^{\lambda} \left|\mathrm{Ln(hfac)_3}\right| + \varepsilon_{\mathrm{Lk}}^{\lambda} \left|\mathbf{L}\boldsymbol{k}\right| + \varepsilon_{\mathrm{Ln\text{-}Lk}}^{\lambda} \left|\mathrm{Ln}(\mathbf{L}\boldsymbol{k})\mathrm{(hfac)_3}\right| \qquad \text{(S2)}$$

The introduction of the mass balances given in eqs (S3)-(S4) into eq (S2) yields eq (S5), which can be easily rearranged to give eq (S6).

$$\left|\mathrm{Ln}\right|_{\mathrm{tot}} = \left|\mathrm{Ln(hfac)_3}\right| + \left|\mathrm{Ln}(\mathbf{L}\boldsymbol{k})\mathrm{(hfac)_3}\right| \qquad \text{(S3)}$$

$$\left|\mathbf{L}\boldsymbol{k}\right|_{\mathrm{tot}} = \left|\mathbf{L}\boldsymbol{k}\right| + \left|\mathrm{Ln}(\mathbf{L}\boldsymbol{k})\mathrm{(hfac)_3}\right| \qquad \text{(S4)}$$

$$\frac{A_x^{\lambda}}{l} = \varepsilon_{\mathrm{Ln(hfac)_3}}^{\lambda} \left(\left|\mathrm{Ln}\right|_{\mathrm{tot}} - \left|\mathrm{Ln}(\mathbf{L}\boldsymbol{k})\mathrm{(hfac)_3}\right|\right) + \varepsilon_{\mathrm{Lk}}^{\lambda} \left(\left|\mathbf{L}\boldsymbol{k}\right|_{\mathrm{tot}} - \left|\mathrm{Ln}(\mathbf{L}\boldsymbol{k})\mathrm{(hfac)_3}\right|\right) + \varepsilon_{\mathrm{Ln\text{-}Lk}}^{\lambda} \left|\mathrm{Ln}(\mathbf{L}\boldsymbol{k})\mathrm{(hfac)_3}\right| \qquad \text{(S5)}$$

$$F\left(\lambda, \left|\mathrm{Ln}\right|_{\mathrm{tot}}, \left|\mathbf{L}\boldsymbol{k}\right|_{\mathrm{tot}}\right) = \frac{A_x^{\lambda}}{l\left|\mathbf{L}\boldsymbol{k}\right|_{\mathrm{tot}}} - \varepsilon_{\mathrm{Ln(hfac)_3}}^{\lambda} \left(\frac{\left|\mathrm{Ln}\right|_{\mathrm{tot}}}{\left|\mathbf{L}\boldsymbol{k}\right|_{\mathrm{tot}}}\right) = \varepsilon_{\mathrm{Lk}}^{\lambda} + \frac{\left(\varepsilon_{\mathrm{Ln\text{-}Lk}}^{\lambda} - \varepsilon_{\mathrm{Lk}}^{\lambda} - \varepsilon_{\mathrm{Ln(hfac)_3}}^{\lambda}\right)}{\left|\mathbf{L}\boldsymbol{k}\right|_{\mathrm{tot}}} \left|\mathrm{Ln}(\mathbf{L}\boldsymbol{k})\mathrm{(hfac)_3}\right| \qquad \text{(S6)}$$

During the spectrophotometric titration, $F\left(\lambda, \left|\mathrm{Ln}\right|_{\mathrm{tot}}, \left|\mathbf{L}\boldsymbol{k}\right|_{\mathrm{tot}}\right)$ is a constant at a specific wavelength λ_0 for which $\left(\varepsilon_{\mathrm{Ln\text{-}Lk}}^{\lambda_0} - \varepsilon_{\mathrm{Lk}}^{\lambda_0} - \varepsilon_{\mathrm{Ln(hfac)_3}}^{\lambda_0}\right) = 0$. This condition has non-negligible probability to occur only for the formation of a single additional absorbing complex. We also note that any graphical representation of $F\left(\lambda, \left|\mathrm{Ln}\right|_{\mathrm{tot}}, \left|\mathbf{L}\boldsymbol{k}\right|_{\mathrm{tot}}\right)$ as a function of $1/\left|\mathbf{L}\boldsymbol{k}\right|_{\mathrm{tot}}$ becomes linear after the final end point of the titration.

Appendix 4. **Calculation of the binding isotherm in polymer 1**.[12,13]

Let us write the multiple intermolecular complexation process depicted in Fig. 1a between receptor (ligand) **L** and metals M with equilibrium S7.

$$\mathbf{L} + m\,\mathrm{M}^{z+} \rightleftharpoons [\mathbf{L}\mathrm{M}_m]^{mz+} \qquad \beta_{m,1}^{\mathrm{M},\mathbf{L}} \tag{S7}$$

Each macrospecies $[\mathbf{L}\mathrm{M}_m]^{mz+}$ is made up of several microspecies differing in the exact location of the m metals bound to the N sites ($m \leq N$). Each microspecies $\{\boldsymbol{s}_\mathrm{i}\}$-$[\mathbf{L}\mathrm{M}_m]^{mz+}$ can be thus defined by a state vector $\{\boldsymbol{s}_\mathrm{i}\}$, for which each element $s_\mathrm{i} = 1$ when a metal is bound to site i and $s_\mathrm{i} = 0$ when no metal is coordinated. The free energy of complexation $G\{\boldsymbol{s}_\mathrm{i}\}$ associated with the formation of the microspecies $\{\boldsymbol{s}_\mathrm{i}\}$-$[\mathbf{L}\mathrm{M}_m]^{mz+}$ is given in eq S8, where the first term linear in the state variable s_i, corresponds to the sum of free energies of intermolecular metal-binding site connections, and the second quadratic term estimates the sum of the intermetallic pairs interactions limited to nearest neighbours.

$$G\left(\{\boldsymbol{s}_i\}\right) = -\sum_{i=1}^{N} RT \ln\left(f_i^{\mathrm{M}}\right) s_i + \frac{1}{2}\sum_{i=1}^{N}\sum_{j\neq i}^{N} \Delta E_{i,j}^{\mathrm{M},\mathrm{M}} s_i s_j \tag{S8}$$

The associated microscopic formation constant is obtained by the van't Hoff isotherm $\beta_{m,1}^{\mathrm{M},\mathbf{L}}\left(\{\boldsymbol{s}_i\}\right) = \exp\left[-G\left(\{\boldsymbol{s}_i\}\right)/RT\right]$, and the target macroconstant in equilibrium S7 is simply obtained by the sum over all contributing microconstants.

$$\beta_{m,1}^{\mathrm{M},\mathbf{L}} = \sum_{\{\boldsymbol{s}_i\}} \beta_{m,1}^{\mathrm{M},\mathbf{L}}\left(\{\boldsymbol{s}_i\}\right) = \sum_{\{\boldsymbol{s}_i\}} \exp\left[-G_{m,1}^{\mathrm{M},\mathbf{L}}\left(\{\boldsymbol{s}_i\}\right)/RT\right] \tag{S9}$$

The relevant information on the binding properties of M to **L** is contained in the semi-grand partition function Ξ, which is equivalent to the so-called binding polynomial of eq S10, where a_M is the activity of the free metal ion.

$$\Xi = \sum_{m=0}^{N} \beta_{m,1}^{\mathrm{M},\mathbf{L}} \left(a_\mathrm{M}\right)^m \tag{S10}$$

The degree of metalation $\theta_\mathrm{M} = \langle m \rangle / N$, also known in coordination chemistry as the occupancy factor estimating the average of bound metals per receptor, is given by eq S11.

$$\theta_\mathrm{M} = \frac{\langle m \rangle}{N} = \frac{1}{N}\frac{\left|\mathrm{M}_\mathrm{bound}\right|}{\left|\mathbf{L}_\mathrm{tot}\right|} = \frac{1}{N}\frac{d\ln(\Xi)}{d\ln\left(a_\mathrm{M}\right)} \tag{S11}$$

Introducing eq S10 into eq S11, followed by derivation eventually yields

$$\theta_\mathrm{M} = \frac{1}{N}\frac{\sum_{m=0}^{N} m\beta_{m,1}^{\mathrm{M},\mathbf{L}}\left(a_\mathrm{M}\right)^m}{\Xi} = \frac{1}{N}\frac{\sum_{m=0}^{N} m\beta_{m,1}^{\mathrm{M},\mathbf{L}}\left(a_\mathrm{M}\right)^m}{\sum_{m=0}^{N} \beta_{m,1}^{\mathrm{M},\mathbf{L}}\left(a_\mathrm{M}\right)^m} \tag{S12}$$

We note that this approach is not limited to occupancy factors (eq S11), and any alternative techniques, which estimate the semi-grand partition function Ξ for various metal activities, can be

used for deducing the macroconstants (eq S10). For instance, the partition function for the entire chain with N sites shown in Fig. 1a can be computed by suming the elements of the partition vector of the elementary subchain over all possible values of the site variables. This operation can be formulated in matrix notation in eq S13, whereby $\mathrm{V_g}$ is the generating vector initiating the effect of the transfer matrix **T**, which takes into account the change produced in the partition vector when the subchain is extended by one elementary unit on the left. $\tilde{\mathrm{V}}_\mathrm{t}$ is the transposed terminating vector.

$$\Xi = \tilde{\mathrm{V}}_\mathrm{t}\, \mathbf{T}^N\, \mathrm{V}_g \qquad \text{(S13)}$$

For infinite long chains considered in polymers ($N \to \infty$), the partition function is given by $\Xi \sim \lambda^N$, where λ is the largest eigenvalue of the transfer matrix **T**. The transfer matrix adapted to a finite chain with vicinal and distal intermetallic interactions between lanthanides for even N values is shown below and the partition functions can be deduced for N = 8 by using eq S13 with $\tilde{\mathrm{V}}_\mathrm{g} = (1,0,0,0,0,0,0,0)$ and $\tilde{\mathrm{V}}_\mathrm{t} = (1,1,1,1,1,1,1,1)$, whereas the target occupancy factor are obtained by derivation with eq S11.

a)

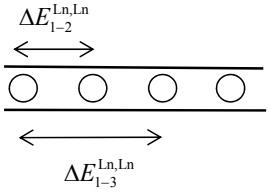

b)

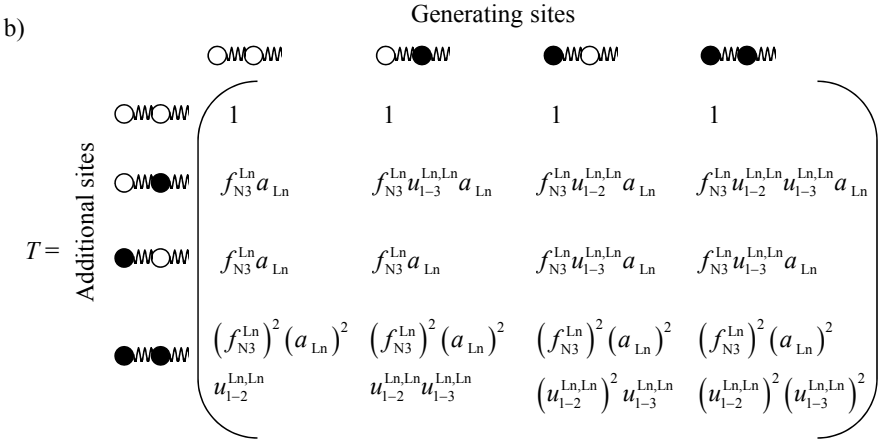

Figure S0 a) Schematic illustration of vicinal $\Delta E_{1\text{-}2}^{\mathrm{Ln,Ln}}$ and distal $\Delta E_{1\text{-}3}^{\mathrm{Ln,Ln}}$ intermetallic pair interactions operating along a linear metal-loaded receptor and b) associated transfer matrix (o = empty site, ● = occupied site) for even N values.[12,13]

Introducing $\Delta G_{\mathrm{inter}}^{\mathrm{Ln,N_3}} = -RT \ln\left(f_{\mathrm{N_3}}^{\mathrm{Ln}}\right)$, $\Delta E_{1\text{-}2}^{\mathrm{Ln,Ln}}$ and $\Delta E_{1\text{-}3}^{\mathrm{Ln,Ln}}$ collected in Tables S29-S30 into the transfer matrix of Fig S0b eventually yields the occupancy factors plotted with respect to the activity of the free metal, thus leading to the so-called binding isotherms depicted in Figure 10.

Table S1 Elemental Analyses for $[Ln_m(\mathbf{L}k)(hfac)_{3m}]$ complexes (k = 2, 3, 4; Ln = La, Eu, Gd, Lu).

Compounds	MM/ g·mol^{-1}	%C found	%H found	%N found	%C calc	%H calc	%N calc
$[La(\mathbf{L2})_2(hfac)_2]_2$ $[La_2(hfac)_4(O_2CCF_3)_4]\cdot 2.4\ H_2O$	1976.86	37.26	2.52	5.57	37.67	2.45	5.67
$[Eu(\mathbf{L2})(hfac)_3]$	1095.52	37.23	2.35	5.13	37.28	2.30	5.11
$[Gd(\mathbf{L2})(hfac)_3]$	1100.81	37.19	2.34	4.94	37.09	2.29	5.09
$[Lu(\mathbf{L2})(hfac)_3]$	1118.53	36.45	2.31	5.08	36.51	2.25	5.01
$[Eu_2(\mathbf{L3})(hfac)_6].1.1\ H_2O$	2203.06	37.26	2.31	5.01	37.62	2.29	5.09
$[Gd_2(\mathbf{L3})(hfac)_6].1.2\ H_2O$	2213.64	37.06	2.36	5.11	37.44	2.28	5.06
$[Lu_2(\mathbf{L3})(hfac)_6].0.5\ H_2O$	2249.06	36.71	2.27	4.96	36.85	2.24	4.98
$[Eu_3(\mathbf{L4})(hfa)_9].1.4\ H_2O$	3355.64	38.39	2.28	5.15	38.66	2.22	5.43
$[Gd_3(\mathbf{L4})(hfa)_9]$	3371.50	38.58	2.42	5.22	38.47	2.21	5.40

Table S2 Summary of crystal data, intensity measurements and structure refinements for [Eu(**L2**)(hfac)$_3$] (**2**), [Lu(**L2**)(hfac)$_3$] (**5**), [Eu$_2$(**L3**)(hfac)$_6$] (**3**), [Lu$_2$(**L3**)(hfac)$_6$] (**6**) , [Eu$_3$(**L4**)(hfa)$_9$]·5.5CH$_3$CN (**4**).

	[Eu(**L2**)(hfac)$_3$] (**2**)	[Lu(**L2**)(hfac)$_3$] (**5**)	[Eu$_2$(**L3**)(hfac)$_6$] (**3**)	[Lu$_2$(**L3**)(hfac)$_6$] (**6**)[a]	[Eu$_3$(**L4**)(hfac)$_9$] (**4**)
Empirical formula	$C_{34}H_{25}F_{18}N_4O_7Eu$	$C_{38}H_{31}F_{18}N_6O_7Lu$	$C_{69}H_{50}F_{36}N_8O_{14}Eu_2$	$C_{69}H_{50}F_{36}N_8O_{14}\ Lu_2$	$C_{119}H_{90.5}F_{54}N_{18.5}O_{20}Eu_3$
Formula weight	1095.54	1200.66	2203.09	2249.11	3581.48
Temperature	180 (2) K	180(2) K	180(2) K	180(2) K	180(2) K
Wavelength	0.71073 Å	1.54184 Å	0.71073 Å	1.54184 Å	1.54184 Å
Crystal System, Space group	Monoclinic, $P2_1/c$	Triclinic, P-1	Monoclinic, $P2_1/c$	Triclinic, P-1	Triclinic, P-1
Unit cell dimensions	a = 12.4834 (1) Å	a = 12.2354 (2) Å	a = 21.9162 (8) Å	a = 12.6357 (4) Å	a = 17.6614 (4) Å
	b = 18.5861 (2) Å	b = 14.4044 (2) Å	b = 18.3619 (8) Å	b = 17.6457 (5) Å	b = 19.7308 (4) Å
	c = 20.5491 (3) Å	c = 14.8029 (3) Å	c = 24.8681 (9) Å	c = 18.3732 (6) Å	c = 23.4654 (5) Å
	α = 90°	α = 77.3039 (16)°	α = 90°	α = 83.577 (3)°	α = 95.2886 (19)°
	β = 117.5470 (10)°	β = 72.1925 (19)°	β = 122.872 (2)°	β = 89.254 (3)°	β = 96.6780 (19)°
	γ = 90°	γ = 68.6551 (17)°	γ = 90°	γ = 88.667 (2)°	γ = 114.691 (2)°
Volume in Å^3	4227.24 (8)	2296.18 (8)	8405.1 (6)	4069.6 (2)	7288.7 (3)
Z, Calculated density	4, 1.721 Mg/m^3	2, 1.737 Mg/m^3	4, 1.741 Mg/m^3	2, 1.835 Mg/m^3	2, 1.632 Mg/m^3
Absorption coefficient	1.612 mm^{-1}	5.275 mm^{-1}	1.622 mm^{-1}	5.888 mm^{-1}	10.343 mm^{-1}
F(000)	2152	1180	4328	2196	3538
Theta range for data collection	1.98 to 29.59°	3.16 to 73.39 °	1.48 to 25.71°	2.52 to 79.77 °	2.79 to 73.46 °

Table S2 (continued)

Limiting indices	-15<=*h*<=17,	-14<=*h*<=15,	-26<=*h*<=26,	-15<=*h*<=15,	-16<=*h*<=21,
	-23<=*k*<=25,	-17<=*k*<=17,	-22<=*k*<=22,	-21<=*k*<=21,	-24<=*k*<=20,
	-26<=*l*<=25	-18<=*l*<=18	-30<=*l*<=30	-22<=*l*<=22	-29<=*l*<=26
Reflections collected / unique	70644 / 10864	34152 / 9099	74386 / 15887	24565 / 24565	53489 / 28544
	[*R*(int) = 0.0311]	[*R*(int) = 0.0283]	[*R*(int) = 0.0976]	[*R*(int) = 0.0000]	[*R*(int) = 0.0398]
Completeness to theta	26.32°/ 99.9 %	73.39°/ 98.4%	25.71°/ 99.2%	68.00°/ 99.2 %	66.97°/ 99.9 %
Data / restraints / parameters	10864 / 12 / 573	9099 / 0 / 634	15887 / 34 / 1132	24565 / 18 / 1143	28544 / 2 / 1894
Goodness-of-fit on F^2	1.049	1.037	1.027	1.020	1.046
Final *R* indices [$I>2\sigma(I)$]	R_1 = 0.0412,	R_1 = 0.0264,	R_1 = 0.0640,	R_1 = 0.0606,	R_1 = 0.0567,
	ωR_2 = 0.1059	ωR_2 = 0.0693	ωR_2 = 0.1592	ωR_2 = 0.1655	ωR_2 = 0.1455
R indices (all data)	R_1 = 0.0504,	R_1 = 0.0277,	R_1 = 0.0863,	R_1 = 0.0694,	R_1 = 0.0715,
	ωR_2 = 0.1150	ωR_2 = 0.0704	ωR_2 = 0.1708	ωR_2 = 0.1742	ωR_2 = 0.1585
Largest diff. peak and hole	1.827 and -1.108 e.Å^{-3}	0.801 and -0.526 e.Å^{-3}	1.391 and -1.385 e.Å^{-3}	1.785 and -1.463 e.Å^{-3}	1.328 and -1.342 e.Å^{-3}

[a] The crystal is a non merohedral twin, the ratio of the twin components beign 0.47:0.53. The structure refinement was performed using HKLF 5 Shelx reflection file

Table S3 Ionic radius (R_{Ln}),[a] average bond valences ($\nu_{Ln,j}$),[b] bond valence sums ($V_{Ln,j}$)[c] and rotation (α) and nutation (β) angles[d] in the crystal structures of $[Ln_m(\mathbf{Lk})(hfac)_{3m}]$ and $[Ln_m(\mathbf{Lk})(NO_3)_{3m}]$ (m = 1-3, **Lk** = **L1**-**L4**).

Complexes	Type [e]	R_{Ln}/Å	$\nu_{Ln,N\text{-}py}$	$\nu_{Ln,N\text{-}bzim}$	$\nu_{Ln,O\text{-}amide}$	$\nu_{Ln,O\text{-}hfac}$	$\nu_{Ln,O\text{-}NO3}$	V_{Ln}	α/°	β/°	Ref.
$[Eu(\mathbf{L1})(hfac)_3]$	NNN	1.06	0.33	0.36(1)	-	0.39(4)	-	3.37	40.2	176.8	18
$[Lu(\mathbf{L1})(hfac)_3]$	NNN	1.00	0.25	0.340(2)	-	0.35(6)	-	3.00	44.5	180.0	18
$[Eu(\mathbf{L2})(hfac)_3]$	NNO	1.10	0.30	0.34	0.38	0.36(2)	-	3.15	87.9	132.7	This work
$[Lu(\mathbf{L2})(hfac)_3]$	NNO	1.01	0.29	0.30	0.39	0.34(4)	-	3.04	83.6	133.6	This work
$[Eu(\mathbf{L2})(NO_3)_3(CH_3CN)]$	NNO	1.17	0.28	0.36	0.41	-	0.27(2)	2.98	-	-	19
$[Eu_2(\mathbf{L3})(hfac)_6]$	NNO	1.10	0.28(1)	0.322(1)	0.390(4)	0.36(3)	-	3.16(3)	85(3)	134(2)	This work
$[Lu_2(\mathbf{L3})(hfac)_6]$	NNO	1.02	0.31(1)	0.30(2)	0.40(1)	0.34(4)	-	3.02(7)	83(2)	133.8(6)	24
$[Eu_2(\mathbf{L3})(NO_3)_6(H_2O)_2]$	NNO	1.16	0.28	0.39	0.42	-	0.26(3)	2.98	-	-	19
$[Eu_3(\mathbf{L4})(hfac)_9]$	NNN	1.09	0.27	0.36(1)	-	0.36(4)	-	3.13	40.0	176.1	This work
	NNO	1.09	0.30(1)	0.32(2)	0.36(1)	0.36(3)	-	3.11(3)	86(4)	135(4)	This work

[a] Ionic radius for Ln^{III} calculated according to Shannon's definition with r(N) = 1.46 Å, r(O) = 1.35 Å and r(O-nitrate) = 1.31 Å.[28] [b] $\nu_{Ln,j} = e^{\left[\left(R_{Ln,j} - d_{Ln,j}\right)/b\right]}$ with valence bond parameters $R_{Ln,N}$ and $R_{Ln,O}$ taken from ref 29e,f and b = 0.37 Å.[29] [c] $V_{Ln} = \sum_j \nu_{Ln,j}$.[29] [d] α is the interplanar angle between the equatorial didentate hfac anion and the plane defined by the three coordinated donor atom of the aromatic ligand. β is the angle between the Eu-N_{py} and the Eu-O1(hfac)+Eu-O2(hfac) direction (Figure 3). [e] Sequence of donor atoms in the tridentate aromatic ligand.

Table S4 Selected structural data for the Eu1 lanthanide coordination sphere in $[Eu_3(\mathbf{L4})(hfac)_9]$ (**4**).

		Angle ϕ [a] / °	
	EuN_3O_6		Perfect MSA[b]
	Standard	Normalized	
R^1-Eu-R^2	175.4	175.7	180
		Angle α [a] / °	
	EuN_3O_6		Perfect MSA[b]
	Standard	Normalized	
	2.5	2.5	0
		Angles θ_t [a] / °	
	EuN_3O_6		Perfect MSA[b]
	Standard	Normalized	
R^1-Eu-O3	66.0	65.9	ρ
R^1-Eu-O1	70.5	70.6	ρ
R^1-Eu-N2	68.7	68.5	ρ
R^1-Eu-N8	58.5	58.7	ρ
R^2-Eu-O2	64.1	64.1	ρ
R^2-Eu-O4	63.8	63.9	ρ
R^2-Eu-O5	40.6	40.4	ρ
R^2-Eu-N6	34.7	34.9	ρ

		Angles ω_{ij} [a] / °	
	EuN_3O_6		Perfect MSA[b]
	Standard	Normalized	
Proj[N2]-Eu-Proj[O3][c]	80.1	80.1	90
Proj[O3]-Eu-Proj[N8]	98.0	98.0	90
Proj[N8]-Eu-Proj[O1]	75.5	75.5	90
Proj[O1]-Eu-Proj[N2]	106.4	106.4	90
Proj[O2]-Eu-Proj[O5]	95.4	95.5	90
Proj[O5]-Eu-Proj[O4]	90.1	90.2	90
Proj[O4]-Eu-Proj[O6]	85.9	85.9	90
Proj[O6]-Eu-Proj[O2]	88.5	88.5	90
Proj[O2]-Eu-Proj[N2]	54.5	54.5	45

Proj[O2]-Eu-Proj[O1]	51.9	51.8	45
Proj[O5]-Eu-Proj[N2]	40.9	41.0	45
Proj[O5]-Eu-Proj[O3]	39.2	39.2	45
Proj[O4]-Eu-Proj[O3]	51.0	51.0	45
Proj[O4]-Eu-Proj[N8]	47.1	47.0	45
Proj[O6]-Eu-Proj[O1]	36.6	36.7	45
Proj[O6]-Eu-Proj[N8]	38.9	38.9	45

---

[a] For the definition of ϕ, α, θ_i and ω_{ij}, see Fig. S11a. The error in the angles is typically 0.5°. [b] MSA = monocapped square antiprism. [c] Proj[O*i*] and Proj[N*i*] are the projections of O*i* and respectively N*i* along the R^2-R^1 direction onto a perpendicular plane passing through the lanthanide atom. R^1 = Eu-O1 + Eu-N2 + Eu-O3 + Eu-N8 and R^2 = Eu-O2 + Eu-O4 + Eu-O5 + Eu-O6.

Table S5 Selected structural data for the Eu3 lanthanide coordination sphere in $[Eu_3(\mathbf{L4})(hfac)_9]$ (**4**).

		Angle ϕ [a] / °	
	EuN_2O_7		Perfect MSA[b]
	Standard	Normalized	
R^1-Eu-R^2	177.8	178.8	180
		Angle α [a] / °	
	EuN_3O_6		Perfect MSA[b]
	Standard	Normalized	
	2.3	2.6	0
		Angles θ_t [a] / °	
	EuN_3O_6		Perfect MSA[b]
	Standard	Normalized	
R^1-Eu-O2	64.9	62.8	ρ
R^1-Eu-O14	70.2	69.9	ρ
R^1-Eu-O16	64.9	65.1	ρ
R^1-Eu-N10	60.9	63.0	ρ
R^2-Eu-O13	57.2	56.9	ρ
R^2-Eu-O15	53.1	52.9	ρ
R^2-Eu-O17	51.0	51.2	ρ
R^2-Eu-O18	55.3	55.7	ρ

		Angles ω_{ij} [a] / °	
	EuN_3O_6		Perfect MSA[b]
	Standard	Normalized	
Proj[O2]-Eu-Proj[O14][c]	86.1	86.6	90
Proj[O14]-Eu-Proj[N10]	96.7	96.3	90
Proj[N10]-Eu-Proj[O16]	84.3	84.3	90
Proj[O16]-Eu-Proj[O2]	92.8	92.8	90
Proj[O13]-Eu-Proj[O17]	89.4	89.5	90
Proj[O17]-Eu-Proj[O18]	90.8	89.6	90
Proj[O18]-Eu-Proj[O15]	88.9	88.9	90
Proj[O15]-Eu-Proj[O13]	90.9	92.0	90
Proj[O17]-Eu-Proj[O2]	45.7	45.1	45
Proj[O17]-Eu-Proj[O14]	40.4	41.1	45

Proj[O18]-Eu-Proj[O2]	45.1	44.6	45
Proj[O18]-Eu-Proj[O16]	47.8	48.8	45
Proj[O15]-Eu-Proj[N10]	43.1	43.7	45
Proj[O15]-Eu-Proj[O16]	41.2	40.1	45
Proj[O13]-Eu-Proj[O14]	49.0	48.5	45
Proj[O13]-Eu-Proj[N10]	47.7	48.3	45

---

[a] For the definition of ϕ, α, θ_i and ω_{ij}, see Fig. S11. The error in the angles is typically 0.5°. [b] MSA = monocapped square antiprism. [c] Proj[O*i*] and Proj[N*i*] are the projections of O*i* and respectively N*i* along the R^2-R^1 direction onto a perpendicular plane passing through the lanthanide atom. R^1 = Eu-O2 + Eu-O14 + Eu-O16 + Eu-N10 and R^2 = Eu-O13 + Eu-O15 + Eu-O17 + Eu-O18.

Table S6 Selected bond distances (Å), bond angles (°) in [Eu(**L2**)(hfac)$_3$] (**2**).

Bond distances (Å)

Atom 1	Atom 2	Distance	Atom 1	Atom 2	Distance
Eu(1)	O(1)	2.396(3)	Eu(1)	O(6)	2.421(3)
Eu(1)	O(2)	2.450(3)	Eu(1)	O(7)	2.445(3)
Eu(1)	O(3)	2.417(3)	Eu(1)	N(1)	2.612(3)
Eu(1)	O(4)	2.394(2)	Eu(1)	N(3)	2.566(3)
Eu(1)	O(5)	2.397(2)			

Angles (°)

At. 1	At. 2	At. 3	Angle	At. 1	At. 2	At. 3	Angle
O(1)	Eu(1)	O(2)	70.32(9)	O(4)	Eu(1)	O(6)	77.51(9)
O(1)	Eu(1)	O(3)	75.48(10)	O(4)	Eu(1)	O(7)	147.64(9)
O(1)	Eu(1)	O(5)	81.63(9)	O(4)	Eu(1)	N(1)	128.83(9)
O(1)	Eu(1)	O(6)	136.29(9)	O(4)	Eu(1)	N(3)	79.33(9)
O(1)	Eu(1)	O(7)	73.75(9)	N(3)	Eu(1)	N(1)	61.62(10)
O(1)	Eu(1)	N(1)	63.67(9)	O(5)	Eu(1)	O(2)	71.27(9)
O(1)	Eu(1)	N(3)	125.16(9)	O(5)	Eu(1)	O(3)	138.94(9)
O(2)	Eu(1)	N(1)	120.26(10)	O(5)	Eu(1)	O(6)	141.89(9)
O(2)	Eu(1)	N(3)	138.86(9)	O(5)	Eu(1)	O(7)	132.25(9)
O(3)	Eu(1)	O(2)	69.09(9)	O(5)	Eu(1)	N(1)	66.36(9)
O(3)	Eu(1)	O(6)	70.12(9)	O(5)	Eu(1)	N(3)	73.97(9)
O(3)	Eu(1)	O(7)	72.58(9)	O(6)	Eu(1)	O(2)	118.75(10)
O(3)	Eu(1)	N(1)	127.86(9)	O(6)	Eu(1)	O(7)	70.84(9)
O(3)	Eu(1)	N(3)	146.64(9)	O(6)	Eu(1)	N(1)	120.70(9)
O(4)	Eu(1)	O(1)	137.39(9)	O(6)	Eu(1)	N(3)	78.19(9)
O(4)	Eu(1)	O(2)	69.69(9)	O(7)	Eu(1)	O(2)	132.46(9)
O(4)	Eu(1)	O(3)	103.06(9)	O(7)	Eu(1)	N(1)	66.11(9)
O(4)	Eu(1)	O(5)	72.22(9)	O(7)	Eu(1)	N(3)	87.67(9)

Table S7 Selected least-squares planes data for [Eu(**L2**)(hfac)$_3$] (**2**).

Least-square planes

Least-squares planes description	Abbreviation	Max. deviation/Å	Atom
Pyridine N1, C1, C2, C3, C4, C5	Py	0.0216 (12)	N1
Benzimidazole N3, C12, C13, C14, C15, C16, C17, N4, C11	Bz	0.0148 (11)	N3
Hexafluoroacetylacetonate O4, C25, C26, C27, O5, Eu1	Hfa I	0.0236 (11)	C27
Hexafluoroacetylacetonate O6, C32, C31, C30, O7, Eu1	Hfa II	0.0184 (11)	C30
Hexafluroacetylacetonate O2, C21, C22, C20, O3, Eu1	Hfa III	0.0095 (11)	C22

Interplanar angles (°)

	Bz	Py	Hfa I	Hfa II
Py	10.749 (31)			
Hfa I	80.818 (38)	71.551 (42)		
Hfa II	74.816 (38)	64.793 (41)	10.906 (36)	
Hfa III	102.047 (27)	106.904 (34)	90.154 (41)	100.249 (40)

Table S8 Selected bond distances (Å), bond angles (°) in [Lu(**L2**)(hfac)$_3$] (**5**).

Bond distances (Å)

Atom 1	Atom 2	Distance	Atom 1	Atom 2	Distance
Lu(1)	O(1)	2.2996(18)	Lu(1)	O(6)	2.3924(18)
Lu(1)	O(2)	2.3359(18)	Lu(1)	O(7)	2.3090(18)
Lu(1)	O(3)	2.2937(17)	Lu(1)	N(1)	2.505(2)
Lu(1)	O(4)	2.3661(17)	Lu(1)	N(3)	2.487(2)
Lu(1)	O(5)	2.3703(18)			

Angles (°)

At. 1	At. 2	At. 3	Angle	At. 1	At. 2	At. 3	Angle
O(6)	Lu(1)	N(1)	117.15(7)	O(2)	Lu(1)	O(6)	68.62(6)
O(6)	Lu(1)	N(3)	134.61(7)	O(2)	Lu(1)	N(1)	68.91(6)
O(7)	Lu(1)	O(2)	139.87(6)	O(2)	Lu(1)	N(3)	70.92(6)
O(7)	Lu(1)	O(4)	70.04(6)	O(3)	Lu(1)	O(1)	139.40(6)
O(7)	Lu(1)	O(5)	74.84(6)	O(3)	Lu(1)	O(2)	74.68(6)
O(7)	Lu(1)	O(6)	71.26(7)	O(3)	Lu(1)	O(4)	70.41(6)
O(7)	Lu(1)	N(1)	131.88(7)	O(3)	Lu(1)	O(5)	141.56(6)
O(7)	Lu(1)	N(3)	145.60(7)	O(3)	Lu(1)	O(6)	69.61(6)
N(3)	Lu(1)	N(1)	63.83(7)	O(3)	Lu(1)	O(7)	92.66(7)
O(1)	Lu(1)	O(2)	88.49(6)	O(3)	Lu(1)	N(1)	135.40(7)
O(1)	Lu(1)	O(3)	136.56(6)	O(3)	Lu(1)	N(3)	80.70(7)
O(1)	Lu(1)	O(5)	73.80(6)	O(4)	Lu(1)	O(5)	71.16(6)
O(1)	Lu(1)	O(6)	69.87(6)	O(4)	Lu(1)	O(6)	121.65(6)
O(1)	Lu(1)	O(7)	76.69(7)	O(4)	Lu(1)	N(1)	121.19(6)
O(1)	Lu(1)	N(1)	64.91(6)	O(4)	Lu(1)	N(3)	75.97(6)
O(1)	Lu(1)	N(3)	128.66(6)	O(5)	Lu(1)	O(6)	134.71(6)
O(2)	Lu(1)	O(4)	134.88(6)	O(5)	Lu(1)	N(1)	67.62(6)
O(2)	Lu(1)	O(5)	136.53(6)	O(5)	Lu(1)	N(3)	89.51(6)

Table S9 Selected least-squares planes data for [Lu(**L2**)(hfac)$_3$] (**5**).

Least-square planes

Least-squares planes description	Abbreviation	Max. deviation/Å	Atom
Benzimidazole C11 N3 C12 C13 C14 C15 C16 C17 N4	Bz	0.0155(10)	C17
Pyridine N1 C1 C2 C3 C4 C5	Py	0.0105(12)	N1
Hexafluoroacetylacetonate O3 C42 C41 C40 O8	Hfa I	0.0316(11)	C20
Hexafluoroacetylacetonate O4 C45 C46 C47 O5	Hfa II	0.0134(11)	C25
Hexafluoroacetylacetonate O6 C50 C51 C52 O7	Hfa III	0.0093(11)	C30

Interplanar angles (°)

	Bz	Py	Hfa I	Hfa II
Py	3.71(3)			
Hfa I	67.04(4)	64.96(4)		
Hfa II	68.44(4)	67.21(4)	14.20(3)	
Hfa III	75.98(3)	79.50(3)	80.64(4)	84.19(4)

Table S10 Selected bond distances (Å), bond angles (°) in $[Eu_2(\mathbf{L3})(hfac)_6]$ (**3**).

Bond distances (Å)

Atom 1	Atom 2	Distance	Atom 1	Atom 2	Distance
Eu(1)	O(1)	2.384(5)	Eu(2)	O(2)	2.389(6)
Eu(1)	O(3)	2.384(5)	Eu(2)	O(10)	2.392(5)
Eu(1)	O(4)	2.399(6)	Eu(2)	O(15)	2.393(6)
Eu(1)	O(7)	2.412(5)	Eu(2)	O(11)	2.406(5)
Eu(1)	O(9)	2.433(5)	Eu(2)	O(14)	2.453(5)
Eu(1)	O(5)	2.436(5)	Eu(2)	O(12)	2.461(5)
Eu(1)	O(8)	2.450(6)	Eu(2)	N(7)	2.579(6)
Eu(1)	N(3)	2.581(6)	Eu(2)	N(5)	2.622(6)
Eu(1)	N(1)	2.637(6)	Eu(1)	Eu(2)	12.594(1)
Eu(2)	O(13)	2.381(5)			

Angles (°)

At. 1	At. 2	At. 3	Angle	At. 1	At. 2	At. 3	Angle
O(1)	Eu(1)	O(3)	80.8(2)	O(7)	Eu(1)	O(8)	73.5(2)
O(1)	Eu(1)	O(4)	140.3(2)	O(9)	Eu(1)	O(8)	70.50(17)
O(3)	Eu(1)	O(4)	72.4(2)	O(5)	Eu(1)	O(8)	136.5(2)
O(1)	Eu(1)	O(7)	76.1(2)	O(1)	Eu(1)	N(3)	125.52(18)
O(3)	Eu(1)	O(7)	138.9(2)	O(3)	Eu(1)	N(3)	75.6(2)
O(4)	Eu(1)	O(7)	105.9(2)	O(4)	Eu(1)	N(3)	75.6(2)
O(1)	Eu(1)	O(9)	136.72(19)	O(7)	Eu(1)	N(3)	145.1(2)
O(3)	Eu(1)	O(9)	142.5(2)	O(9)	Eu(1)	N(3)	78.12(18)
O(4)	Eu(1)	O(9)	75.37(19)	O(5)	Eu(1)	N(3)	138.4(2)
O(7)	Eu(1)	O(9)	68.92(19)	O(8)	Eu(1)	N(3)	85.1(2)
O(1)	Eu(1)	O(5)	74.8(2)	O(1)	Eu(1)	N(1)	64.01(18)
O(3)	Eu(1)	O(5)	72.6(2)	O(3)	Eu(1)	N(1)	63.9(2)
O(4)	Eu(1)	O(5)	69.7(2)	O(4)	Eu(1)	N(1)	124.1(2)
O(7)	Eu(1)	O(5)	68.8(2)	O(7)	Eu(1)	N(1)	129.9(2)
O(9)	Eu(1)	O(5)	113.24(19)	O(9)	Eu(1)	N(1)	123.58(18)
O(1)	Eu(1)	O(8)	75.9(2)	O(5)	Eu(1)	N(1)	123.16(19)
O(3)	Eu(1)	O(8)	132.30(18)	O(8)	Eu(1)	N(1)	68.49(18)
O(4)	Eu(1)	O(8)	143.52(19)	N(3)	Eu(1)	N(1)	61.52(18)
O(13)	Eu(2)	O(2)	78.5(2)	O(15)	Eu(2)	O(12)	121.3(2)
O(13)	Eu(2)	O(10)	99.90(18)	O(11)	Eu(2)	O(12)	72.71(18)
O(2)	Eu(2)	O(10)	139.5(2)	O(14)	Eu(2)	O(12)	131.84(18)
O(13)	Eu(2)	O(15)	70.66(18)	O(13)	Eu(2)	N(7)	143.76(19)
O(2)	Eu(2)	O(15)	137.79(19)	O(2)	Eu(2)	N(7)	124.94(19)
O(10)	Eu(2)	O(15)	75.25(18)	O(10)	Eu(2)	N(7)	79.59(18)
O(13)	Eu(2)	O(11)	142.19(18)	O(15)	Eu(2)	N(7)	74.30(19)
O(2)	Eu(2)	O(11)	84.4(2)	O(11)	Eu(2)	N(7)	72.71(19)
O(10)	Eu(2)	O(11)	72.36(17)	O(14)	Eu(2)	N(7)	87.72(17)
O(15)	Eu(2)	O(11)	137.03(18)	O(12)	Eu(2)	N(7)	139.72(18)
O(13)	Eu(2)	O(14)	71.88(17)	O(13)	Eu(2)	N(5)	130.95(18)
O(2)	Eu(2)	O(14)	73.7(2)	O(2)	Eu(2)	N(5)	63.29(18)
O(10)	Eu(2)	O(14)	144.85(19)	O(10)	Eu(2)	N(5)	129.08(17)

O(15)	Eu(2)	O(14)	69.77(18)	O(15)	Eu(2)	N(5)	119.24(19)
O(11)	Eu(2)	O(14)	134.49(17)	O(11)	Eu(2)	N(5)	65.69(17)
O(13)	Eu(2)	O(12)	69.89(19)	O(14)	Eu(2)	N(5)	68.84(19)
O(2)	Eu(2)	O(12)	70.9(2)	O(12)	Eu(2)	N(5)	119.4(2)
O(10)	Eu(2)	O(12)	70.8(2)	N(7)	Eu(2)	N(5)	61.67(19)

Table S11 Selected least-squares planes data for $[Eu_2(\mathbf{L3})(hfac)_6]$ (**3**).

Least-Squares Planes

Least-squares planes description	Abbreviation	Max. deviation /Å	Atom
Benzimidazole 1 C11 N3 C12 C13 C14 C15 C16 C17 N4	Bz1	0.0421 (11)	C14
Pyridine 1 C1 C2 C3 C4 C5 N1	Py1	0.0160 (12)	C3
Benzimidazole 2 C21 C22 C23 N7 C24 N8 C25 C26 C27	Bz2	0.0489 (11)	C21
Pyridine 2 N5 C30 C31 C32 C33 C34	Py2	0.0135 (12)	C32
Hexafluoroacetylacetonate O3 C40 C41 C42 O4	Hfa I	0.0538 (11)	C42
Hexafluoroacetylacetonate O8 C51 C52 C53 O9	Hfa II	0.0225 (11)	C51
Hexafluoroacetylacetonate O5 C45 C46 C47 O7	Hfa III	0.0221 (12)	C46
Hexafluoroacetylacetonate O10 C56 C57 C58 O11	Hfa IV	0.0398 (11)	C58
Hexafluoroacetylacetonate O14 C66 C67 C68 O15	Hfa V	0.0315 (11)	C68
Hexafluoroacetylacetonate O12 C61 C62 C63 O13	Hfa VI	0.0232 (11)	C61

Interplanar angles (°)

	Bz1	Py1	Bz2	Py2	Hfa I	Hfa II	Hfa III	Hfa IV	Hfa V
Bz1									
Py1	18.47(3)								
Bz2	54.25(2)	69.53(3)							
Py2	57.71(3)	74.12(4)	7.30(3)						
Hfa I	74.52(4)	58.74(4)	98.75(3)	106.05(4)					
Hfa II	78.95(4)	62.84(4)	102.84(4)	110.13(4)	4.70(5)				
Hfa III	75.89(3)	71.81(4)	118.85(3)	116.59(4)	99.48(4)	99.29(4)			
Hfa IV	89.89(3)	73.66(4)	109.72(4)	116.88(4)	15.44(4)	10.95(4)	102.37(4)		
Hfa V	82.97(4)	65.32(4)	113.85(4)	121.14(4)	15.29(4)	11.95(4)	89.48(4)	13.44(3)	
Hfa VI	61.03(3)	55.14(4)	109.82(3)	109.58(3)	87.33(4)	88.14(4)	16.86(4)	93.61(4)	80.18(4)

Table S12 Selected bond distances (Å), bond angles (°) in $[Lu_2(\mathbf{L3})(hfac)_6]$ (6).

Bond distances (Å)

Atom 1	Atom 2	Distance	Atom 1	Atom 2	Distance
Lu(1)	O(8)	2.266(4)	Lu(1)	O(7)	2.381(4)
Lu(1)	O(1)	2.284(4)	Lu(1)	O(3)	2.394(4)
Lu(1)	O(5)	2.326(4)	Lu(1)	N(1)	2.474(5)
Lu(1)	O(6)	2.354(4)	Lu(1)	N(3)	2.479(5)
Lu(1)	O(4)	2.375(5)	Lu(1)	Lu(2)	12.533 (1)
Lu(2)	O(10)	2.279(4)	Lu(2)	O(14)	2.388(4)
Lu(2)	O(2)	2.296(4)	Lu(2)	O(13)	2.395(4)
Lu(2)	O(11)	2.339(4)	Lu(2)	N(5)	2.496(5)
Lu(2)	O(12)	2.360(5)	Lu(2)	N(7)	2.507(5)
Lu(2)	O(9)	2.379(4)			

Angles (°)

At. 1	At. 2	At. 3	Angle	At. 1	At. 2	At. 3	Angle
O(8)	Lu(1)	O(1)	139.66(17)	O(6)	Lu(1)	O(3)	134.53(15)
O(8)	Lu(1)	O(5)	100.86(17)	O(4)	Lu(1)	O(3)	69.23(16)
O(1)	Lu(1)	O(5)	76.42(17)	O(7)	Lu(1)	O(3)	138.70 (16)
O(8)	Lu(1)	O(6)	140.86(16)	O(8)	Lu(1)	N(1)	128.34(17)
O(1)	Lu(1)	O(6)	77.73(15)	O(1)	Lu(1)	N(1)	65.27(17)
O(5)	Lu(1)	O(6)	72.92(15)	O(5)	Lu(1)	N(1)	130.76(16)
O(8)	Lu(1)	O(4)	70.02(17)	O(6)	Lu(1)	N(1)	69.76(14)
O(1)	Lu(1)	O(4)	70.77(16)	O(4)	Lu(1)	N(1)	117.89(17)
O(5)	Lu(1)	O(4)	73.30(16)	O(7)	Lu(1)	N(1)	123.82(16)
O(6)	Lu(1)	O(4)	138.06(16)	O(3)	Lu(1)	N(1)	64.77(15)
O(8)	Lu(1)	O(7)	72.25(16)	O(8)	Lu(1)	N(3)	76.25(17)
O(1)	Lu(1)	O(7)	137.18(15)	O(1)	Lu(1)	N(3)	129.64(16)
O(5)	Lu(1)	O(7)	68.12(16)	O(5)	Lu(1)	N(3)	142.45(16)
O(6)	Lu(1)	O(7)	69.65(13)	O(6)	Lu(1)	N(3)	85.94(15)
O(4)	Lu(1)	O(7)	118.28(16)	O(4)	Lu(1)	N(3)	135.67(16)
O(8)	Lu(1)	O(3)	73.60(17)	O(7)	Lu(1)	N(3)	75.60(15)
O(1)	Lu(1)	O(3)	84.44(17)	O(3)	Lu(1)	N(3)	74.31(16)
O(5)	Lu(1)	O(3)	141.71(17)	N(1)	Lu(1)	N(3)	64.38(16)
O(10)	Lu(2)	O(2)	141.33(16)	O(12)	Lu(2)	O(13)	119.47(16)
O(10)	Lu(2)	O(11)	100.34(15)	O(9)	Lu(2)	O(13)	139.68(15)
O(2)	Lu(2)	O(11)	75.26(16)	O(14)	Lu(2)	O(13)	69.17(14)
O(10)	Lu(2)	O(12)	70.32(16)	O(10)	Lu(2)	N(5)	128.13(15)
O(2)	Lu(2)	O(12)	71.73(17)	O(2)	Lu(2)	N(5)	65.02(16)
O(11)	Lu(2)	O(12)	73.12(16)	O(11)	Lu(2)	N(5)	131.41(15)
O(10)	Lu(2)	O(9)	73.81(15)	O(12)	Lu(2)	N(5)	116.30(16)
O(2)	Lu(2)	O(9)	85.19(16)	O(9)	Lu(2)	N(5)	64.52(15)
O(11)	Lu(2)	O(9)	139.86(16)	O(14)	Lu(2)	N(5)	70.67(14)
O(12)	Lu(2)	O(9)	67.50(16)	N(13)	Lu(2)	N(5)	124.23(15)
O(10)	Lu(2)	O(14)	140.84(14)	O(10)	Lu(2)	N(7)	76.63(15)
O(2)	Lu(2)	O(14)	75.78(16)	O(2)	Lu(2)	N(7)	129.02(15)

O(11)	Lu(2)	O(14)	73.45(15)	O(11)	Lu(2)	N(7)	143.79(15)
O(12)	Lu(2)	O(14)	138.02(16)	O(12)	Lu(2)	N(7)	135.12(16)
O(9)	Lu(2)	O(14)	135.20(14)	O(9)	Lu(2)	N(7)	74.80(16)
O(10)	Lu(2)	O(13)	72.61(15)	O(14)	Lu(2)	N(7)	86.32(16)
O(2)	Lu(2)	O(13)	135.10(16)	O(13)	Lu(2)	N(7)	76.29(15)
O(11)	Lu(2)	O(13)	68.59(15)	N(5)	Lu(2)	N(7)	64.03(15)

Table S13 Selected least-squares planes data for for $[Lu_2(\mathbf{L3})(hfac)_6]$ (**6**).

Least-Squares Planes

Least-squares planes description	Abbreviation	Max. deviation /Å	Atom
Benzimidazole 1 C11 N3 C12 C13 C14 C15 C16 C17 N4	Bz1	0.0511 (10)	C12
Pyridine 1 C1 C2 C3 C4 C5 N1	Py1	0.0110 (12)	N1
Benzimidazole 2 C21 C22 C23 N7 C24 N8 C25 C26 C27	Bz2	0.0435 (11)	C21
Pyridine 2 C30 C31 C32 C33 C34 N5	Py2	0.0097 (12)	C34
Hexafluoroacetylacetonate O3 C42 C41 C40 O8	Hfa I	0.0275 (11)	C40
Hexafluoroacetylacetonate O6 C50 C51 C52 O7	Hfa II	0.0190 (11)	C50
Hexafluoroacetylacetonate O4 C45 C46 C47 O5	Hfa III	0.0071 (12)	C46
Hexafluoroacetylacetonate O9 C55 C56 C57 O10	Hfa IV	0.0189 (11)	C57
Hexafluoroacetylacetonate O13 C65 C66 C67 O14	Hfa V	0.0212 (11)	C67
Hexafluoroacetylacetonate O11 C62 C61 C60 O12	Hfa VI	0.0084 (12)	C61

Interplanar angles (°)

	Bz1	Py1	Bz2	Py2	Hfa I	Hfa II	Hfa III	Hfa IV	Hfa V
Py1	4.76(3)								
Bz2	60.67(3)	59.10(3)							
Py2	72.86(3)	71.94(3)	14.52(3)						
Hfa I	118.43(4)	122.18(4)	90.68(3)	77.28(3)					
Hfa II	107.77(4)	111.14(4)	79.37(4)	66.63(4)	12.42(5)				
Hfa III	101.85(3)	97.54(3)	59.06(3)	59.44(4)	107.14(4)	105.02(4)			
Hfa IV	103.57(3)	106.69(4)	73.56(4)	60.99(4)	18.16(4)	5.89(5)	102.27(5)		
Hfa V	109.96(4)	113.02(4)	76.83(4)	63.55(4)	13.86(4)	5.31(3)	99.75(4)	6.44(4)	
Hfa VI	115.16(3)	110.80(4)	69.80(3)	67.52(4)	100.33(4)	100.91(4)	13.40(3)	99.43(4)	95.63(4)

Table S14 Selected bond distances (Å), bond angles (°) in $[Eu_3(\mathbf{L4})(hfac)_9]$ (**4**).

Bond distances (Å)

Atom 1	Atom 2	Distance	Atom 1	Atom 2	Distance
Eu(1)	O(5H)	2.372(4)	Eu(2)	O(11H)	2.469(4)
Eu(1)	O(6H)	2.402(4)	Eu(2)	N(4)	2.567(4)
Eu(1)	O(3H)	2.402(4)	Eu(2)	N(6)	2.593(4)
Eu(1)	O(1H)	2.410(4)	Eu(3)	O(13H)	2.399(4)
Eu(1)	O(2H)	2.471(4)	Eu(3)	O(15H)	2.409(4)
Eu(1)	O(4H)	2.482(4)	Eu(3)	O(2)	2.422(4)
Eu(1)	N(2)	2.525(4)	Eu(3)	O(16H)	2.425(4)
Eu(1)	N(8)	2.547(4)	Eu(3)	O(14H)	2.425(4)
Eu(1)	N(1)	2.643(4)	Eu(3)	O(18H)	2.435(4)
Eu(2)	O(7H)	2.387(4)	Eu(3)	O(17H)	2.435(4)
Eu(2)	O(10H)	2.396(4)	Eu(3)	N(10)	2.598(4)
Eu(2)	O(12H)	2.409(4)	Eu(3)	N(12)	2.611(5)
Eu(2)	O(1)	2.412(4)	Eu(3)	Eu(1)	12.806(1)
Eu(2)	O(9H)	2.434(4)	Eu(1)	Eu(2)	9.593(1)
Eu(2)	O(8H)	2.446(3)	Eu(2)	Eu(3)	19.051(1)

Angles (°)

At. 1	At. 2	At. 3	Angle	At. 1	At. 2	At. 3	Angle
O(5H)	Eu(1)	O(6H)	75.31(15)	O(1)	Eu(2)	O(11H)	73.81(14)
O(5H)	Eu(1)	O(3H)	81.65(15)	O(9H)	Eu(2)	O(11H)	132.18(13)
O(6H)	Eu(1)	O(3H)	135.71(15)	O(8H)	Eu(2)	O(11H)	136.49(13)
O(5H)	Eu(1)	O(1H)	139.94(15)	O(7H)	Eu(2)	N(4)	80.73(13)
O(6H)	Eu(1)	O(1H)	80.39(14)	O(10H)	Eu(2)	N(4)	143.49(13)
O(3H)	Eu(1)	O(1H)	136.22(13)	O(12H)	Eu(2)	N(4)	76.12(13)
O(5H)	Eu(1)	O(2H)	72.50(14)	O(1)	Eu(2)	N(4)	125.18(13)
O(6H)	Eu(1)	O(2H)	67.21(14)	O(9H)	Eu(2)	N(4)	141.15(13)
O(3H)	Eu(1)	O(2H)	139.06(13)	O(8H)	Eu(2)	N(4)	76.63(12)
O(1H)	Eu(1)	O(2H)	68.86(12)	O(11H)	Eu(2)	N(4)	85.96(13)
O(5H)	Eu(1)	O(4H)	71.38(14)	O(7H)	Eu(2)	N(6)	130.40(13)
O(6H)	Eu(1)	O(4H)	67.92(15)	O(10H)	Eu(2)	N(6)	129.02(15)
O(3H)	Eu(1)	O(4H)	69.05(14)	O(12H)	Eu(2)	N(6)	121.27(13)
O(1H)	Eu(1)	O(4H)	126.93(14)	O(1H)	Eu(2)	N(6)	63.38(12)
O(2H)	Eu(1)	O(4H)	127.70(13)	O(9H)	Eu(2)	N(6)	119.53(13)
O(5H)	Eu(1)	N(2)	82.67(14)	O(8H)	Eu(2)	N(6)	68.61(12)
O(6H)	Eu(1)	N(2)	139.08(14)	O(11H)	Eu(2)	N(6)	68.01(13)
O(3H)	Eu(1)	N(2)	72.14(14)	N(4)	Eu(2)	N(6)	61.81(13)
O(1H)	Eu(1)	N(2)	96.04(14)	O(13H)	Eu(3)	O(15H)	72.05(13)
O(2H)	Eu(1)	N(2)	73.49(13)	O(13H)	Eu(3)	O(2)	140.61(14)
O(4H)	Eu(1)	N(2)	135.67(14)	O(15H)	Eu(3)	O(2)	139.76(13)
O(5H)	Eu(1)	N(8)	141.41(14)	O(13H)	Eu(3)	O(16H)	137.39(13)
O(6H)	Eu(1)	N(8)	89.66(13)	O(15H)	Eu(3)	O(16H)	71.76(13)
O(3H)	Eu(1)	N(8)	85.35(14)	O(2)	Eu(3)	O(16H)	81.96(13)
O(1H)	Eu(1)	N(8)	68.33(13)	O(13H)	Eu(3)	O(14H)	71.09(14)
O(2H)	Eu(1)	N(8)	133.95(13)	O(15H)	Eu(3)	O(14H)	141.85(14)
O(4H)	Eu(1)	N(8)	70.03(13)	O(2)	Eu(3)	O(14H)	77.74(14)
N(2)	Eu(1)	N(8)	127.14(13)	O(16H)	Eu(3)	O(14H)	134.95(14)
O(5H)	Eu(1)	N(1)	138.18(14)	O(13H)	Eu(3)	O(18H)	112.49(15)
O(6H)	Eu(1)	N(1)	146.51(13)	O(15H)	Eu(3)	O(18H)	69.69(13)
O(3H)	Eu(1)	N(1)	65.56(13)	O(2)	Eu(3)	O(18H)	74.25(13)
O(1H)	Eu(1)	N(1)	71.42(12)	O(16H)	Eu(3)	O(18H)	74.38(14)

O(2H)	Eu(1)	N(1)	116.32(13)	O(14H)	Eu(3)	O(18H)	135.08(14)
O(4H)	Eu(1)	N(1)	115.88(13)	O(13H)	Eu(3)	O(17H)	69.25(16)
N(2)	Eu(1)	N(1)	63.57(13)	O(15H)	Eu(3)	O(17H)	104.08(15)
N(8)	Eu(1)	N(1)	63.58(13)	O(2)	Eu(3)	O(17H)	78.48(15)
O(7H)	Eu(2)	O(10H)	100.52(15)	O(16H)	Eu(3)	O(17H)	142.00(14)
O(7H)	Eu(2)	O(12H)	74.27(14)	O(14H)	Eu(3)	O(17H)	71.40(15)
O(10H)	Eu(2)	O(12H)	69.36(14)	O(18H)	Eu(3)	O(17H)	69.11(15)
O(7H)	Eu(2)	O(1)	140.02(13)	O(13H)	Eu(3)	N(10)	75.92(15)
O(10H)	Eu(2)	O(1)	76.52(14)	O(15H)	Eu(3)	N(10)	75.90(13)
O(12H)	Eu(2)	O(1)	136.27(14)	O(2)	Eu(3)	N(10)	125.77(14)
O(7H)	Eu(2)	O(9H)	71.04(14)	O(16H)	Eu(3)	N(10)	74.11(14)
O(10H)	Eu(2)	O(9H)	69.73(14)	O(14H)	Eu(3)	N(10)	85.97(14)
O(12H)	Eu(2)	O(9H)	118.99(14)	O(18H)	Eu(3)	N(10)	138.95(13)
O(1)	Eu(2)	O(9H)	70.67(13)	O(17H)	Eu(3)	N(10)	142.97(15)
O(7H)	Eu(2)	O(8H)	72.14(13)	O(13H)	Eu(3)	N(12)	121.06(15)
O(10H)	Eu(2)	O(8H)	138.93(13)	O(15H)	Eu(3)	N(12)	127.44(14)
O(12H)	Eu(2)	O(8H)	139.44(14)	O(2)	Eu(3)	N(12)	64.20(13)
O(1)	Eu(2)	O(8H)	84.22(13)	O(16H)	Eu(3)	N(12)	67.91(13)
O(9H)	Eu(2)	O(8H)	69.74(13)	O(14H)	Eu(3)	N(12)	67.06(14)
O(7H)	Eu(2)	O(11H)	144.02(14)	O(18H)	Eu(3)	N(12)	126.43(14)
O(10H)	Eu(2)	O(11H)	71.66(14)	O(17H)	Eu(3)	N(12)	128.45(15)
O(12H)	Eu(2)	O(11H)	70.11(15)	O(10)	Eu(3)	N(12)	61.79(14)

Table S15 Selected least-squares planes data for $[Eu_3(\mathbf{L4})(hfac)_9]$ (**4**).

Least-Squares Planes

Least-squares planes description	Abbreviation	Max. deviation /Å	Atom
Benzimidazole 1 C6 N2 C7 C8 C9 C10 C11 C12 N3	Bz1	0.0283 (11)	C6
Pyridine 1 C1 C2 C3 C4 C5 N1	Py1	0.0079 (12)	C5
Benzimidazole 2 C31 N8 C32 C33 C34 C35 C36 C37 N9	Bz2	0.0137 (11)	C31
Pyridine 2 C21 C22 C23 C24 C25 N6	Py2	0.0262 (12)	N6
Benzimidazole 3 N4 C16 C15 C14 C19 C18 C17 N5	Bz3	0.0279 (12)	N4
Benzimidazole 4 C39 C40 C41 N10 C45 N11 C42 C43 C44	Bz4	0.0124 (11)	N10
Pyridine 3 N12 C46 C47 C48 C49 C50	Py3	0.0403 (12)	N12
Hexafluoroacetylacetonate O1H C1H C2H C3H O2H	Hfa I	0.0341 (11)	C1H
Hexafluoroacetylacetonate O3H C6H C7H C8H O4H	Hfa II	0.0203 (11)	C8H
Hexafluoroacetylacetonate O5H C11H C12H C13H O6H	Hfa III	0.0004 (11)	C11H
Hexafluoroacetylacetonate O7H C16H C17H C18H O8H	Hfa IV	0.0118 (11)	C18H
Hexafluoroacetylacetonate O11H C26H C27H C28H O12H	Hfa V	0.0006 (11)	C28H
Hexafluoroacetylacetonate O9H C21H C22H C23H O10H	Hfa VI	0.0258 (11)	C21H
Hexafluoroacetylacetonate O16H C36H C37H C38H O15H	Hfa VII	0.0385 (11)	C38H
Hexafluoroacetylacetonate O13H C31H C32H C33H O14H	Hfa VIII	0.0210 (11)	C33H
Hexafluoroacetylacetonate O17H C41H C42H C43H O18H	Hfa IX	0.0097 (11)	C43H

Interplanar angles (°)

	Bz1	Py1	Bz2	Py2	Bz3	Py3	Bz4
Py1	24.33 (3)						
Bz2	155.14 (2)	147.28 (3)					
Py2	72.72 (3)	62.68 (3)	86.24 (3)				
Bz3	82.51 (2)	77.73 (3)	73.86 (2)	17.87 (3)			
Py3	58.89 (3)	37.35 (3)	110.80 (3)	37.24 (3)	55.10 (3)		
Bz4	82.34 (3)	61.12 (3)	87.66 (3)	34.26 (3)	48.61 (2)	23.81 (3)	
Hfa I	100.66 (4)	119.92 (4)	64.25 (4)	86.82 (3)	69.99 (3)	122.30 (3)	117.81 (3)
Hfa II	66.36 (4)	55.10 (4)	93.46 (4)	7.70 (4)	25.04 (4)	30.59 (4)	32.14 (3)
Hfa III	136.09 (3)	136.81 (4)	19.80 (3)	74.47 (4)	59.12 (3)	106.53 (4)	86.69 (4)
Hfa IV	124.17 (3)	146.73 (3)	49.93 (3)	108.28 (4)	90.42 (4)	145.48 (4)	130.48 (4)
Hfa V	62.09 (3)	37.85 (4)	118.86 (3)	60.78 (4)	78.47 (4)	23.97 (4)	36.24 (3)
Hfa VI	142.84 (3)	121.09 (4)	32.73 (4)	74.43 (3)	71.00 (3)	84.34 (4)	60.64 (4)
Hfa VII	19.26 (3)	28.40 (4)	136.18 (3)	54.86 (4)	63.34 (3)	50.59 (4)	71.50 (4)
Hfa VIII	18.35 (3)	42.16 (4)	144.15 (3)	77.01 (4)	81.52 (4)	73.36 (4)	95.33 (4)
Hfa IX	89.11 (4)	103.25 (4)	69.83 (4)	65.73 (3)	49.75 (3)	100.62 (3)	98.34 (3)

	Hfa I	Hfa II	Hfa III	Hfa IV	Hfa V	Hfa VI	Hfa VII	Hfa VIII
Hfa II	92.34 (3)							
Hfa III	49.10 (4)	82.15 (4)						
Hfa IV	28.42 (4)	115.20 (4)	44.45 (5)					
Hfa V	146.04 (4)	54.47 (4)	122.39 (4)	166.70 (4)				
Hfa VI	94.36 (5)	79.33 (4)	45.40 (4)	82.58 (4)	86.85 (4)			
Hfa VII	91.53 (4)	49.29 (4)	118.10 (3)	118.97 (4)	62.45 (4)	128.49 (4)		
Hfa VIII	83.16 (4)	72.37 (5)	124.53 (3)	105.82 (3)	80.10 (4)	151.43 (4)	24.07 (5)	
Hfa IX	21.67 (3)	70.86 (3)	50.64 (4)	48.60 (4)	124.40 (4)	92.93 (4)	75.51 (4)	74.40 (4)

Table S16 Bond Distances ($\delta_{i,j}$), Bond Valences ($v_{\mathrm{Ln,j}}$)[a] and Total Atom Valence (V_{Ln})[b] in the Crystal Structure of [Eu(**L2**)(hfac)$_3$] (**2**).

Atom[c]	Donor type	$\delta_{\mathrm{Eu},j}$ / Å	$v_{\mathrm{Eu},j}$	
N3	bzim	2.566	0.335	Average N-heterocyclic
N1	py	2.612	0.296	0.32 (3)
O1	amide	2.396	0.380	
O2	hfac	2.450	0.328	
O3	hfac	2.417	0.359	
O4	hfac	2.394	0.382	
O5	hfac	2.397	0.379	
O6	hfac	2.421	0.355	Average O-hfac
O7	hfac	2.445	0.333	0.36 (2)
		V_{Eu}	3.147	

[a] $v_{\mathrm{Ln},j} = e^{\left[\left(R_{\mathrm{Ln},j} - d_{\mathrm{Ln},j}\right)/b\right]}$, whereby $\delta_{\mathrm{Ln},j}$ is the Ln-donor atom j distance. The valence bond parameters $R_{\mathrm{Ln,N}}$ and $R_{\mathrm{Ln,O}}$ are taken from ref 29e,f and b = 0.37 Å. [b] $V_{\mathrm{Ln}} = \sum_j v_{\mathrm{Ln},j}$. [c] Numbering taken from Fig S1a.

Table S17 Bond Distances ($\delta_{i,j}$), Bond Valences ($v_{\mathrm{Ln,j}}$)[a] and Total Atom Valence (V_{Ln})[b] in the Crystal Structure of [Lu(**L2**)(hfac)$_3$] (**5**).

Atom[c]	Donor type	$\delta_{\mathrm{Lu},j}$ / Å	$v_{\mathrm{Lu},j}$	
N3	bzim	2.487	0.304	Average N-heterocyclic
N1	py	2.505	0.289	0.30 (1)
O1	amide	2.300	0.386	
O2	hfac	2.336	0.350	
O3	hfac	2.294	0.392	
O4	hfac	2.366	0.322	
O5	hfac	2.370	0.319	
O6	hfac	2.392	0.300	Average O-hfac
O7	hfac	2.309	0.376	0.34 (4)
		V_{Lu}	3.036	

[a] $v_{\mathrm{Ln},j} = e^{\left[\left(R_{\mathrm{Ln},j} - d_{\mathrm{Ln},j}\right)/b\right]}$, whereby $\delta_{\mathrm{Ln},j}$ is the Ln-donor atom j distance. The valence bond parameters $R_{\mathrm{Ln,N}}$ and $R_{\mathrm{Ln,O}}$ are taken from ref 29e,f and b = 0.37 Å. [b] $V_{\mathrm{Ln}} = \sum_j v_{\mathrm{Ln},j}$. [c] Numbering taken from Fig S1b.

Table S18 Bond Distances ($\delta_{i,j}$), Bond Valences ($v_{\mathrm{Ln,j}}$)[a] and Total Atom Valence (V_{Ln})[b] in the Crystal Structure of [Eu_2(**L3**)(hfac)$_6$] (**3**).

Atom[c]	Donor type	$\delta_{\mathrm{Eu},j}$ / Å	$v_{\mathrm{Eu},j}$	
N3	bzim	2.581	0.321	Average N-heterocyclic
N1	py	2.637	0.276	0.30 (3)
O1	amide	2.384	0.393	
O3	hfac	2.384	0.393	
O4	hfac	2.399	0.377	
O8	hfac	2.450	0.328	
O9	hfac	2.433	0.344	
O5	hfac	2.436	0.341	Average O-hfac
O7	hfa	2.412	0.364	0.36 (2)
		V_{Eu1}	3.137	
N7	bzim	2.579	0.323	Average N-heterocyclic
N5	py	2.622	0.288	0.31 (3)
O2	amide	2.389	0.387	
O10	hfac	2.392	0.384	
O11	hfac	2.406	0.370	
O14	hfac	2.453	0.326	
O15	hfac	2.393	0.383	
O12	hfac	2.461	0.319	Average O-hfac
O13	hfac	2.381	0.396	0.36 (3)
		V_{Eu2}	3.175	

[a] $v_{\mathrm{Ln},j} = e^{\left[\left(R_{\mathrm{Ln},j} - d_{\mathrm{Ln},j}\right)/b\right]}$, whereby $\delta_{\mathrm{Ln},j}$ is the Ln-donor atom j distance. The valence bond parameters $R_{\mathrm{Ln,N}}$ and $R_{\mathrm{Ln,O}}$ are taken from ref 29e,f and b = 0.37 Å. [b] $V_{\mathrm{Ln}} = \sum_j v_{\mathrm{Ln},j}$. [c] Numbering taken from Fig S2a.

Table S19 Bond Distances ($\delta_{i,j}$), Bond Valences ($v_{\mathrm{Ln,j}}$)[a] and Total Atom Valence (V_{Ln})[b] in the Crystal Structure of [Lu_2(**L3**)(hfac)$_6$] (**6**).

Atom[c]	Donor type	$\delta_{\mathrm{Lu},j}$ / Å	$v_{\mathrm{Lu},j}$	
N3	bzim	2.479	0.310	Average N-heterocyclic
N1	py	2.474	0.315	0.312 (3)
O1	amide	2.284	0.402	
O3	hfac	2.394	0.299	
O8	hfac	2.266	0.422	
O4	hfac	2.375	0.315	
O5	hfac	2.326	0.359	
O6	hfac	2.354	0.333	Average O-hfac
O7	hfac	2.381	0.309	0.34 (5)
		V_{Lu1}	3.064	
N7	bzim	2.507	0.288	Average N-heterocyclic
N5	py	2.496	0.296	0.29 (1)
O2	amide	2.296	0.389	
O11	hfac	2.339	0.347	
O12	hfac	2.360	0.328	
O9	hfac	2.379	0.311	
O10	hfac	2.279	0.408	
O13	hfac	2.395	0.298	Average O-hfac
O14	hfac	2.388	0.304	0.33 (4)
		V_{Lu2}	2.968	

[a] $v_{\mathrm{Ln},j} = e^{\left[\left(R_{\mathrm{Ln},j} - d_{\mathrm{Ln},j}\right)/b\right]}$, whereby $\delta_{\mathrm{Ln},j}$ is the Ln-donor atom j distance. The valence bond parameters $R_{\mathrm{Ln,N}}$ and $R_{\mathrm{Ln,O}}$ are taken from ref 29e,f and b = 0.37 Å. [b] $V_{\mathrm{Ln}} = \sum_j v_{\mathrm{Ln},j}$. [c] Numbering taken from Fig S2b.

Table S20 Bond Distances ($\delta_{i,j}$), Bond Valences ($v_{\mathrm{Ln,j}}$)[a] and Total Atom Valence (V_{Ln})[b] in the Crystal Structure of [Eu_3(**L4**)(hfac)$_9$] (**4**).

Atom[c]	Donor type	$\delta_{\mathrm{Eu},j}$ / Å	$v_{\mathrm{Eu},j}$	
N2	bzim	2.525	0.374	
N1	py	2.643	0.272	Average N-heterocyclic
N8	bzim	2.547	0.352	0.33 (5)
O1H	hfac	2410	0.366	
O2H	hfac	2.471	0.310	
O3H	hfac	2.402	0.374	
O4H	hfac	2.482	0.301	
O5H	hfac	2.372	0.405	Average O-hfac
O6H	hfac	2.402	0.374	0.36 (4)
		V_{Eu1}	3.129	
N4	bzim	2.567	0.334	Average N-heterocyclic
N6	py	2.593	0.311	0.32 (2)
O1	amide	2.412	0.364	
O7H	hfac	2.387	0.389	
O8H	hfac	2.446	0.332	
O9H	hfac	2.434	0.343	
O10H	hfac	2.396	0.380	
O11H	hfac	2.469	0.312	Average O-hfac
O12H	hfac	2.409	0.367	0.35 (3)
		V_{Eu2}	3.132	
N10	bzim	2.598	0.307	Average N-heterocyclic
N12	py	2.611	0.296	0.30 (1)
O2	amide	2.422	0.354	
O13H	hfac	2.399	0.377	
O14H	hfac	2.425	0.351	
O15H	hfac	2.409	0.367	
O16H	hfac	2.425	0.351	
O17H	hfac	2.435	0.342	Average O-hfac
O18H	hfac	2.435	0.342	0.36 (1)
		V_{Eu3}	3.088	

[a] $v_{\mathrm{Ln},j} = e^{\left[\left(R_{\mathrm{Ln},j} - d_{\mathrm{Ln},j}\right)/b\right]}$, whereby $\delta_{\mathrm{Ln},j}$ is the Ln-donor atom j distance. The valence bond parameters $R_{\mathrm{Ln,N}}$ and $R_{\mathrm{Ln,O}}$ are taken from ref 29e,f and b = 0.37 Å. [b] $V_{\mathrm{Ln}} = \sum_j v_{\mathrm{Ln},j}$. [c] Numbering taken from Fig S3.

Table S21 Helicity indexes *H* of the five-atoms crooked line in the molecular structures of $[Eu_2(\mathbf{L3})(hfac)_6]$ (**3**), $[Lu_2(\mathbf{L3})(hfac)_6]$ (**6**) and $[Eu_3(\mathbf{L4})(hfac)_9]$ (**4**) whree *L* is the end to end distance of the helix, *A* is the area of the subtended figure in the projection plane and *D* is the total length of the crooked line.[30]

Compound	*L* /Å	*A* /Å^2	*D* /Å	*H*
$[Eu_2(\mathbf{L3})(hfac)_6]$	4.32	0.747	5.87	0.52
$[Lu_2(\mathbf{L3})(hfac)_6]$	4.06	0.842	5.78	0.58
$[Eu_3(\mathbf{L4})(hfac)_9]$	3.64	1.290	5.86	0.71
	4.32	1.195	5.87	0.83

Table S22 Summary of crystal data, intensity measurements and structure refinements for $[La(\mathbf{L2})_2(hfac)_2]_2[La_2(hfac)_4(O_2CCF_3)_4]\cdot 2CH_3CN$ (**7**).

	7
Empirical formula	$C_{48}H_{46}F_{12}N_8O_6La$, $0.5(C_{28}H_4F_{36}La_2O_{16})$, $2CH_3CN$
Formula weight	2059.01
Temperature	190 (2) K
Wavelength	1.54184 Å
Crystal System, Space group	triclinic, *P*-1
Unit cell dimensions	a = 11.6721 (2) Å
	b = 15.7298 (4) Å
	c = 22.3967 (5) Å
	α = 78.307 (2)°
	β = 87.1599 (10)°
	γ = 89.3088 (18)°
Volume in Å^3	4018.90 (16)
Z, Calculated density	2, 1.701 Mg/m^3
Absorption coefficient	9.331 mm^{-1}
F(000)	2032
Theta range for data collection	2.87 to 73.48°
Limiting indices	-14<=h<=11,
	-18<=k<=19,
	-27<=l<=27
Reflections collected / unique	28390 / 15744
	[R(int) = 0.05]
Completeness to theta	66.97°/ 99.9 %
Data / restraints / parameters	15744 / 3 / 1091
Goodness-of-fit on F^2	1.051
Final R indices [I>2σ(I)]	R_1 = 0.0522,
	ωR_2 = 0.1400
R indices (all data)	R_1 = 0.0554,
	ωR_2 = 0.1449
Largest diff. peak and hole	1.541 and -1.428 e.Å^{-3}

Table S23 Selected bond distances (Å), bond angles (°) in $[La(\mathbf{L2})_2(hfac)_2]_2[La_2(hfac)_4(O_2CCF_3)_4]$ (**7**).

Bond distances (Å)			Bond distances (Å)		
Atom 1	Atom 2	Distance	Atom 1	Atom 2	Distance
La(1)	N(1A)	2.769(3)	La(1)	O(4H)	2.537(3)
La(1)	N(1B)	2.788(3)	La(2)	O(1C)	2.494(3)
La(1)	N(3A)	2.728(3)	La(2)	O(2C)	2.497(3)
La(1)	N(3B)	2.757(3)	La(2)	O(3C)	2.493(3)
La(1)	O(1A)	2.549(3)	La(2)	O(4C)	2.507(3)
La(1)	O(1B)	2.507(3)	La(2)	O(5C)	2.495(3)
La(1)	O(1H)	2.543(3)	La(2)	O(6C)	2.510(3)
La(1)	O(2H)	2.550(3)	La(2)	O(7C)	2.460(3)
La(1)	O(3H)	2.571(3)	La(2)	O(8C)	2.543(3)

Angles				Angles			
At. 1	At. 2	At. 3	Angle	At. 1	At. 2	At. 3	Angle
O(1B)	La(1)	O(4H)	136.14(10)	O(4H)	La(1)	N(1B)	115.43(10)
O(1B)	La(1)	O(1H)	68.72(11)	O(1H)	La(1)	N(1B)	114.09(10)
O(4H)	La(1)	O(1H)	130.26(10)	O(1A)	La(1)	N(1B)	123.87(10)
O(1B)	La(1)	O(1A)	72.71(10)	O(2H)	La(1)	N(1B)	64.46(10)
O(4H)	La(1)	O(1A)	78.26(9)	O(3H)	La(1)	N(1B)	69.37(10)
O(1H)	La(1)	O(1A)	70.89(10)	N(3A)	La(1)	N(1B)	117.46(10)
O(1B)	La(1)	O(2H)	78.78(10)	N(3B)	La(1)	N(1B)	58.08(10)
O(4H)	La(1)	O(2H)	142.50(9)	N(1A)	La(1)	N(1B)	175.80(10)
O(1H)	La(1)	O(2H)	67.01(10)	O(7C)	La(2)	O(3C)	145.76(12)
O(1A)	La(1)	O(2H)	135.36(10)	O(7C)	La(2)	O(1C)	139.34(12)
O(1B)	La(1)	O(3H)	72.09(11)	O(3C)	La(2)	O(1C)	72.58(12)
O(4H)	La(1)	O(3H)	66.84(10)	O(7C)	La(2)	O(5C)	73.29(12)
O(1H)	La(1)	O(3H)	129.60(10)	O(3C)	La(2)	O(5C)	78.70(12)
O(1A)	La(1)	O(3H)	68.08(10)	O(1C)	La(2)	O(5C)	146.41(11)
O(2H)	La(1)	O(3H)	133.16(10)	O(7C)	La(2)	O(2C)	79.48(12)
O(1B)	La(1)	N(3A)	146.98(10)	O(3C)	La(2)	O(2C)	112.88(12)
O(4H)	La(1)	N(3A)	76.32(9)	O(1C)	La(2)	O(2C)	68.49(11)
O(1H)	La(1)	N(3A)	85.34(10)	O(5C)	La(2)	O(2C)	141.09(12)
O(1A)	La(1)	N(3A)	118.68(10)	O(7C)	La(2)	O(4C)	85.60(13)
O(2H)	La(1)	N(3A)	72.26(10)	O(3C)	La(2)	O(4C)	68.32(12)
O(3H)	La(1)	N(3A)	140.45(10)	O(1C)	La(2)	O(4C)	108.76(12)
O(1B)	La(1)	N(3B)	118.40(10)	O(5C)	La(2)	O(4C)	75.27(12)
O(4H)	La(1)	N(3B)	71.58(10)	O(2C)	La(2)	O(4C)	75.43(11)
O(1H)	La(1)	N(3B)	143.98(10)	O(7C)	La(2)	O(6C)#1	74.07(12)
O(1A)	La(1)	N(3B)	144.62(10)	O(3C)	La(2)	O(6C)#1	139.39(12)
O(2H)	La(1)	N(3B)	79.47(10)	O(1C)	La(2)	O(6C)#1	72.97(12)
O(3H)	La(1)	N(3B)	83.10(10)	O(5C)	La(2)	O(6C)#1	123.54(10)
N(3A)	La(1)	N(3B)	71.77(10)	O(2C)	La(2)	O(6C)#1	72.69(11)
O(1B)	La(1)	N(1A)	123.08(10)	O(4C)	La(2)	O(6C)#1	144.67(12)
O(4H)	La(1)	N(1A)	63.98(10)	O(7C)	La(2)	O(8C)#1	117.79(13)
O(1H)	La(1)	N(1A)	66.98(10)	O(3C)	La(2)	O(8C)#1	75.28(12)

O(1A)	La(1)	N(1A)	60.30(10)	O(1C)	La(2)	O(8C)#1	76.06(12)
O(2H)	La(1)	N(1A)	113.23(10)	O(5C)	La(2)	O(8C)#1	80.14(12)
O(3H)	La(1)	N(1A)	113.33(10)	O(2C)	La(2)	O(8C)#1	138.06(12)
N(3A)	La(1)	N(1A)	58.37(10)	O(4C)	La(2)	O(8C)#1	139.16(12)
N(3B)	La(1)	N(1A)	118.49(10)	O(6C)#1	La(2)	O(8C)#1	76.13(12)
O(1B)	La(1)	N(1B)	60.48(10)				

Symmetry transformations used to generate equivalent atoms: #1 $-x+2,-y+1,-z+1$

Table S24 Selected least-squares planes data for $[La(\mathbf{L2})_2(hfac)_2]_2[La_2(hfac)_4(O_2CCF_3)_4]$ (**7**).

Least-square planes

Least-squares planes description	Abbreviation	Max. deviation/Å	Atom
Pyridine N1A C1A C2A C3A C4A C5A	PyA	0.0154(12)	N1A
Benzimidazole N4A C11A N3A C12A C13A C14A C15A C16A C17A	BzA	0.0223(11)	N3A
Pyridine N1B C1B C2B C3B C4B C5B	PyB	0.0213(12)	N1B
Benzimidazole N4B C11B N3B C12B C13B C14B C15B C16B C17B	BzB	0.0204(11)	C11B
Hexafluoroacetylacetonate O1H C1H C2H C3H O2H	Hfa I	0.0459(11)	C3H
Hexafluoroacetylacetonate O3H C6H C7H C8H O4H	Hfa II	0.0435 (11)	C8H

Interplanar angles (°)

	PyA	BzA	PyB	BzB	Hfa I
BzA	3.11(3)				
PyB	19.90(3)	22.75(3)			
BzB	25.19(3)	28.28(2)	12.81(3)		
HfaI	57.24(4)	59.93(4)	37.45(4)	38.86(4)	
Hfa II	45.42(4)	43.13(4)	55.62(4)	67.07(4)	78.73(4)

Table S25 Bond Distances ($\delta_{i,j}$), Bond Valences ($v_{\mathrm{Ln,j}}$)[a] and Total Atom Valence (V_{Ln})[b] in the Crystal Structure of [La(**L2**)$_2$(hfac)$_2$]$_2$[La$_2$(hfac)$_4$(O$_2$CCF$_3$)$_4$] (**7**)

Atom[c]	Donor type	$\delta_{\mathrm{La1},j}$ / Å	$v_{\mathrm{La},j}$	
		[La(**L2**)$_2$(hfac)$_2$]$^+$		
N1A	py	2.769	0.253	Average N-heterocyclic
N1B	py	2.788	0.241	0.26 (2)
N3A	bzim	2.728	0.283	
N3B	bzim	2.757	0.262	
O1A	amide	2.549	0.338	Average O-amide
O1B	amide	2.507	0.379	0.36 (3)
O1H	hfac	2.543	0.344	
O2H	hfac	2.550	0.337	Average O-hfa
O3H	hfac	2.571	0.319	0.34 (1)
O4H	hfac	2.537	0.349	
		V_{La1}	3.106	
		[La(hfac)$_4$(O$_2$CCF$_3$)$_4$]$^{2-}$		
O1C	hfac	2.494	0.393	
O2C	hfac	2.497	0.389	
O3C	hfac	2.493	0.394	Average O-hfac
O4C	hfac	2.507	0.379	0.39 (1)
O5C	OAc$_F$	2.495	0.391	
O6C	OAc$_F$	2.510	0.376	
O7C	OAc$_F$	2.460	0.430	Average O-OAc$_F$
O8C	OAc$_F$	2.543	0.344	0.39 (4)
		V_{La2}	3.096	

[a] $v_{\mathrm{Ln},j} = e^{\left[\left(R_{\mathrm{Ln},j} - d_{\mathrm{Ln},j}\right)/b\right]}$, whereby $\delta_{\mathrm{Ln},,j}$ is the Ln-donor atom j distance. The valence bond parameters $R_{\mathrm{Ln,N}}$ and $R_{\mathrm{Ln,O}}$ are taken from ref 29e,f and b = 0.37 Å. [b] $V_{\mathrm{Ln}} = \sum_j v_{\mathrm{Ln},j}$. [c] Numbering taken from Fig S13.

Table S26 Ligand-centered absorption and emission properties of **L2**-**L4** and of their complexes $[Ln_m(\mathbf{L}\boldsymbol{k})(hfac)_{3m}]$ in the solid state.

Compound	Absorption /cm^{-1} [a] $^1\pi^* \leftarrow {}^1\pi$	Emission /cm^{-1} [b] $^1\pi^* \rightarrow {}^1\pi$	Emission /cm^{-1} [b] $^3\pi^* \rightarrow {}^1\pi$	Lifetime /ms τ ($^3\pi^*$)
L2	31445	29110 sh	21280 sh	3.9(2)
		27780	20000	
		26455 sh	18870 sh	
L3	29585	28250 sh	20408 sh	1.7(1)
		26990	19420	
		23725		
L4	30395	27780 sh	20000 sh	1.4(1)
		26665	19050	
		21645 sh		
[Lu(**L2**)(hfac)$_3$]	31545	25350	20830 sh	1.08(6)
			19420	
			18180 sh	
[Gd(**L2**)(hfac)$_3$]	31545	24875	21740 sh	1.06(5)
	28490 sh		20620	
			19610 sh	
			18180 sh	
[Eu(**L2**)(hfac)$_3$]	31750	[c]	[c]	-
	28490 sh			
[Lu$_2$(**L3**)(hfac)$_6$]	31350	24875	20620 sh	2.4(2)
	27780 sh		19420	
			18350 sh	
[Gd$_2$(**L3**)(hfac)$_3$]	31446	24783	21276 sh	0.19(1)
	27933 sh		19802	
			18518 sh	
[Eu$_2$(**L3**)(hfac)$_6$]	31650	[c]	[c]	-
	27470 sh			
[Gd$_3$(**L4**)(hfac)$_9$]	31250	23980	20620 sh	0.20(3)
	26525 sh		19230	
			17860 sh	
[Eu$_3$(**L4**)(hfac)$_9$]	31850	[c]	[c]	-
	26670 sh			

[a] Reflectance spectra recorded from MgO matrices at 293 K, sh = shoulder. [b] Recorded at 77 K with $\bar{\nu}_{exc}$ = 30300 cm^{-1}. [c] Quenched by quantitative transfer onto Eu(III).

Table S27 Integral intensities of $^5D_0 \rightarrow {}^7F_J$ ($J = 0 - 4$) transitions in Eu^{III} complexes.[a]

Compound	$\int_{0\text{-}0}$	$\int_{0\text{-}1}$	$\int_{0\text{-}2}$	$\int_{0\text{-}3}$	$\int_{0\text{-}4}$	$\int_{tot}/\int_{0\text{-}1}$
[Eu(**L2**)(hfac)$_3$]	0.14	1.0	12.64	0.28	1.39	15.46
[Eu$_2$(**L3**)(hfac)$_6$]	0.12	1.0	12.18	0.25	1.34	14.89
[Eu$_3$(**L4**)(hfac)$_9$]	0.10	1.0	11.34	0.19	1.32	13.94

[a] Experimental error, ±5%.

Table S28 ^{1}H NMR shifts of aromatic part (in ppm with respect to TMS) for the ligand **L2** and its complexes [Ln(**L2**)(hfac)$_3$] in CD_3CN at 293 K (Ln = La, Y, Lu).

	H1	H2	H3	H4	H5	H6	H7	H-hfac
L2	7.58	7.36	7.30	7.74	8.37	8.02	7.51	-
[La(**L2**)$_2$(hfac)$_3$]	7.65	7.44	7.30	8.03	8.21	8.35	7.99	5.90
[Y(**L2**)(hfac)$_3$]	7.63	7.42	7.27	8.20	8.25	8.34	8.01	5.87
[Y(**L2**)(hfac)$_2$]$^+$	7.72	7.50	7.40	8.11	8.44	8.44	8.09	5.87
[Lu(**L2**)(hfac)$_3$]	7.64	7.43	7.30	8.22	8.27	8.35	8.04	5.87
[Lu(**L2**)(hfac)$_2$]$^+$	7.71	7.51	7.40	8.07	8.36	8.46	8.13	6.14

Table S29 ^{19}F NMR shifts (in ppm with Respect to Hexafluorobenzene) for the complexes [Ln(**L2**)(hfac)$_3$] at 293 K (Ln = La, Eu, Y, Lu).

	δ/$CDCl_3$	δ/CD_3CN
$[La(\mathbf{L2})_2(hfac)_2]^+$	-	-77.06
$[La_2(hfac)_4(CF_3COO)_4]^{2-}$	-	-77.41
[La(**L2**)(hfac)$_3$]	-76.78	-77.41
[Eu(**L2**)(hfac)$_3$]		-79.93
[Y(**L2**)(hfac)$_3$]	-76.86	-77.48
$[Y(\mathbf{L2})(hfac)_2]^+$	-	-77.21
[Lu(**L2**)(hfac)$_3$]	-76.93	-77.47
$[Lu(\mathbf{L2})(hfac)_2]^+$	-	-77.14

Table S30 Cumulative thermodynamic formation constants $\log(\beta_{m,1}^{\mathrm{Ln(hfac)3,\mathbf{Lk}}})$, associated intermolecular microscopic affinities ($\Delta G_{\mathrm{inter}}^{\mathrm{Ln,N3}} = -RT\ln\left(f_{\mathrm{N3}}^{\mathrm{Ln}}\right)$ and $\Delta G_{\mathrm{inter}}^{\mathrm{Ln,N2O}} = -RT\ln\left(f_{\mathrm{N2O}}^{\mathrm{Ln}}\right)$ in kJ/mol) and intermetallic ($\Delta E_{1-2}^{\mathrm{Ln,Ln}} = -RT\ln\left(u_{1-2}^{\mathrm{Ln,Ln}}\right)$ and $\Delta E_{1-3}^{\mathrm{Ln,Ln}} = -RT\ln\left(u_{1-3}^{\mathrm{Ln,Ln}}\right)$ in kJ/mol) interactions obtained for [Ln_m(**L*k***)$(\mathrm{hfac})_{3m}$] (Ln = La, Eu, Y, Lu; CH_3CN, 298 K).

Metal	La	Eu	Y	Lu	Reference
$\log(\beta_{1,1}^{\mathrm{Ln(hfac)3,\mathbf{L1}}})$	5.7(1)	5.94(9)	5.15(5)	4.3(3)	18
$\log(\beta_{1,1}^{\mathrm{Ln(hfac)3,\mathbf{L2}}})$	5.66(6)	6.3(1)	5.47(8)	5.57(6)	This work
$\log(\beta_{1,1}^{\mathrm{Ln(hfac)3,\mathbf{L3}}})$	5.93(8)	6.6(1)	5.79(7)	4.02(9)	This work
$\log(\beta_{2,1}^{\mathrm{Ln(hfac)3,\mathbf{L3}}})$	10.95(6)	11.9(1)	10.87(6)	7.34(5)	This work
$\log(\beta_{1,1}^{\mathrm{Ln(hfac)3,\mathbf{L4}}})$	4.5(1)	5.40(7)	3.9(2)	*5.52(9)* [a]	This work
$\log(\beta_{2,1}^{\mathrm{Ln(hfac)3,\mathbf{L4}}})$	9.88(7)	10.70(7)	9.50(1)	*11.6(1)* [a]	This work
$\log(\beta_{3,1}^{\mathrm{Ln(hfac)3,\mathbf{L4}}})$	14.01(9)	16.25(6)	13.9(1)	*17.1(1)* [a]	This work
$\log(f_{\mathrm{N2O}}^{\mathrm{Ln,\mathbf{L2}}})$/ $\Delta G_{\mathrm{inter}}^{\mathrm{Ln,N2O,\mathbf{L2}}}$	5.2(2)/-30(1)	5.8(2)/-33(1)	5.0(3)/-29(1)	-	This work
$\log(f_{\mathrm{N2O}}^{\mathrm{Ln}})/\Delta G_{\mathrm{inter}}^{\mathrm{Ln,N2O}}$	4.8(2)/-27(1)	4.9(2)/-30(1)	4.5(3)/-26(1)	-	This work
$\log(f_{\mathrm{N3}}^{\mathrm{Ln,\mathbf{L1}}})/\Delta G_{\mathrm{inter}}^{\mathrm{Ln,N3,\mathbf{L1}}}$	5.2(1)/-30(1)	5.5(1)/-31(1)	4.7(1)/-27(1)	-	18
$\log(f_{\mathrm{N3}}^{\mathrm{Ln}})/\Delta G_{\mathrm{inter}}^{\mathrm{Ln,N3}}$	3.1(2)/-18(1)	3.2(2)/-18(1)	2.5(3)/-14(1)	-	This work
$\log(u_{1-2}^{\mathrm{Ln,Ln}})/\Delta E_{1-2}^{\mathrm{Ln,Ln}}$	0.4(2)/-2(1)	1.1(2)/-6(1)	0.9(3)/-5(1)	-	This work
$\log(u_{1-3}^{\mathrm{Ln,Ln}})/\Delta E_{1-3}^{\mathrm{Ln,Ln}}$	-0.9(2)/5(1)	-0.4(2)/2(1)	-0.8(3)/5(1)	-	This work

[a] Due to major difficulties during the fitting process, these values are only mere estimates (see text).

Table S31 Cumulative thermodynamic formation constants log($\beta_{m,1}^{\mathrm{Ln(NO3)3,}\mathbf{Lk}}$), associated intermolecular microscopic affinities ($\Delta G_{\mathrm{inter}}^{\mathrm{Ln,N3}} = -RT\ln\left(f_{\mathrm{N3}}^{\mathrm{Ln}}\right)$ and $\Delta G_{\mathrm{inter}}^{\mathrm{Ln,N2O}} = -RT\ln\left(f_{\mathrm{N2O}}^{\mathrm{Ln}}\right)$ in kJ/mol) and intermetallic ($\Delta E_{1-2}^{\mathrm{Ln,Ln}} = -RT\ln\left(u_{1-2}^{\mathrm{Ln,Ln}}\right)$ and $\Delta E_{1-3}^{\mathrm{Ln,Ln}} = -RT\ln\left(u_{1-3}^{\mathrm{Ln,Ln}}\right)$ in kJ/mol) interactions obtained for [Ln_m(**L*k***)$(\mathrm{NO_3})_{3m}$] (Ln = La, Eu, Y, Lu; $\mathrm{CH_3CN}$, 298 K).

Metal	La	Eu	Y	Lu	Reference
log($\beta_{1,1}^{\mathrm{Ln(NO3)3,}\mathbf{L2}}$)	5.77(6)	5.27(9)	5.99(9)	6.06(9)	19
log($\beta_{1,1}^{\mathrm{Ln(NO3)3,}\mathbf{L3}}$)	5.09(9)	5.49(4)	5.69(8)	5.79(9)	19
log($\beta_{2,1}^{\mathrm{Ln(NO3)3,}\mathbf{L3}}$)	9.20(8)	9.42(6)	10.12(9)	10.36(9)	19
log($\beta_{1,1}^{\mathrm{Ln(NO3)3,}\mathbf{L4}}$)	6.4(2)	6.8(2)	6.8(2)	*7.9(2)* [a]	This work
log($\beta_{2,1}^{\mathrm{Ln(NO3)3,}\mathbf{L4}}$)	12.3(2)	12.7(3)	12.7(2)	*14.2(3)* [a]	This work
log($\beta_{3,1}^{\mathrm{Ln(NO3)3,}\mathbf{L4}}$)	17.3(2)	17.4(3)	17.8(2)	*19.8(3)* [a]	This work
log($f_{\mathrm{N2O(}\mathbf{L2}\mathrm{)}}^{\mathrm{Ln}}$)/ $\Delta G_{\mathrm{inter}}^{\mathrm{Ln,N2O,}\mathbf{L2}}$	5.3(2)/-30(1)	4.8(2)/-27(1)	5.6(3)/-32(2)	-	19
log($f_{\mathrm{N2O}}^{\mathrm{Ln}}$)/ $\Delta G_{\mathrm{inter}}^{\mathrm{Ln,N2O}}$	4.5(1)/-25.6(4)	4.7(1)/-26.9(3)	4.9(3)/-28.3(4)	-	This work
log($f_{\mathrm{N3(}\mathbf{L1}\mathrm{)}}^{\mathrm{Ln,}}$)/ $\Delta G_{\mathrm{inter}}^{\mathrm{Ln,N3,}\mathbf{L1}}$	4.2(2)/-24.1(8)	4.2(2)/-24.2(8)	4.4(2)/-25.1(9		47
log($f_{\mathrm{N3}}^{\mathrm{Ln}}$)/ $\Delta G_{\mathrm{inter}}^{\mathrm{Ln,N3}}$	6.3(1)/-35.5(1)	6.2(1)/-35.5(1)	6.2(1)/-35.5(1)	-	This work
log($u_{1-2}^{\mathrm{Ln,Ln}}$)/ $\Delta E_{1-2}^{\mathrm{Ln,Ln}}$	-0.8(1)/4.6(2)	-0.8(2)/5.4(4)	-0.8(1)/4.4(2)	-	This work
log($u_{1-3}^{\mathrm{Ln,Ln}}$)/ $\Delta E_{1-3}^{\mathrm{Ln,Ln}}$	2.3(1)/-13(1)	2.2(3)/-12(2)	1.8(1)/-10(1)	-	This work

[a] Due to major difficulties during the fitting process, these values are only mere estimates (see text).

Table S32 ^{1}H NMR shifts of aromatic part (in ppm with respect to TMS) for the ligand **L2** and its complexes [Ln(**L2**)(hfac)$_3$] in $CDCl_3$ at 293 K (Ln = La, Y, Lu).

Compound	H1	H2	H3	H4	H5	H6	H7	H-hfac
L2	7.47	7.37	7.33	7.87	8.44	7.96	7.57	-
[La(**L2**)(hfac)$_3$]	7.41	7.41	7.34	8.19	7.95	8.19	7.72	5.85
[Y(**L2**)(hfac)$_3$]	7.39	7.39	7.32	8.36	7.97	8.19	7.76	5.84
[Lu(**L2**)(hfac)$_3$]	7.40	7.40	7.33	8.38	8.02	8.19	7.77	5.82

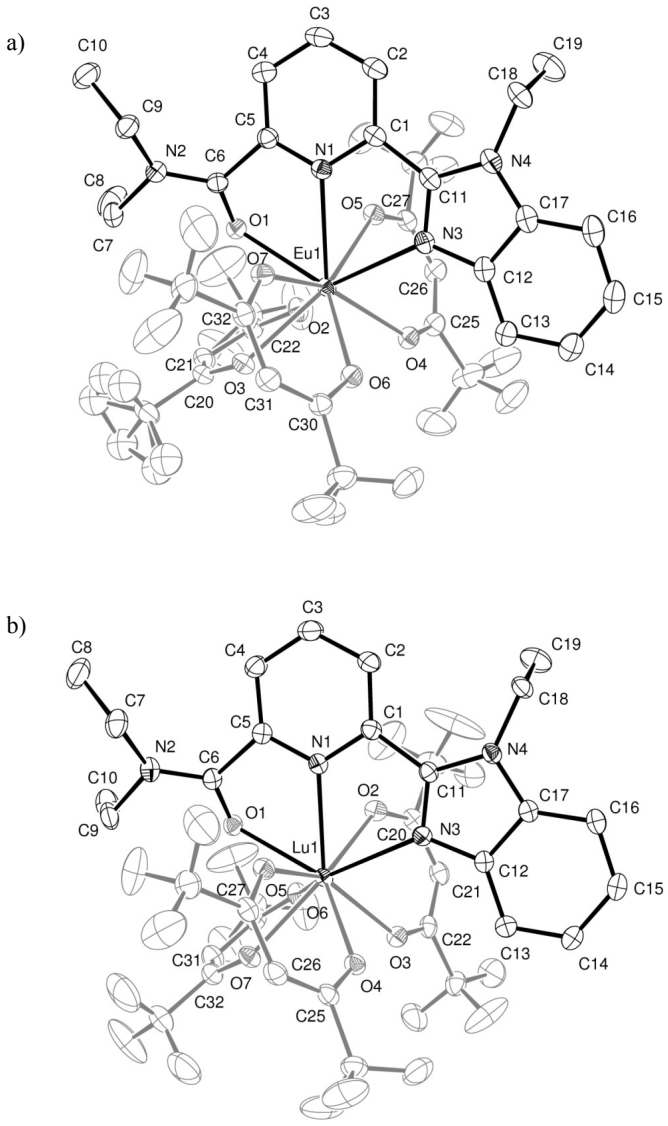

Figure S1 Molecular structures with partial numbering schemes of the assymetric units for a) [Eu(**L2**)(hfac)$_3$] and b) [Lu(**L2**)(hfac)$_3$] in the crystal structures of **2** and **5** (thermal ellipsoids are represented at the 30% probability level). Hydrogen atoms are omitted for clarity.

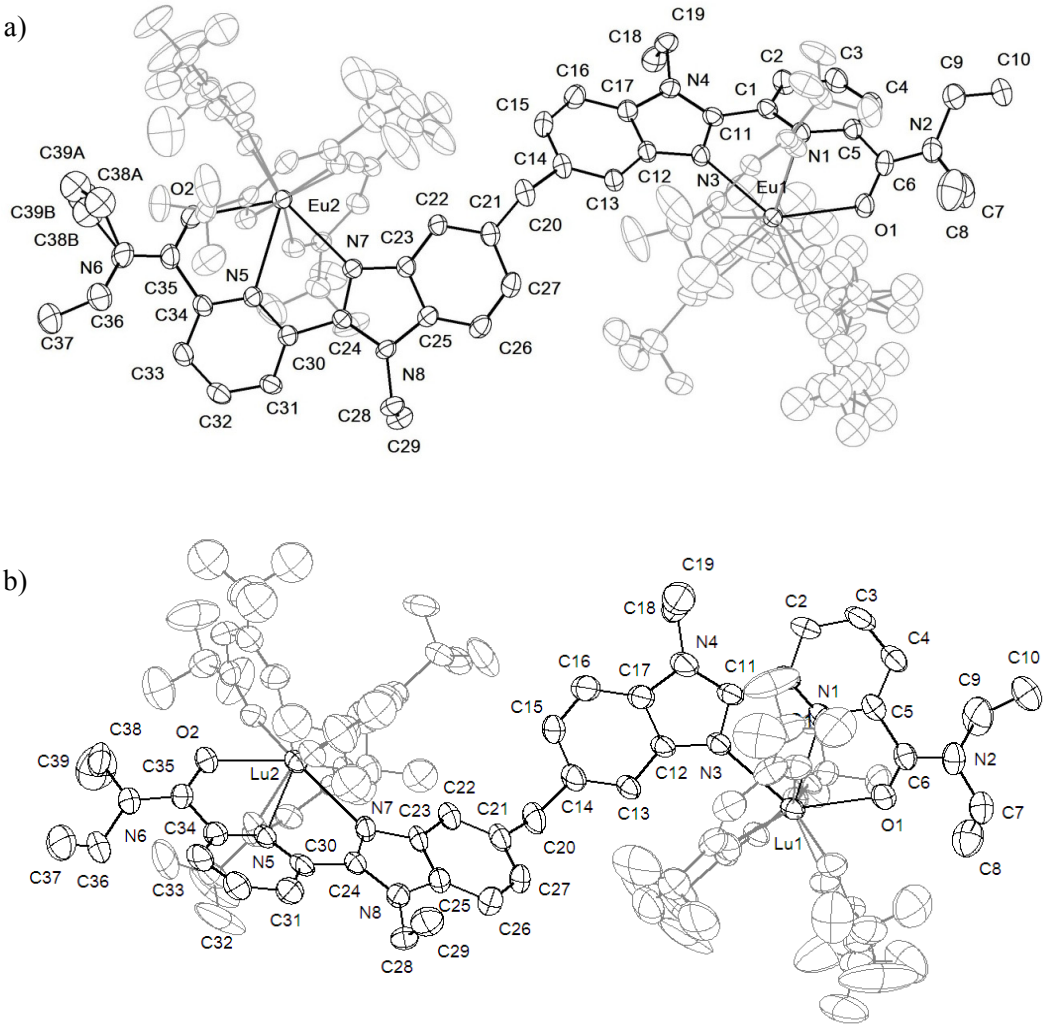

Figure S2 Molecular structures with partial numbering schemes of the assymetric units for a) $[Eu_2(\mathbf{L3})(hfac)_6]$ and b) $[Lu_2(\mathbf{L3})(hfac)_6]$ in the crystal structures of **3** and **6** (thermal ellipsoids are represented respectively at the 30% and 50% probability levels). Hydrogen atoms are omitted for clarity.

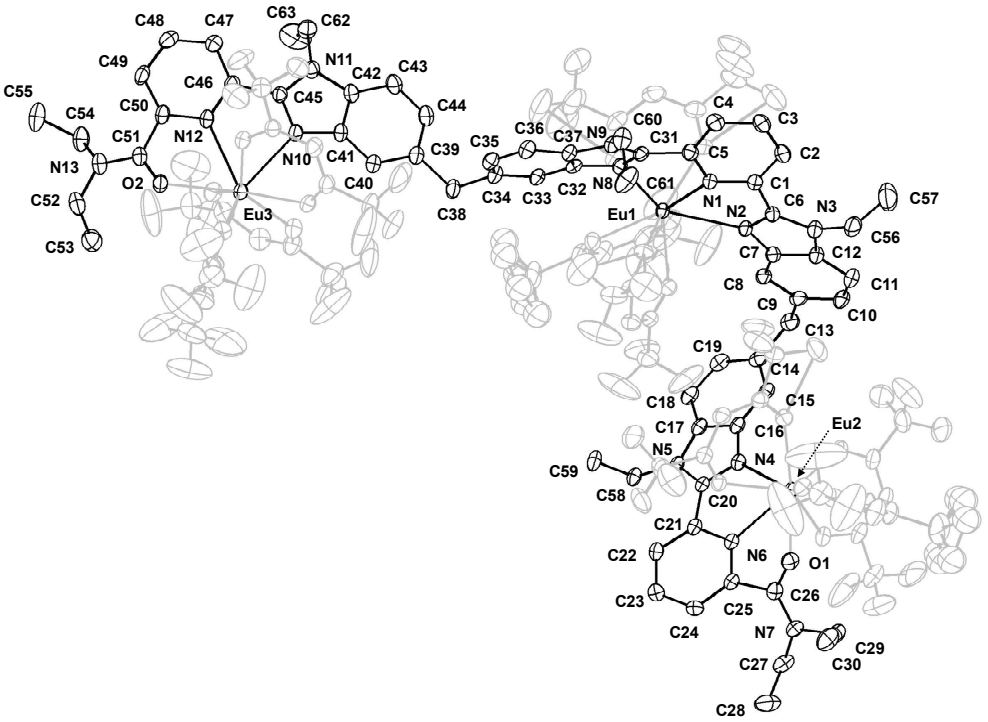

Figure S3 Molecular structure with partial numbering scheme of the assymetric unit for [Eu_3(**L4**)(hfac)$_9$] in the crystal structure of **4** (thermal ellipsoids are represented at the 30% probability level). Hydrogen atoms are omitted for clarity.

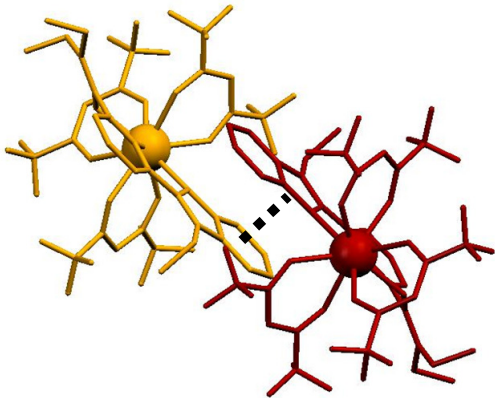

Figure S4 Intermolecular π-stacking benzimidazole···benzimidazole interactions (d = 3.35Å) found in [Lu(**L2**)(hfac)$_3$] (**5**) involving neighbouring molecules related by inversion centres.

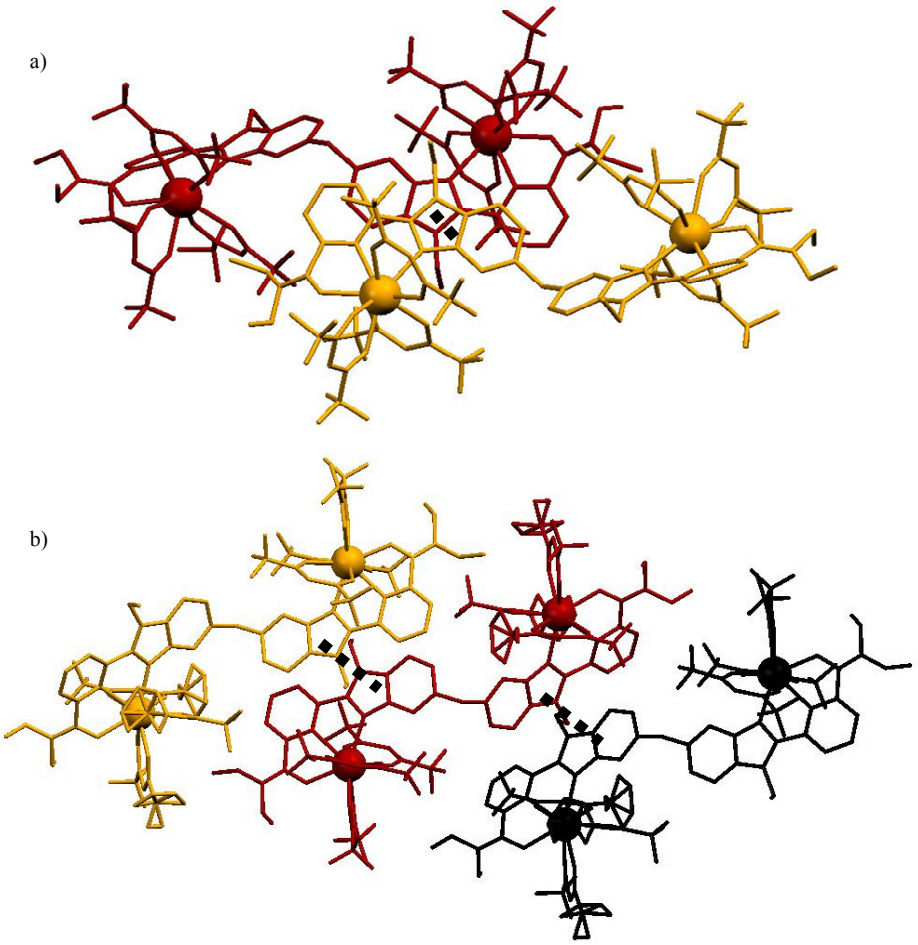

Figure S5 Intermolecular π-stacking benzimidazole···benzimidazole interactions found in a) $[Eu_2(\mathbf{L3})(hfac)_6]$ (**3**) (d = 3.50Å) and b) $[Lu_2(\mathbf{L3})(hfac)_6]$ (**6**) (d = 3.60Å) involving neighbouring molecules related by inversion centres.

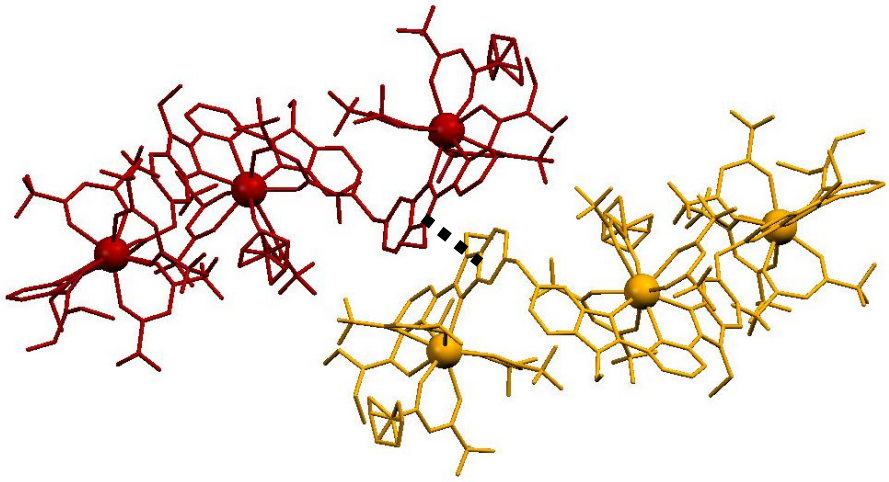

Figure S6 Intermolecular π-stacking benzimidazole···benzimidazole interactions (d = 3.32Å) interactions found in $[Eu_3(\mathbf{L4})(hfa)_9]$ (**4**) involving neighbouring molecules related by inversion centres.

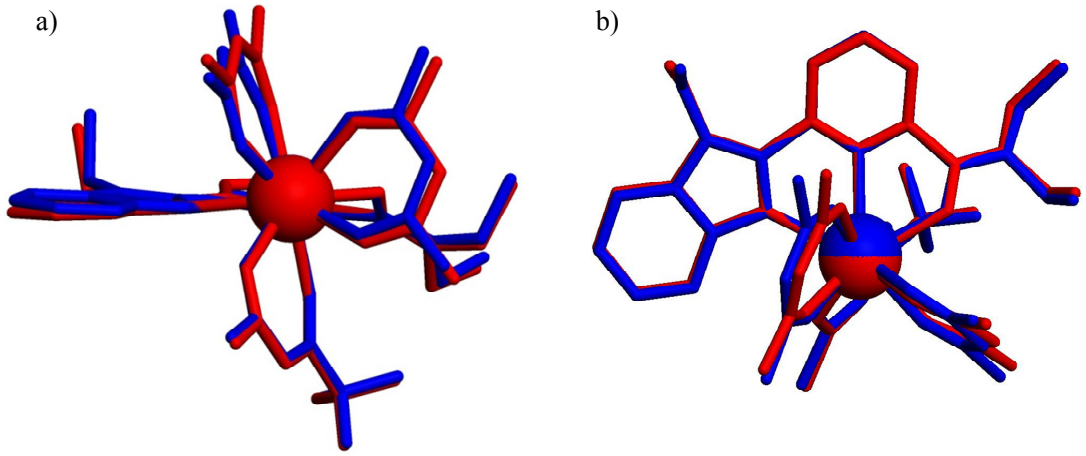

Figure S7 Superimposition of the molecular structures of [Eu(**L2**)(hfac)$_3$] (red) and [Lu(**L2**)(hfac)$_3$] (blue). Perspective views a) along and b) perpendicular to the pyridine plane of the tridentate ligand. Hydrogen and fluorine atoms are omitted for clarity.

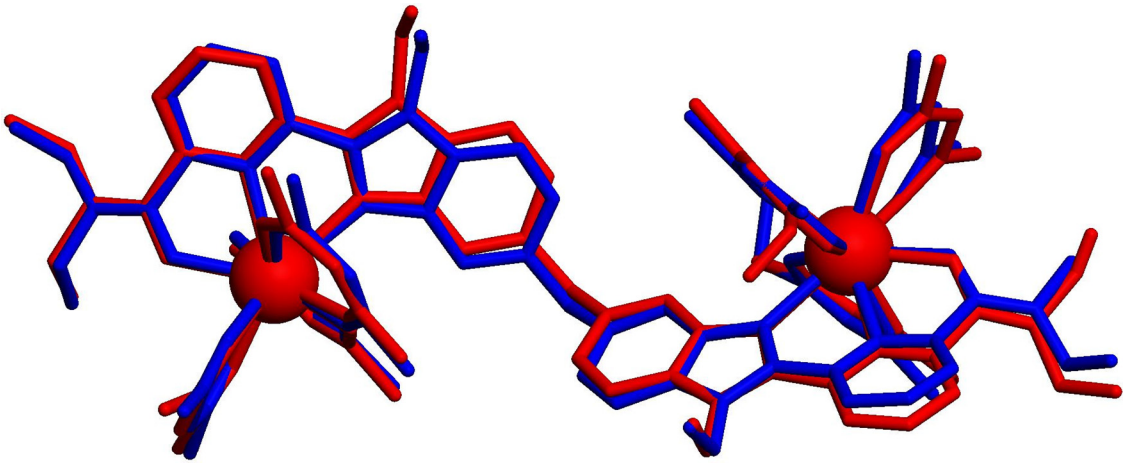

Figure S8 Superimposition of the molecular structures of [Eu$_2$(**L3**)(hfac)$_6$] (red) and [Lu$_2$(**L3**)(hfac)$_6$] (blue). Hydrogen and fluorine atoms are omitted for clarity.

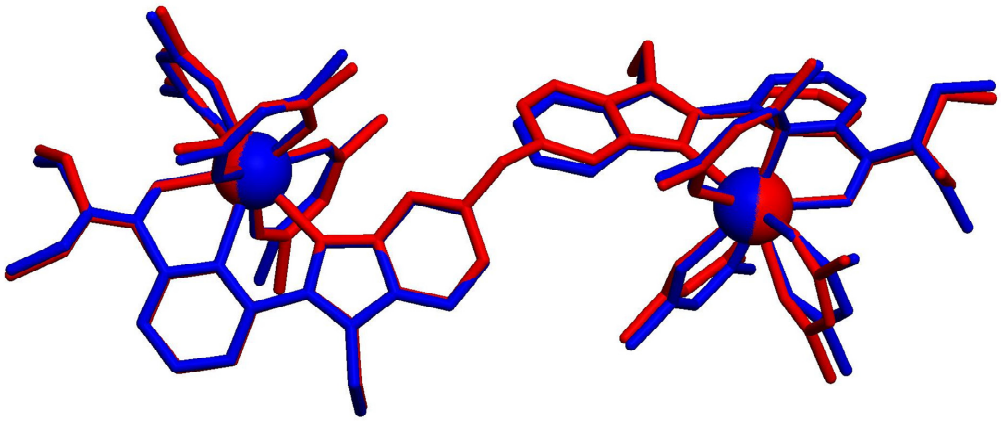

Figure S9 Superimposition of the molecular structures of $[Eu_2(\mathbf{L3})(hfac)_6]$ (red) and $[Eu_2(\mathbf{L2})(hfac)_3]$ (twice, blue). Hydrogen and fluorine atoms are omitted for clarity.

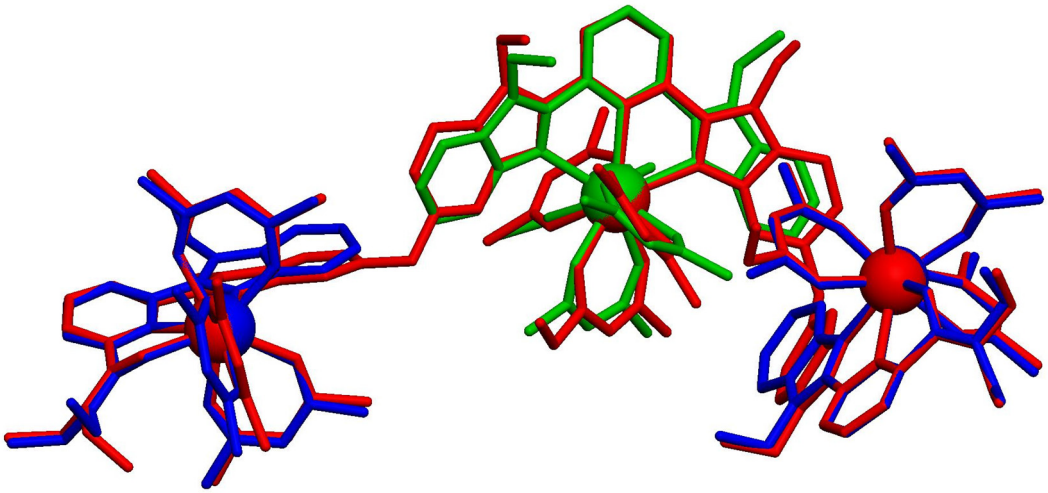

Figure S10 Superimposition of the molecular structures of $[Eu_3(\mathbf{L4})(hfac)_9]$ (red) and $[Eu_2(\mathbf{L2})(hfac)_3]$ (twice, blue) and $[Eu(\mathbf{L1})(hfac)_3]$ (green). Hydrogen and fluorine atoms are omitted for clarity.

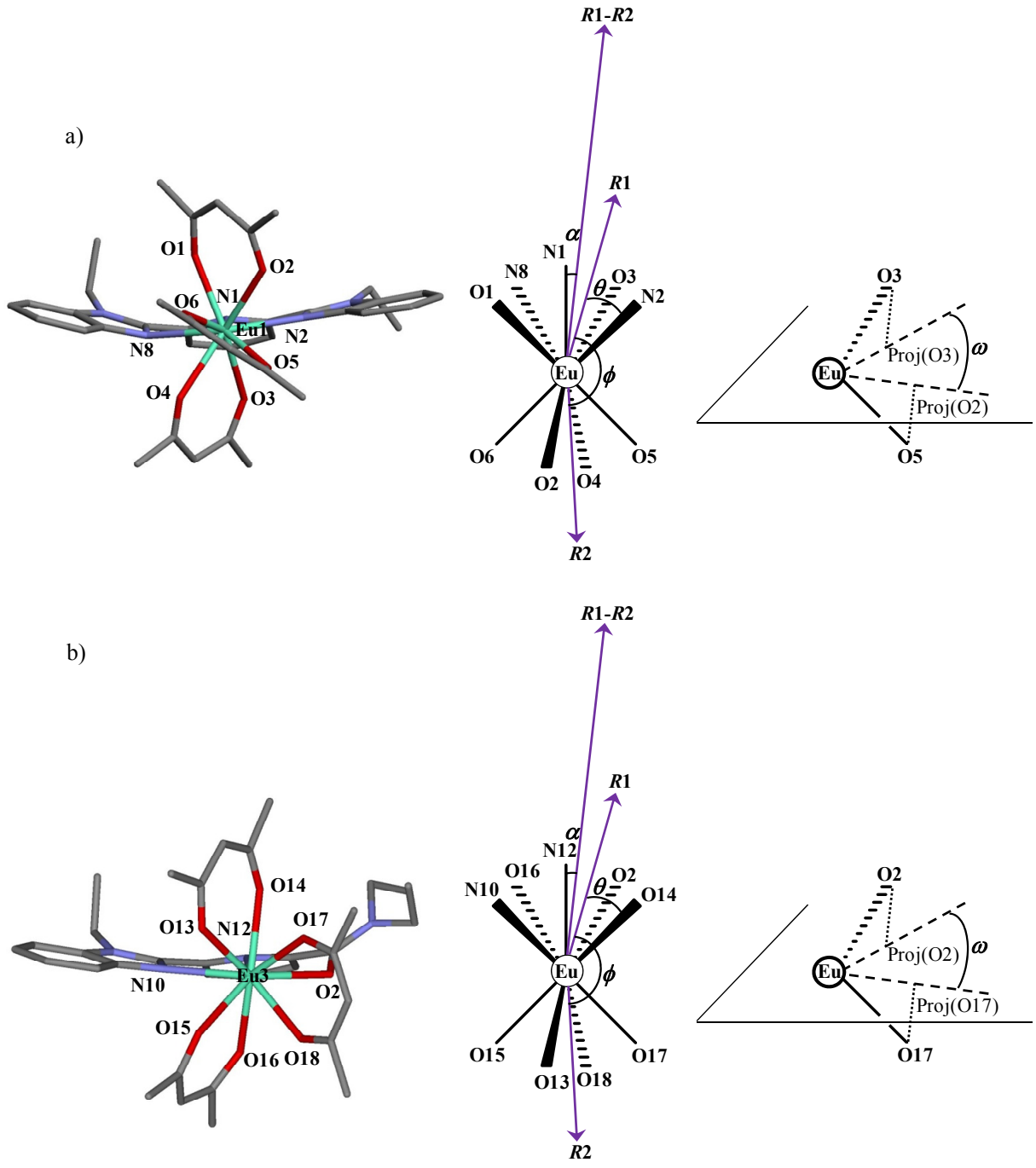

Figure S11 Perspective views along the Eu-N(pyridine) direction (left) and associated angles α, ϕ, θ and ω characterizing the pseudo-monocapped square antiprismatic geometry adopted by the coordination spheres around Eu^{III} in a) the central $[Eu(N_3)(hfac)_3]$ unit and b) the distal $[Eu(N_2O)(hfac)_3]$ unit in the trinuclear $[Eu_3(\mathbf{L4})(hfac)_9]$. Hydrogen and fluorine atoms are omitted for clarity.

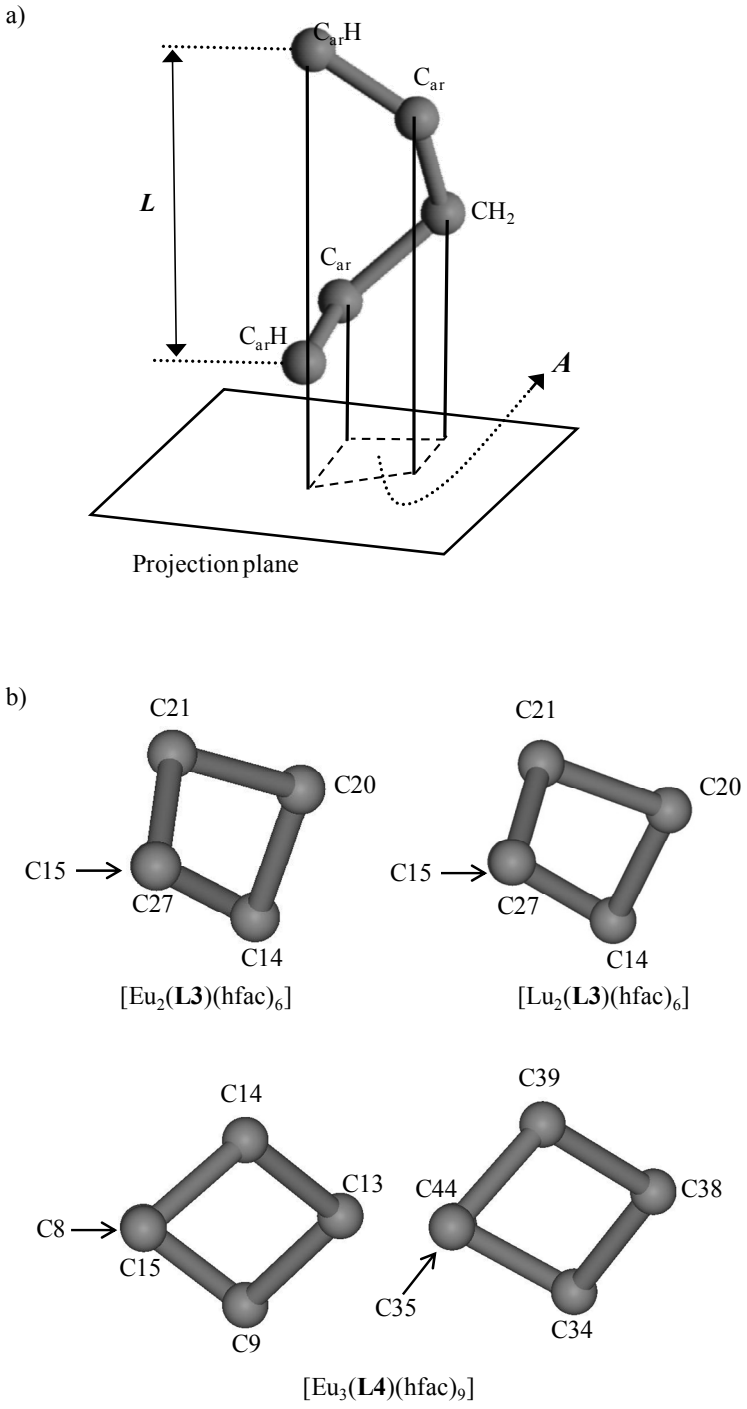

Figure S12 a) Analysis of the helicity of a five-atoms crooked line proposed by Brewster (*L* is the end to end distance of the helix, *A* is the area of the subtended figure in the projection plane and *D* is the total length of the crooked line).[30] b) Subtended geometrical figures obtained in the projection plane for $[Eu_2(\mathbf{L3})(hfac)_6]$, $[Lu_2(\mathbf{L3})(hfac)_6]$ and $[Eu_3(\mathbf{L4})(hfac)_9]$.

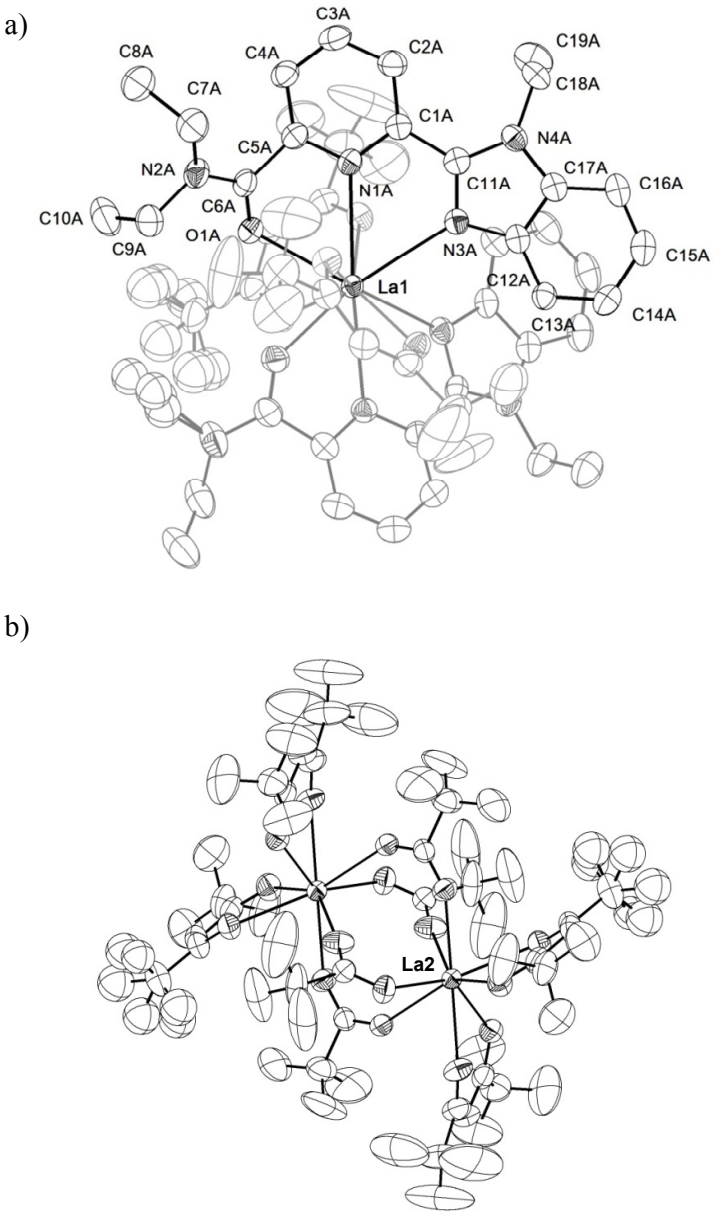

Figure S13 Molecular structure with partial numbering scheme of a) $[La(\mathbf{L2})_2(hfac)_2]^+$ and b) $[La_2(hfac)_4(O_2CCF_3)_4]^{2-}$ in the crystal structure of **7** (thermal ellipsoids are represented at the 50% probability level). Hydrogen atoms are omitted for clarity.

a)

b)

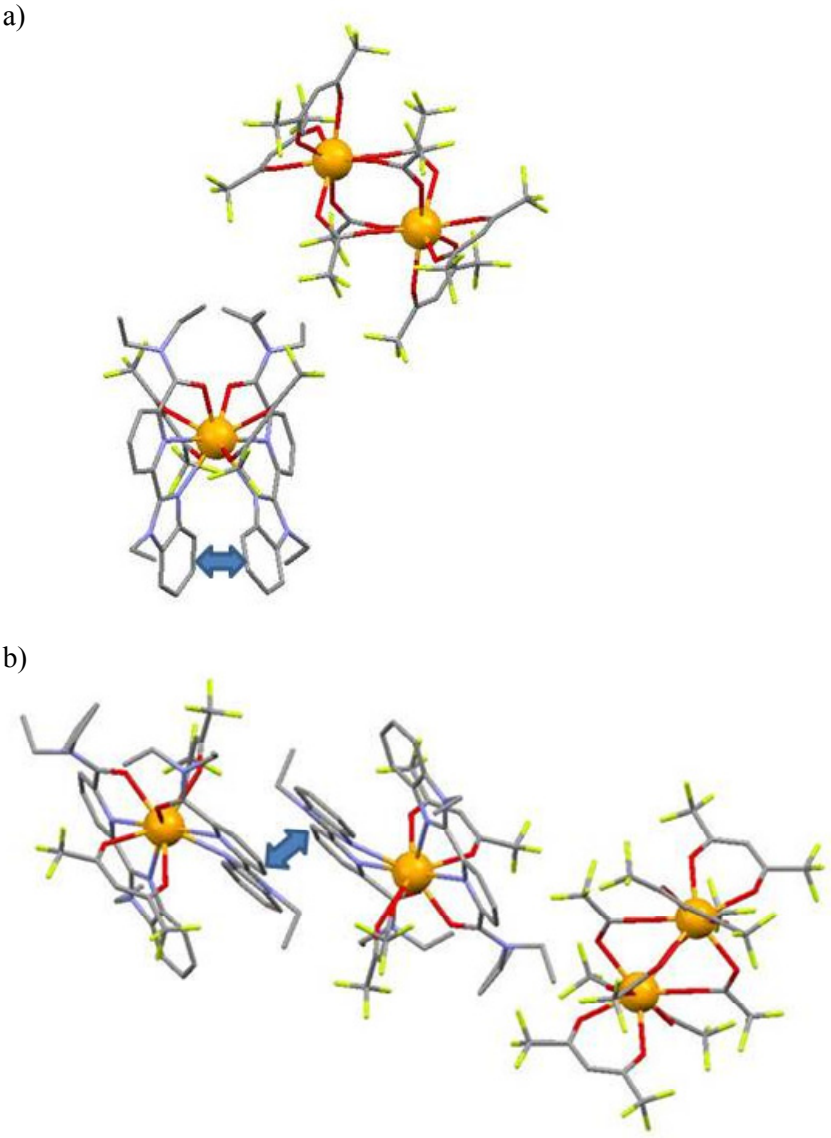

Figure S14 a) Intramolecular (interplanar angle = 28° *d* = 3.7 Å and b) intermolecular π-stacking benzimidazole···benzimidazole interactions (3.36(1) Å) found in $[La(\mathbf{L2})_2(hfac)_2]^+$ in the crystal structure of **7**.

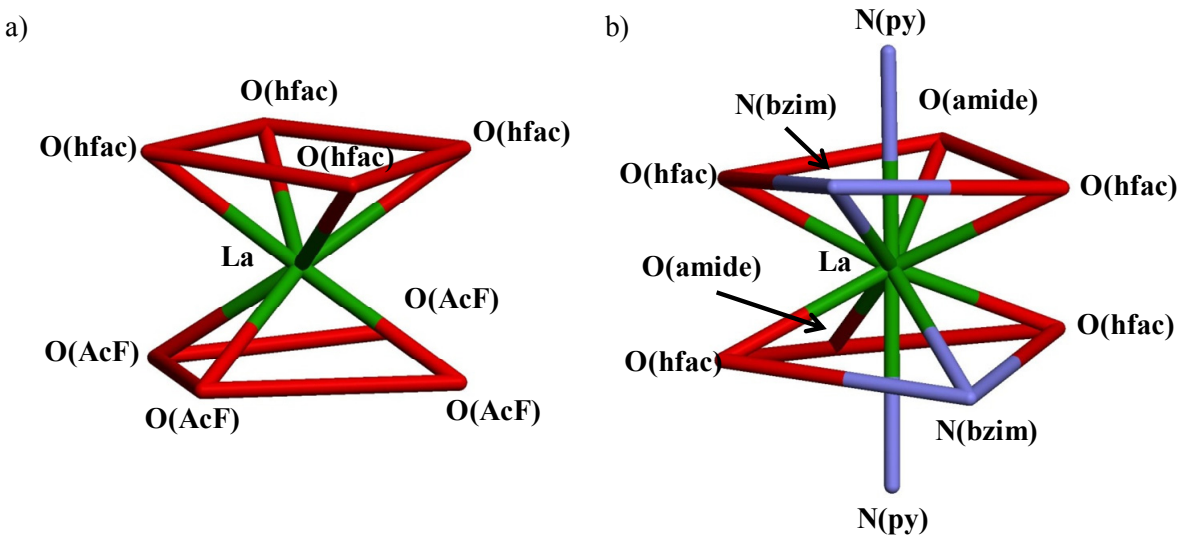

Figure S15 Coordination spheres around La^{III} in a) $[La_2(hfac)_4(O_2CCF_3)_4]^{2-}$ (pseudo-square antiprism) and b) $[La(\mathbf{L2})_2(hfac)_2]^{+}$ (pseudo-bicapped square antiprism) in the crystal structure of **7**.

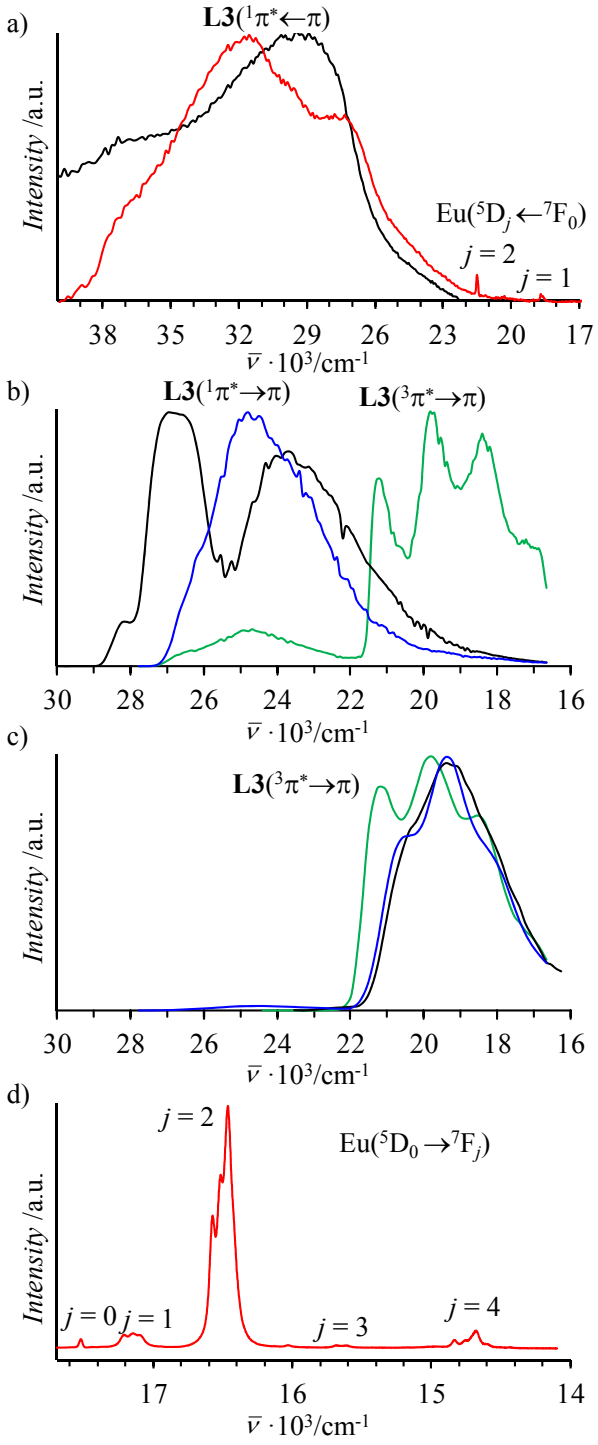

Figure S16 Solid state a) reflectance absorption spectra (293 K), b) emission spectra ($\bar{\nu}_{exc}$ = 30300-29500 cm^{-1}, 77 K), c) phosphorescence spectra ($\bar{\nu}_{exc}$ = 30300-29500 cm^{-1}, delay time after excitation flash 5 μs, 77 K) d) luminescence spectra ($\bar{\nu}_{exc}$ = 28170 cm^{-1} [1] at 293 K) recorded for **L3** (black traces), $[Lu_2(\mathbf{L3})(hfac)_6]$ (blue traces), $[Gd_2(\mathbf{L3})(hfac)_6]$ (green traces) and $[Eu_2(\mathbf{L3})(hfac)_6]$ (red traces).

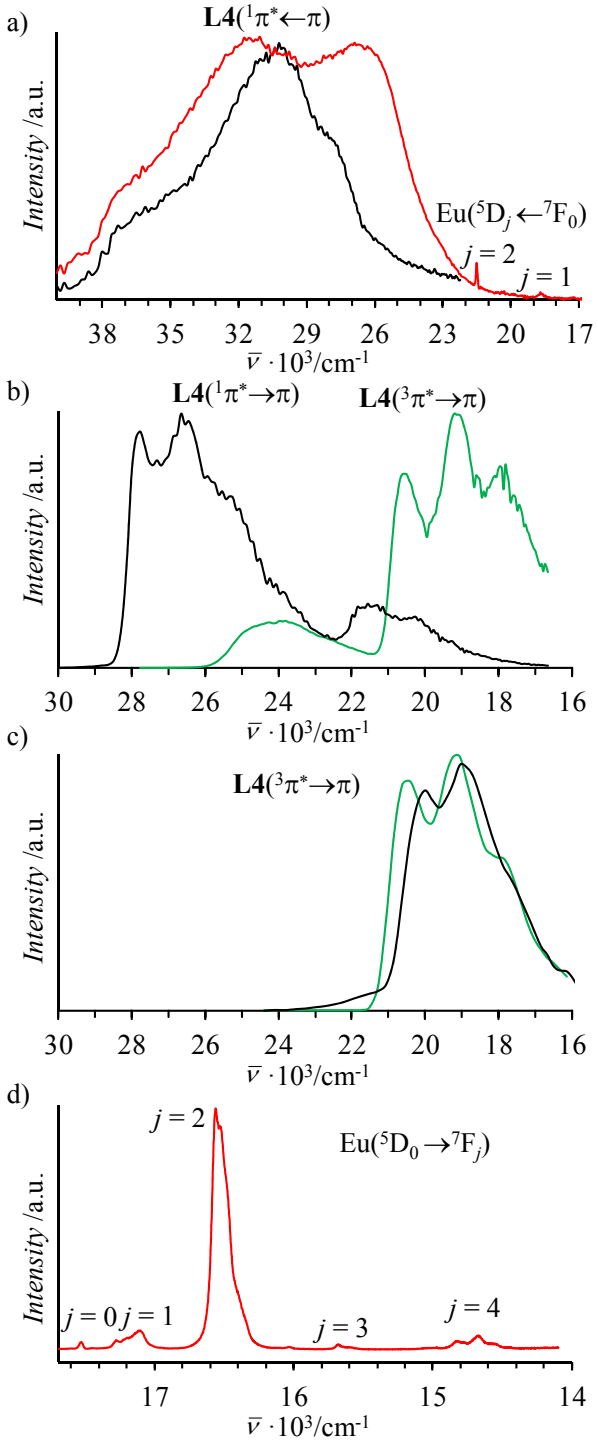

Figure S17 Solid state a) reflectance absorption spectra (293 K), b) emission spectra ($\bar{\nu}_{exc}$ = 30300-29500 cm^{-1}, 77 K), c) phosphorescence spectra ($\bar{\nu}_{exc}$ = 30300-29500 cm^{-1}, delay time after excitation flash 5 μs, 77 K) d) luminescence spectra ($\bar{\nu}_{exc}$ = 28170 cm^{-1} [1] at 293 K) recorded for **L4** (black traces), $[Gd_3(\mathbf{L4})(hfac)_9]$ (green traces) and $[Eu_3(\mathbf{L4})(hfac)_9]$ (red traces).

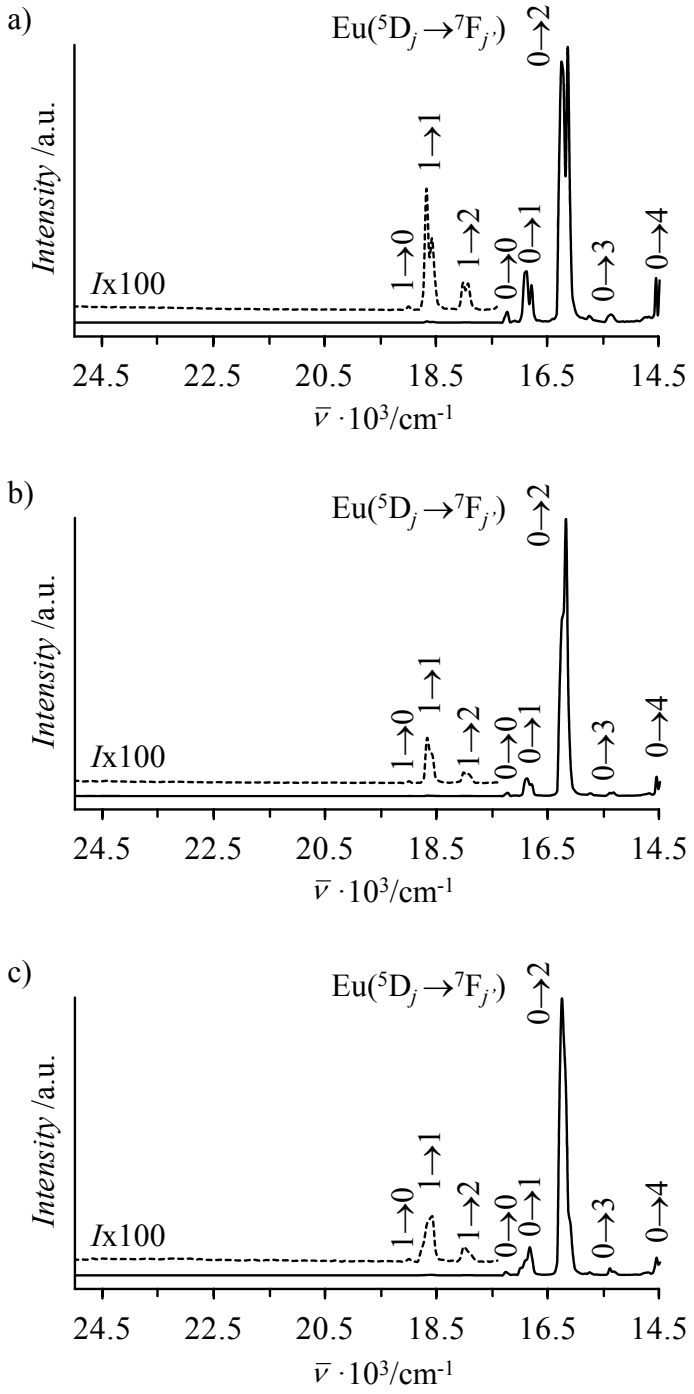

Figure S18 Luminescence spectra ($\bar{\nu}_{exc}$ = 29000 cm^{-1}, solid state 77 K) recorded for a) [Eu(**L2**)(hfac)$_3$], b) [Eu$_2$(**L3**)(hfac)$_6$] and c) [Eu$_3$(**L4**)(hfac)$_9$].

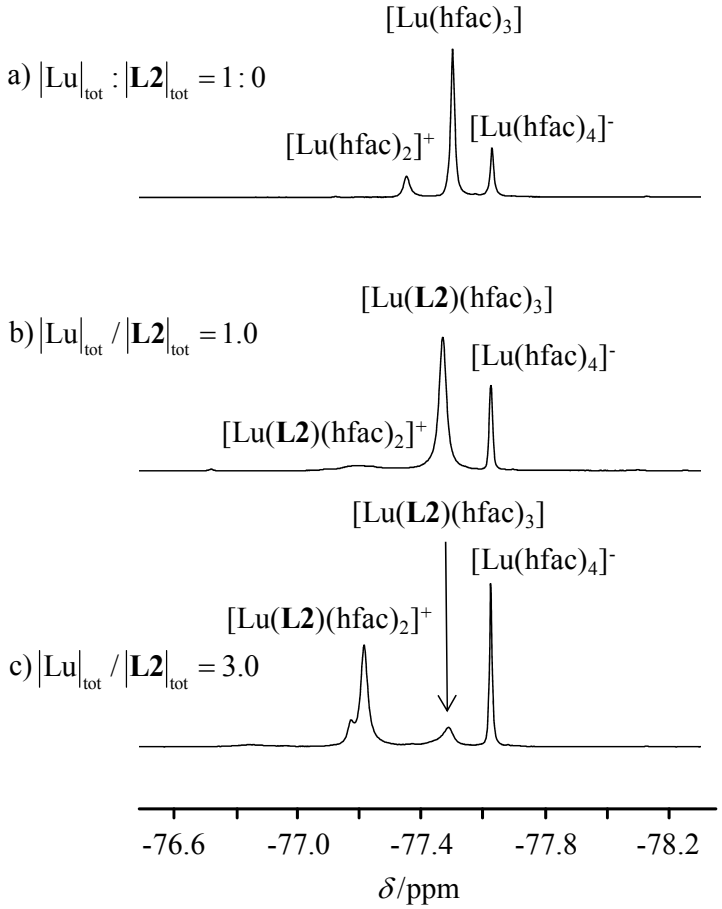

Figure S19 Selected ^{19}F NMR spectra recorded during the titration of **L2** with [Lu(hfac)$_3$(diglyme)] in CD_3CN at 293 K. a) Lu:**L2** = 1:0, b) Lu:**L2** = 1:1 and c) Lu:**L2** = 3:1.

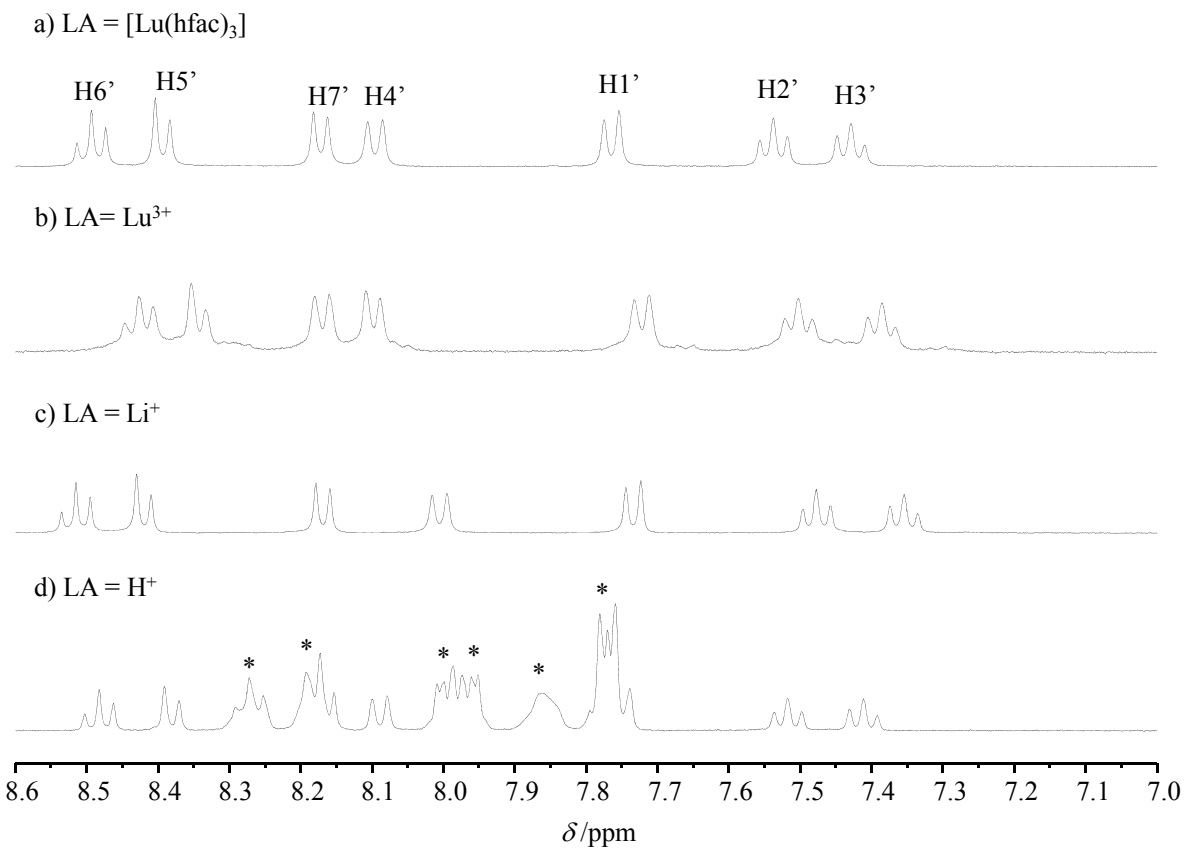

Figure S20 ^{1}H NMR spectra recorded for [Lu(**L2**)(hfac)$_2$]$^+$ in CD_3CN at 293 K prepared by reacting [Lu(**L2**)(hfac)$_3$] with various Lewis acids (LA). a) LA = [Lu(hfac)$_3$] obtained from [Lu(hfac)$_3$(diglyme)], b) LA = Lu^{3+} obtained from [Lu(CF_3SO_3)$_3$(diglyme)], c) LA = Li^+ obtained from $LiClO_4$ and d) LA = H^+ obtained form CF_3SO_3H (the signals with an asterisk are those of the protonated ligand).

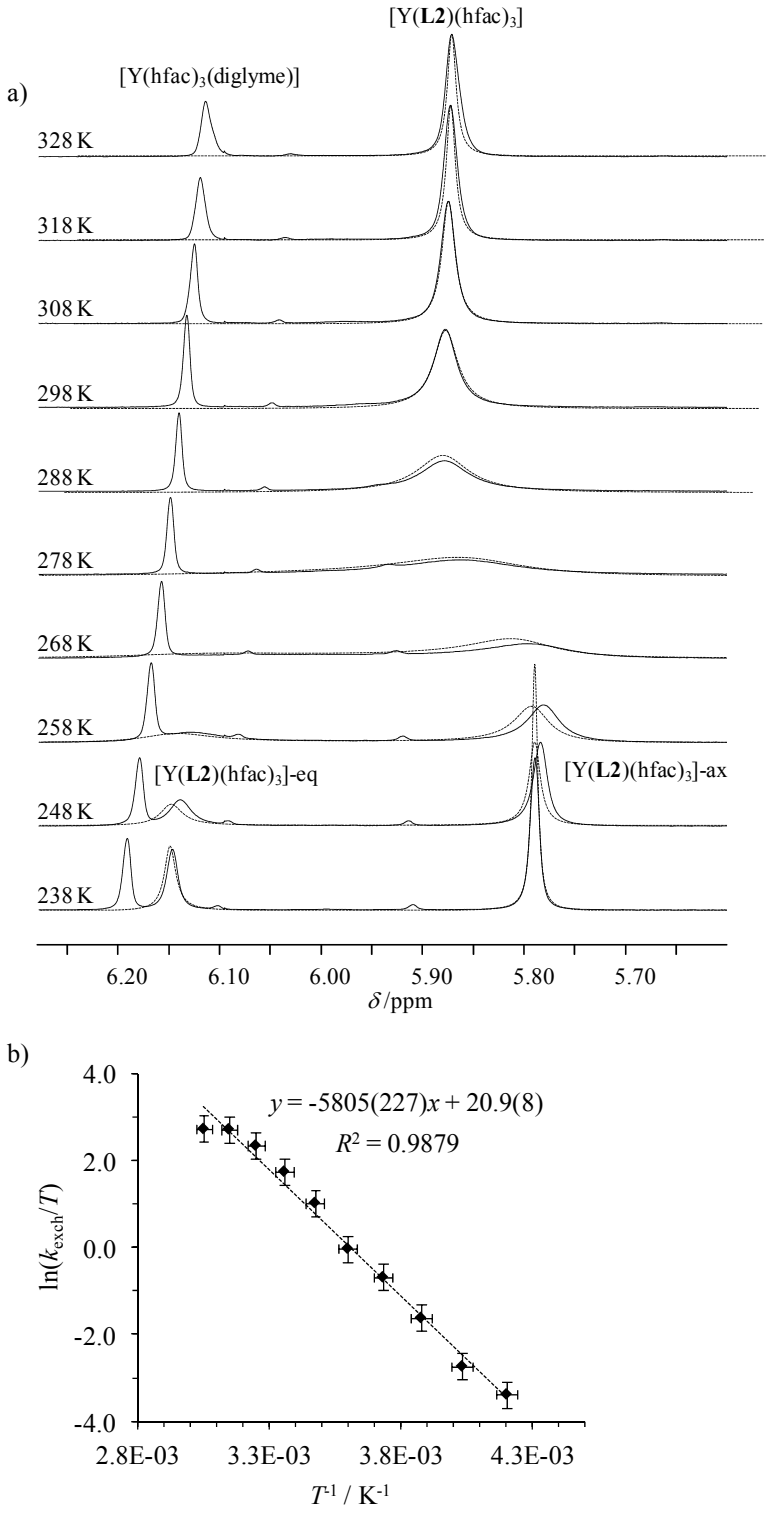

Figure S21 a) Experimental (full line) and simulated (dotted line) variable temperature ^{1}H NMR spectra recorded for [Ln(**L2**)(hfac)$_3$] in CD_3CN and showing the signals of the protons connected to the bound hfac anions (an excess of [Y(diglyme)(hfac)$_3$] was used as a reference). b) Eyring plots of the first-order kinetic rate constants calculated for the dynamic exchange between axial and equatorial hfac anion.

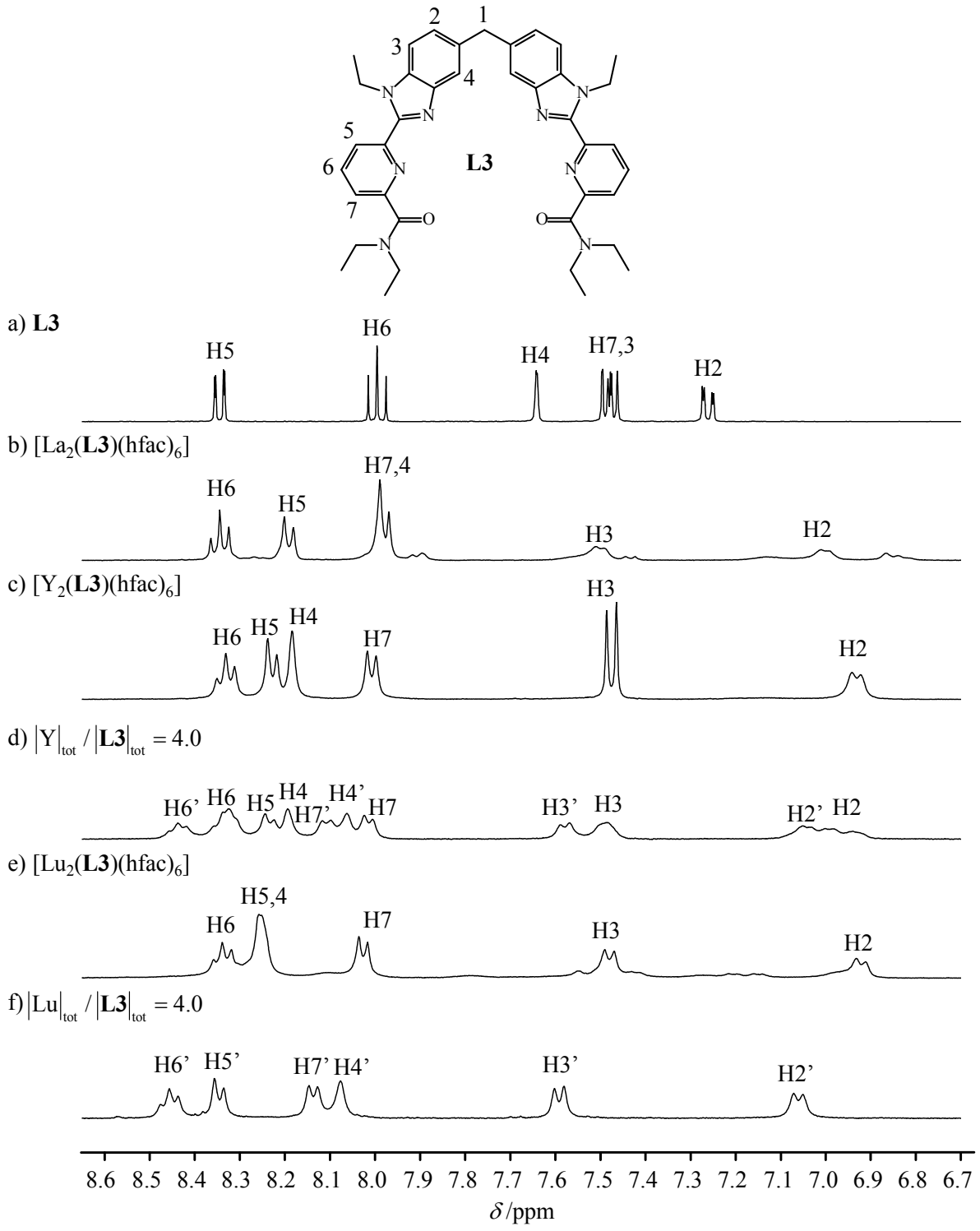

Figure S22 Aromatic parts of selected ^{1}H NMR spectra recorded during the titration of **L3** with [Ln(hfac)$_3$(diglyme)] in CD_3CN at 293 K. a) **L3**, b) La:**L3** = 2:1, c) Y:**L3** = 2:1, d) Y:**L3** = 4:1, e) Lu:**L3** = 2:1 and f) Lu:**L3** = 4:1. Protons with standard numbering correpond to those of [Ln$_2$(**L3**)(hfac)$_6$], whereas those marked are assigned to the dissociated complexes [Ln$_2$(**L3**)(hfac)$_4$]$^{2+}$ (see text).

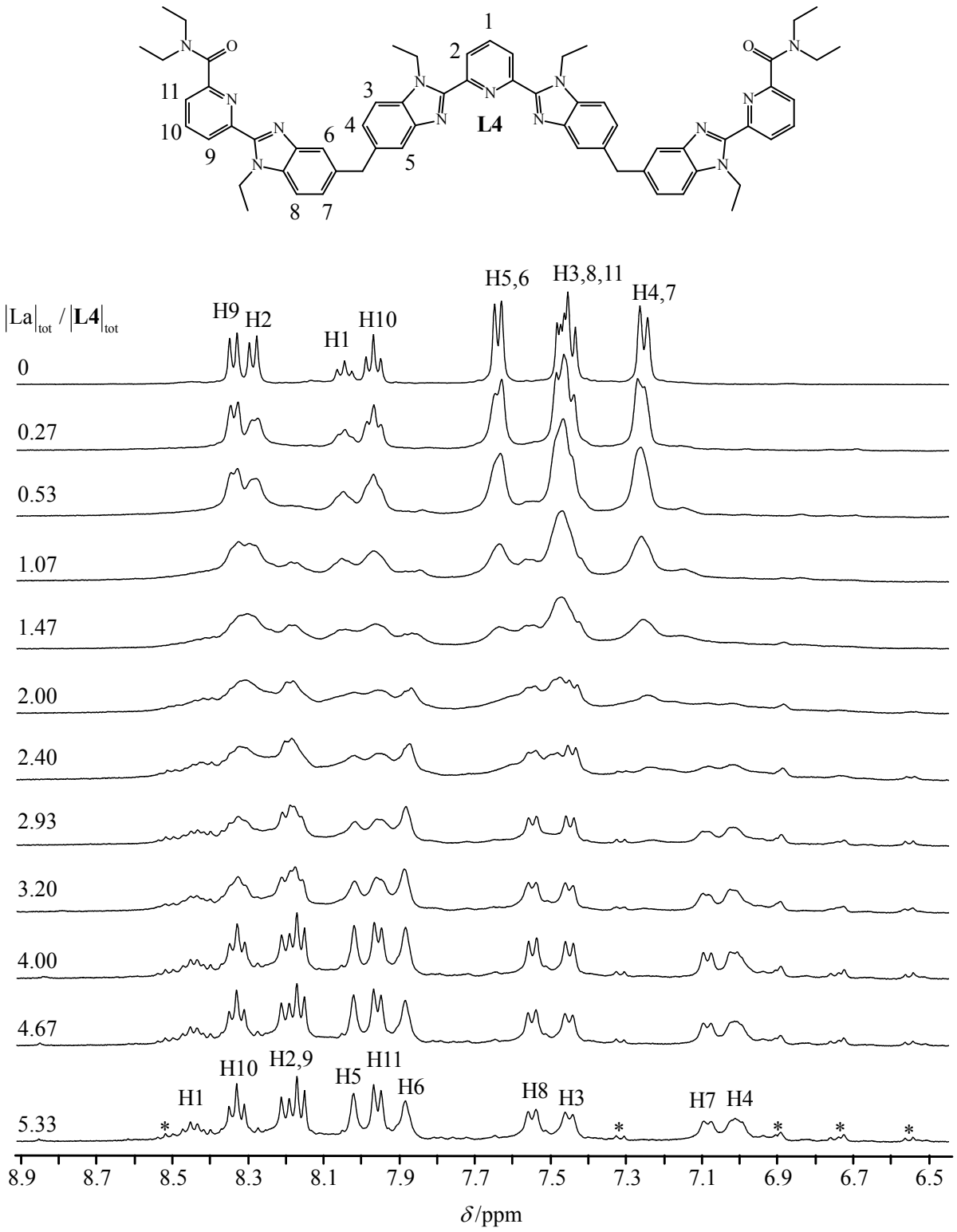

Figure S23 Aromatic parts of selected ^{1}H NMR spectra recorded during the titration of **L4** with [La(hfac)$_3$(diglyme)] in CD_3CN/CD_2Cl_2 (7:3) at 293 K. Protons with standard numbering correpond to those of [La$_3$(**L4**)(hfac)$_9$], whereas those marked with a star are assigned to traces of the double-stranded complex [La$_3$(**L4**)$_2$(hfac)$_8$]$^+$ (see text).

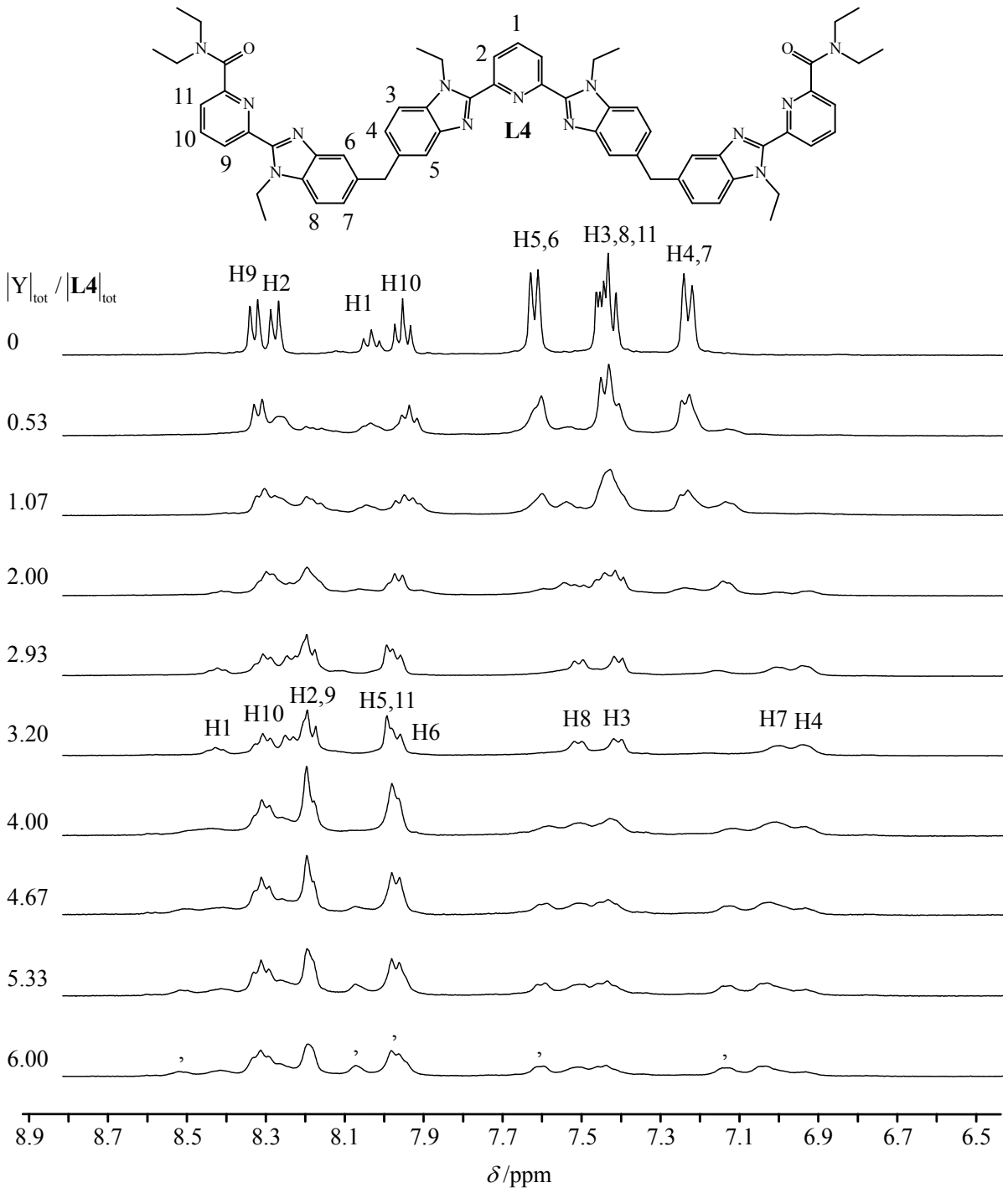

Figure S24 Aromatic parts of selected ^{1}H NMR spectra recorded during the titration of **L4** with [Y(hfac)$_3$(diglyme)] in CD_3CN/CD_2Cl_2 (7:3) at 293 K. Protons with standard numbering correpond to those of [Y_3(**L4**)(hfac)$_9$], whereas those primed are assigned to the dissociated complex [Y_3(**L4**)(hfac)$_8$]$^+$ (see text).

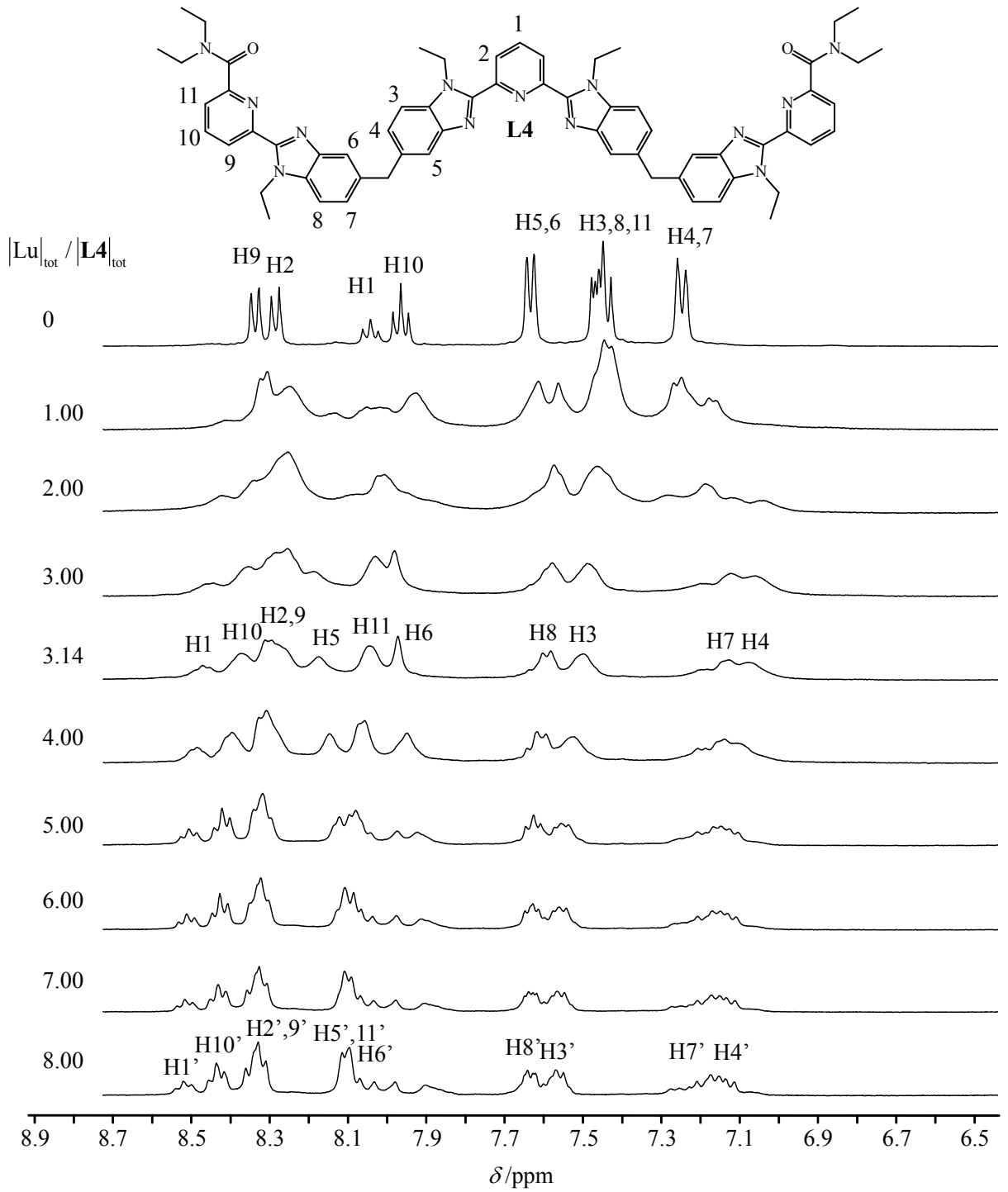

Figure S25 Aromatic parts of selected ^{1}H NMR spectra recorded during the titration of **L4** with [Lu(hfac)$_3$(diglyme)] in CD_3CN/CD_2Cl_2 (7:3) at 293 K. Protons with standard numbering correpond to those of [Lu$_3$(**L4**)(hfac)$_9$], whereas those primed are assigned to the dissociated complex [Lu$_3$(**L4**)(hfac)$_8$]$^+$ (see text).

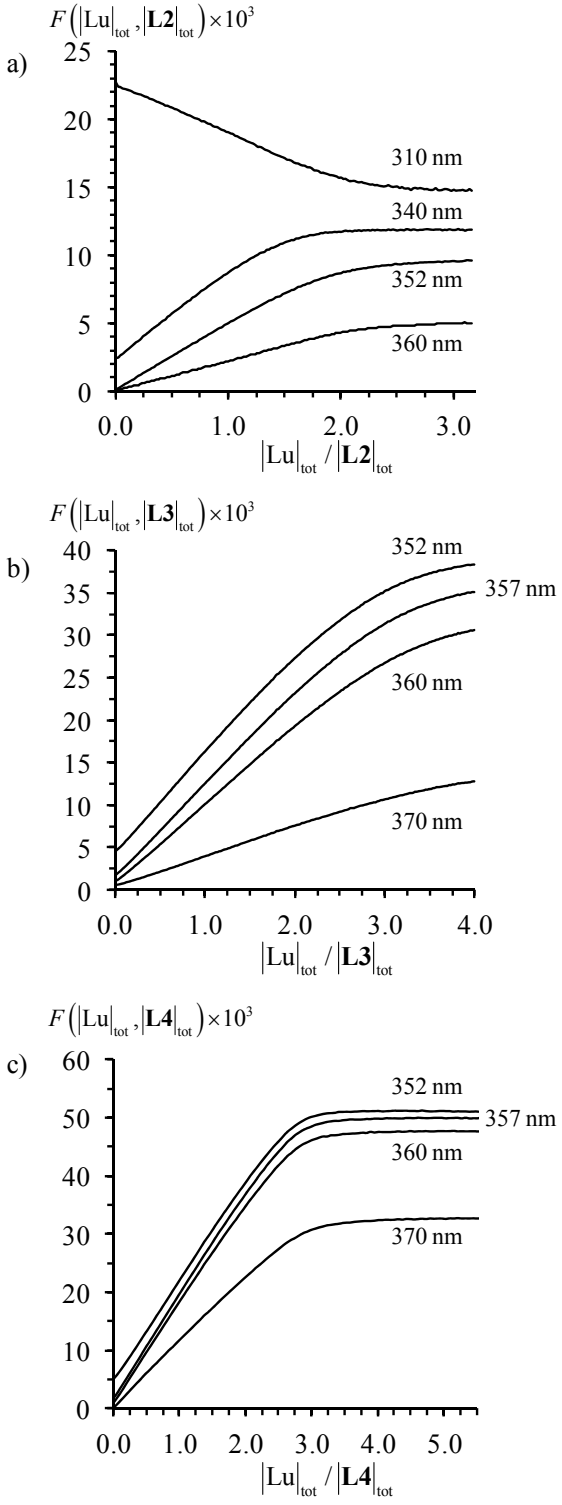

Figure S26 Variation of corrected molar extinction *F* (see appendix 3) at four different wavelengths observed during the spectrophotometric titrations of a) **L2**, b) **L3** and c) **L4** with [Lu(hfac)$_3$(diglyme)] (298 K, CH_3CN, total ligand concentration: 10^{-4} mol·dm^{-3}).

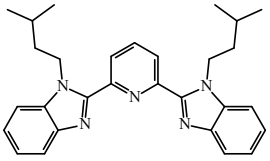

L1 + $[Ln(X)_3(CH_3CN)_3]$ $\overset{\beta_{1,1}^{Ln,\mathbf{L1}}}{\rightleftharpoons}$ $[Ln(\mathbf{L1})(X)_3]$ + 3 CH_3CN (10)

Point groups:	C_{2v}	C_{3v}	C_{2v}	C_{3v}
σ^{ext}:	2	3	2	3
σ^{int}:	$2^2 3^4$	3^3	$2^2 3^4$	1
σ^{chiral}:	1	1	1	1

$$\Rightarrow \omega_{1,1}^{chiral} = \frac{1 \cdot 1}{1 \cdot 1} = 1 \qquad \omega_{1,1}^{Ln,\mathbf{L1}} = \frac{2 \cdot 2^2 \cdot 3^4 \cdot 3 \cdot 3^3}{2 \cdot 2^2 \cdot 3^4 \cdot 3^3} = 3$$

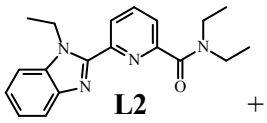

L2 + $[Ln(X)_3(CH_3CN)_3]$ $\overset{\beta_{1,1}^{Ln,\mathbf{L2}}}{\rightleftharpoons}$ $[Ln(\mathbf{L1})(X)_3]$ + 3 CH_3CN (10)

Point groups:	C_s	C_{3v}	C_s	C_{3v}
σ^{ext}:	1	3	1	3
σ^{int}:	3^3	3^3	3^3	1
σ^{chiral}:	1	1	1	1

$$\Rightarrow \omega_{1,1}^{chiral} = \frac{1 \cdot 1}{1 \cdot 1} = 1 \qquad \omega_{1,1}^{Ln,\mathbf{L2}} = \frac{1 \cdot 3^2 \cdot 3 \cdot 3^3}{1 \cdot 3^3 \cdot 3^3} = 3$$

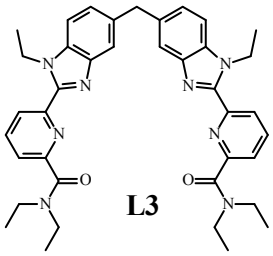

L3 + $[Ln(X)_3(CH_3CN)_3]$ $\overset{\beta_{1,1}^{Ln,\mathbf{L3}}}{\rightleftharpoons}$ $[Ln(\mathbf{L3})(X)_3]$ + 3 CH_3CN (11)

Point groups:	C_{2v}	C_{3v}	C_s	C_{3v}
σ^{ext}:	2	3	1	3
σ^{int}:	3^6	3^3	3^6	1
σ^{chiral}:	1	1	1	1

$$\Rightarrow \omega_{1,1}^{chiral} = \frac{1 \cdot 1}{1 \cdot 1} = 1 \qquad \omega_{1,1}^{Ln,\mathbf{L3}} = \frac{2 \cdot 3^6 \cdot 3 \cdot 3^3}{1 \cdot 3^6 \cdot 3^3} = 6$$

L3 + 2 $[Ln(X)_3(CH_3CN)_3]$ $\overset{\beta_{2,1}^{Ln,\mathbf{L3}}}{\rightleftharpoons}$ $[Ln_2(\mathbf{L3})(X)_6]$ + 6 CH_3CN (11)

Point groups:	C_{2v}	C_{3v}	C_{2v}	C_{3v}
σ^{ext}:	2	3	2	3
σ^{int}:	3^6	3^3	3^6	1
σ^{chiral}:	1	1	1	1

$$\Rightarrow \omega_{2,1}^{chiral} = \frac{1 \cdot 1}{1 \cdot 1} = 1 \qquad \omega_{2,1}^{Ln,\mathbf{L3}} = \frac{2 \cdot 3^6 \cdot \left(3 \cdot 3^3\right)^2}{2 \cdot 3^6 \cdot 3^6} = 9$$

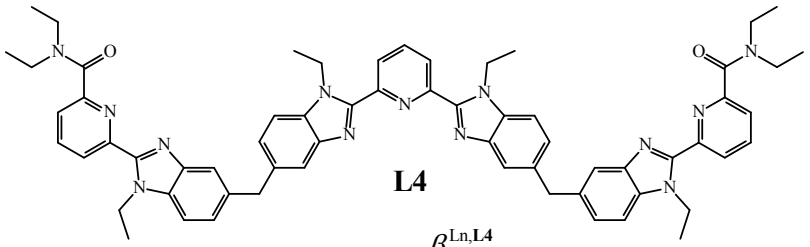

L4

$$\mathbf{L4} + [Ln(X)_3(CH_3CN)_3] \overset{\beta^{Ln,\mathbf{L4}}_{1,1,N_2O}}{\rightleftharpoons} [Ln(\mathbf{L4})(X)_3] + 3\,CH_3CN \quad (12)$$

Point groups:	C_{2v}	C_{3v}	C_s	C_{3v}
σ^{ext}:	2	3	1	3
σ^{int}:	3^4	3^3	3^4	1
σ^{chiral}:	1	1	1	1

$$\Rightarrow \omega_{1,1}^{chiral} = \frac{1\cdot 1}{1\cdot 1} = 1 \qquad \omega_{1,1,N_2O}^{Ln,\mathbf{L4}} = \frac{2\cdot 3^4\cdot 3\cdot 3^3}{1\cdot 3^4\cdot 3^3} = 6$$

$$\mathbf{L4} + [Ln(X)_3(CH_3CN)_3] \overset{\beta^{Ln,\mathbf{L4}}_{1,1,N_3}}{\rightleftharpoons} [Ln(\mathbf{L4})(X)_3] + 3\,CH_3CN \quad (12)$$

Point groups:	C_{2v}	C_{3v}	C_{2v}	C_{3v}
σ^{ext}:	2	3	2	3
σ^{int}:	3^4	3^3	3^4	1
σ^{chiral}:	1	1	1	1

$$\Rightarrow \omega_{1,1}^{chiral} = \frac{1\cdot 1}{1\cdot 1} = 1 \qquad \omega_{1,1,N_3}^{Ln,\mathbf{L4}} = \frac{2\cdot 3^4\cdot 3\cdot 3^3}{2\cdot 3^4\cdot 3^3} = 3$$

$$\mathbf{L4} + 2\,[Ln(X)_3(CH_3CN)_3] \overset{\beta^{Ln,\mathbf{L4}}_{2,1,N_2O}}{\rightleftharpoons} [Ln_2(\mathbf{L4})(X)_6] + 6\,CH_3CN \quad (12)$$

Point groups:	C_{2v}	C_{3v}	C_{2v}	C_{3v}
σ^{ext}:	2	3	2	3
σ^{int}:	3^4	3^3	3^4	1
σ^{chiral}:	1	1	1	1

$$\Rightarrow \omega_{1,1}^{chiral} = \frac{1\cdot 1}{1\cdot 1} = 1 \qquad \omega_{2,1,N_2O}^{Ln,\mathbf{L4}} = \frac{2\cdot 3^4\cdot \left(3\cdot 3^3\right)^2}{2\cdot 3^4\cdot 3^6} = 9$$

$$\mathbf{L4} + 2\,[Ln(X)_3(CH_3CN)_3] \overset{\beta^{Ln,\mathbf{L4}}_{2,1,N_3}}{\rightleftharpoons} [Ln_2(\mathbf{L4})(X)_6] + 6\,CH_3CN \quad (12)$$

Point groups:	C_{2v}	C_{3v}	C_s	C_{3v}
σ^{ext}:	2	3	1	3
σ^{int}:	3^4	3^3	3^4	1
σ^{chiral}:	1	1	1	1

$$\Rightarrow \omega_{1,1}^{chiral} = \frac{1\cdot 1}{1\cdot 1} = 1 \qquad \omega_{2,1,N_3}^{Ln,\mathbf{L4}} = \frac{2\cdot 3^4\cdot \left(3\cdot 3^3\right)^2}{1\cdot 3^4\cdot 3^6} = 18$$

$$\mathbf{L4} + 3\,[Ln(X)_3(CH_3CN)_3] \overset{\beta_{3,1}^{Ln,\mathbf{L4}}}{\rightleftharpoons} [Ln_3(\mathbf{L4})(X)_9] + 9\,CH_3CN \quad (12)$$

Point groups:	C_{2v}	C_{3v}	C_{2v}	C_{3v}
σ^{ext}:	2	3	2	3
σ^{int}:	3^4	3^3	3^4	1
σ^{chiral}:	1	1	1	1

$$\Rightarrow \omega_{1,1}^{chiral} = \frac{1 \cdot 1}{1 \cdot 1} = 1 \qquad \omega_{3,1}^{Ln,\mathbf{L4}} = \frac{2 \cdot 3^4 \cdot \left(3 \cdot 3^3\right)^3}{2 \cdot 3^4 \cdot 3^9} = 27$$

Figure S27 Symmetry numbers (σ) and statistical factors (ω) for the complexation of nine-coordinate $[Ln(X)_3(CH_3CN)_3]$ to **L1**-**L4** in acetonitrile (X = NO_3^- or $hfac^-$). For comparison purpose, we set that the weakly interacting water or diglyme molecules in the starting complexes are shifted by acetonitrile at 10^{-4} M. The somewhat arbitrary choice of an ideal C_{3v} symmetry for the starting lanthanide complexes is not crucial since each equilibrium refers to the same starting metal-containing entity.

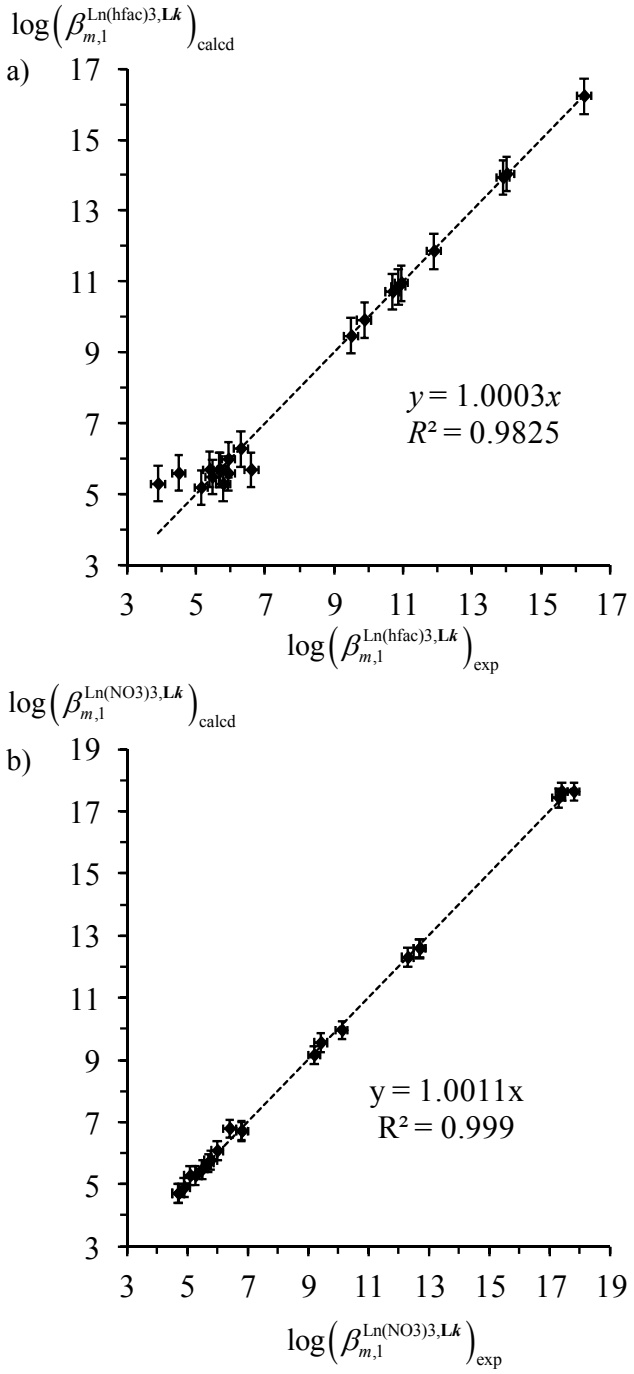

Figure S28 Cumulative experimental a) $\log\left(\beta_{m,1}^{\mathrm{Ln(hfac)3},\mathbf{L}k}\right)_{\mathrm{exp}}$ and b) $\log\left(\beta_{m,1}^{\mathrm{Ln(NO3)3},\mathbf{L}k}\right)_{\mathrm{exp}}$ (eqs 10-12) and calculated a) $\log\left(\beta_{m,1}^{\mathrm{Ln(hfac)3},\mathbf{L}k}\right)_{\mathrm{calcd}}$ and b) $\log\left(\beta_{m,1}^{\mathrm{Ln(NO3)3},\mathbf{L}k}\right)_{\mathrm{calcd}}$ (eqs 17-23) thermodynamic formation constants obtained for $[\mathrm{Ln}_m(\mathbf{L}k)(\mathrm{hfac})_{3m}]^{3m+}$ in CH_3CN at 298 K (Ln = La, Eu, Y; **L*k*** = **L1**-**L4**).

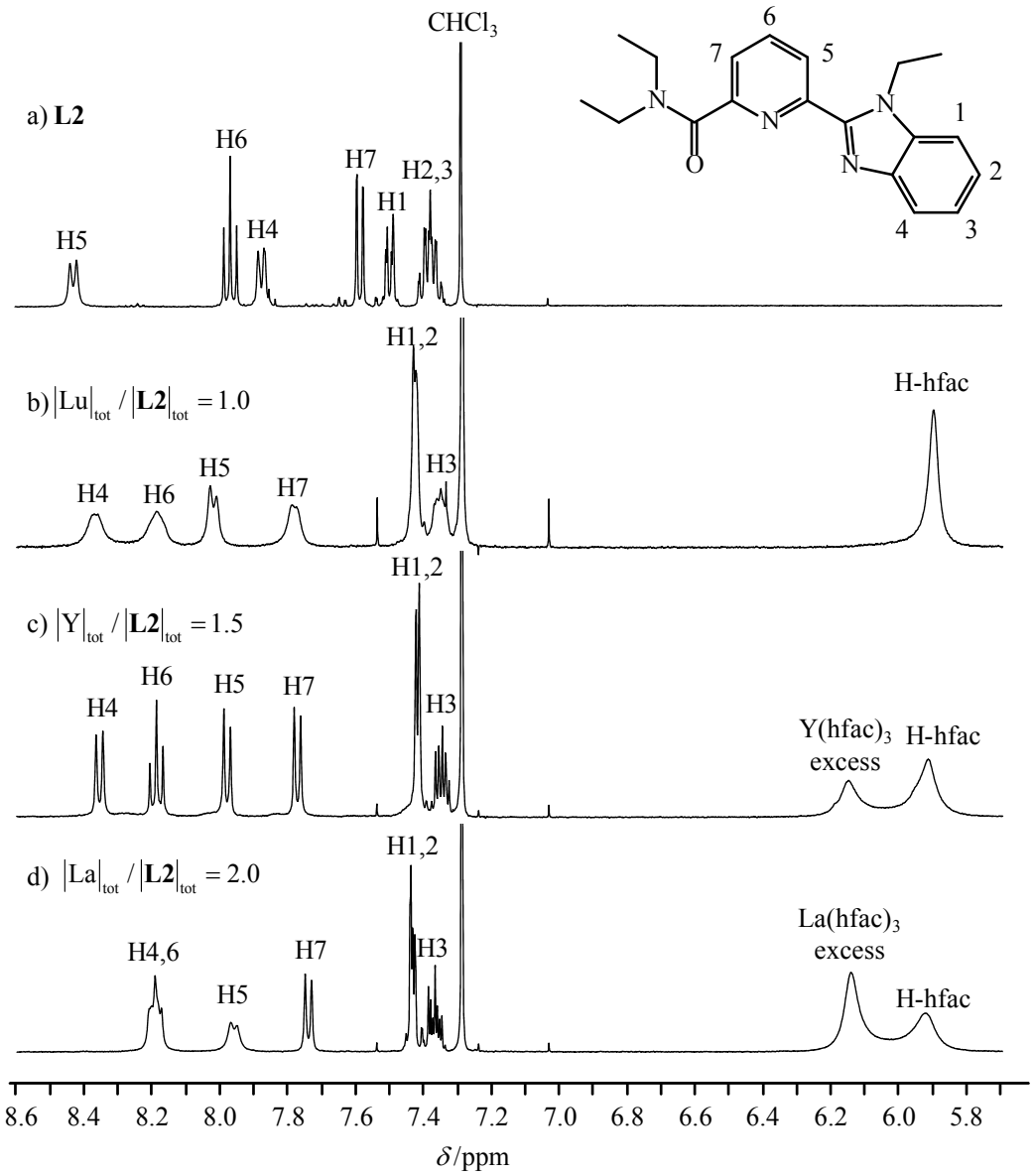

Figure S29 Selected ^{1}H NMR spectra recorded upon titration of **L2** with [Ln(hfac)$_3$(diglyme)] in $CDCl_3$ at 293 K. a) **L2**, b) Lu:**L2** = 1:1, c) Y:**L2** = 3:2 and d) La:**L2** = 2:1.

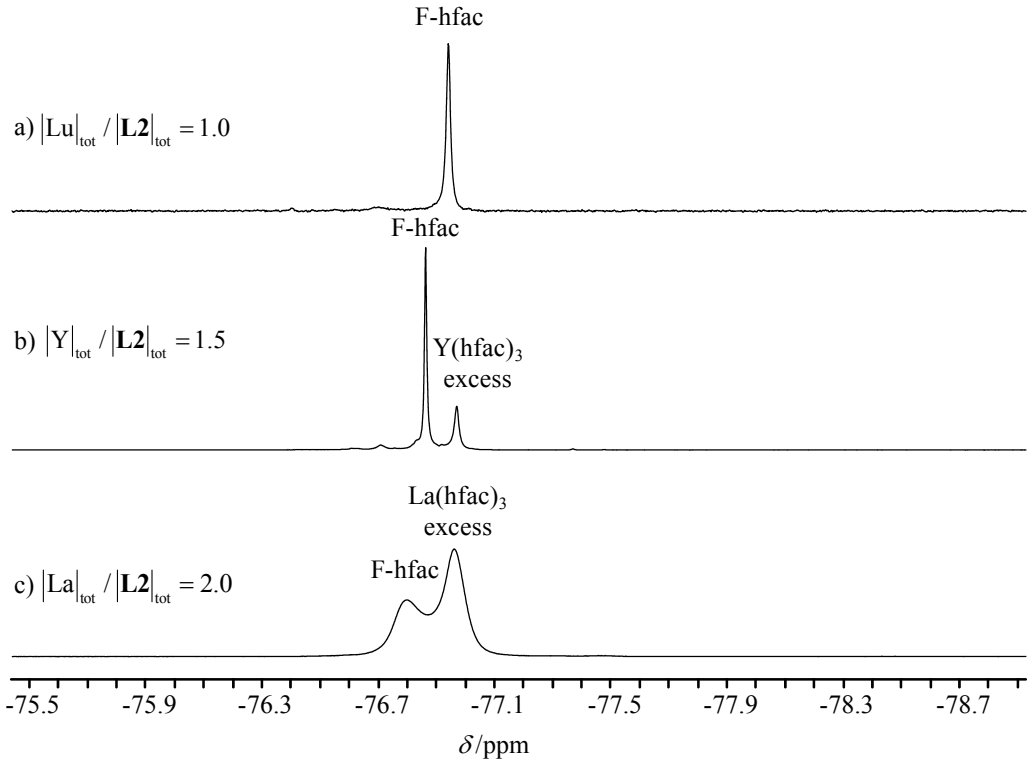

Figure S30 Selected ^{19}F NMR spectra recorded during the titration of **L2** with [Ln(hfac)$_3$(diglyme)] in $CDCl_3$ at 293 K. a) Lu:**L2** = 1:1, b) Y:**L2** = 3:2 and c) La:**L2** = 2:1.